TUDelft

Delft University of Technology

Electrode/electrolyte interfaces in (photo-)electrochemical devices

Venugopal, A.

DOI
Publication date
2023
Document Version
Final published version
Citation (APA)

Important note
To cite this publication, please use the final published version (if applicable).
Please check the document version above.

Electrode/electrolyte interfaces in (photo-)electrochemical devices

Electrode/electrolyte interfaces in (photo-)electrochemical devices

Dissertation

for the purpose of obtaining the degree of doctor
at Delft University of Technology,
by the authority of the Rector Magnificus Prof. dr. ir. T.H.J.J van der Hagen,
Chair of the Board of Doctorates,
to be defended publicaly on
Monday 20 March 2023 at 15:00 o' clock

by

Anirudh VENUGOPAL

Master of Science in Chemical Engineering
Delft University of Technology, The Netherlands,
born in Mangalore, India.

An electronic version of this dissertation is available at
`http://repository.tudelft.nl/`.

to my parents...

Contents

1

Introduction

1.1. Context

Climate change, due to the rising levels of carbon dioxide (CO_2) in our atmosphere, is viewed as an existential crisis facing humanity. If the emissions of CO_2 continue its current trend, the global temperatures are projected to increase by approximately 4 °C on average by 2100 [1], as shown in Figure 1.1. This can have devastating irreversible effects on our planet through melting ice caps and glaciers, rising sea levels, sea water acidification and changing weather patterns. In many respects, fighting against or slowing and stopping this climate change is viewed as the biggest challenge our humanity has ever faced. This is partly due to our power hungry lifestyle and the inertia within our energy systems, that is still majorly dependent on fossil based resources. The use of fossil based energy resources, which emits CO_2 into the atmosphere, is the primary reason for this ongoing global warming. The Intergovernmental Panel on Climate Change (IPCC) in its 2021 report had presented different scenarios for global warming, which outlined the need to limit the global temperature increase to 1.5 °C to avoid catastrophic effects on our planet. The IPCC has recently also warned countries that the global average temperature will rise above this 1.5 °C limit in almost two decades under the current circumstances and that even adhering to the Paris Climate Agreement will not be enough to limit the temperature rise below the 1.5 °C limit. [2] They have urged countries to do more to avoid a climate disaster. Drastic innovations in carbon neutral technologies, change in policies and our lifestyle are needed to combat this climate change and have any hope of limiting the global average temperature rise at 1.5 °C above the preindustrial levels.

The need for sustainable, renewable energy sources to transition away from fossil based energy sources is more than obvious at this point. Electrification of our energy infrastructure using green electricity from wind and solar is viewed as the first decarbonisation vector in this transition. [3] However, the incorporation of such intermittent energy sources into our energy infrastructure poses its own challenges. The disparity between the energy supply and demand cycles when using such intermittent energy sources entails that new energy storage solutions are needed to bridge this disparity. At the TW scale, chemical energy storage (i.e. storage of energy in the chemical bonds of molecules) is one of the most cost effective options to store this energy and hence is one of the most important energy storage solutions. [4, 5] Additionally, during this energy

1
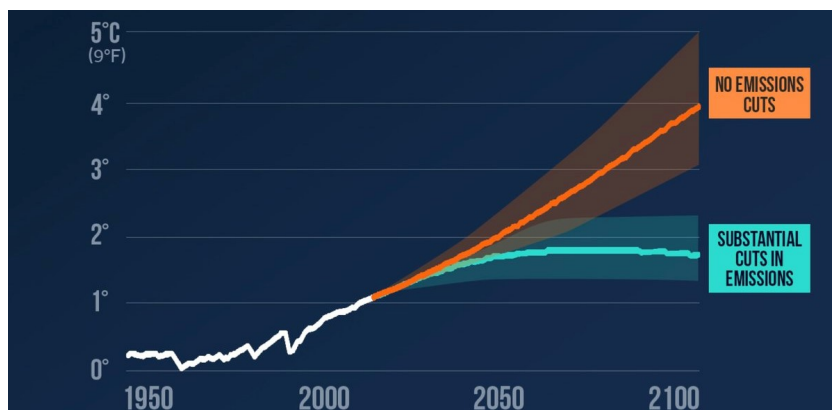
Figure 1.1: Projections for global average temperature increase till 2100 under scenarios with substantial cuts in emissions and with no cuts in emissions [2]

transition, our economy will primarily transition from a thermal energy based economy to an electrical energy based economy. This transition brings in new opportunities and challenges. The biggest challenge here is to reinvent our chemical industry which is still primarily dependent on thermal processes. Here, electrochemistry can offer to be a solution for both these problems. Using electrochemistry, the electrical energy can be converted into chemical energy or vice versa. This way, electrochemistry can be used for chemical energy storage and also to produce green chemicals for future chemical industries.

1.2. Electrochemistry

Electrochemistry is a discipline that studies the relationship between electricity and chemistry. With a thorough understanding of this concept, we can use chemical changes to produce electricity, like in a battery, or alternatively use electricity to drive chemical processes. We will focus on the latter concept here. With this approach, we can use sustainably produced electricity to produce the basic building blocks for the chemical industry of the future. These e-refineries are essential to get to a zero carbon future.

Using electrochemistry to produce basic chemicals is an age old concept, which is actively being used within the chlor-alkali industry for decades to produce chlorine gas. Acid and alkaline water electrolysis to produce hydrogen has also been explored in the past. However, the latter technology was not actively pursued since it was cheaper to make hydrogen via fossil based thermochemical processes. In the context of this energy transition, there has been a renewed interest in electrochemistry and the technology itself has made significant advancements in the past few years. Green hydrogen, hydrogen produced via water electrolysis using green electricity, is viewed as one of the key components to facilitate this energy transition, owing to the versatility of the hydrogen molecules. This green hydrogen can be processed further for storage or used as is and
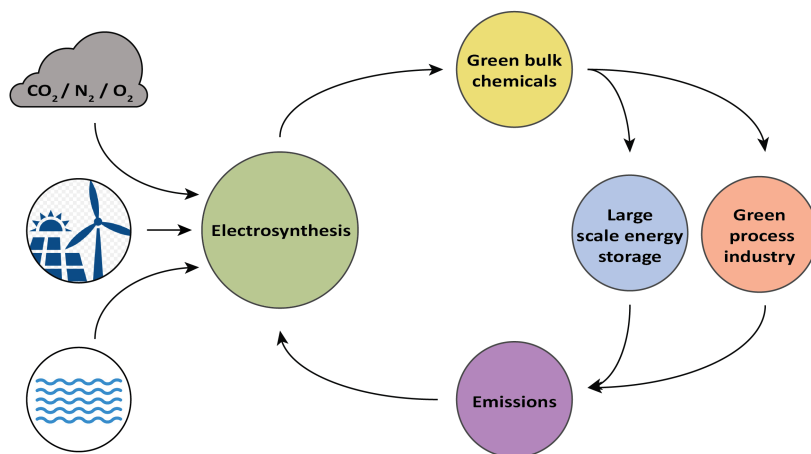
Figure 1.2: Renewable electricity driven energy and chemical infrastructure via electrosynthesis can replace the present thermochemical energy and chemical infrastrucutre to a large extent in the future

can be converted back to electricity using fuel cells, as and when required. This green hydrogen can also be used directly for end use applications, particularly in the hard-to-electrify sectors, like in the case of steel making and chemical processing industries. And as such, green hydrogen is viewed as the second decarbonisation vector in the energy transition. [3] The projected share of electrification and green hydrogen vectors in the energy transition is shown in Figure 1.2. To enable this transition in a cost effective manner, further advancements in the technology are required to bring down the levelized cost of green hydrogen and make the technology self-sustainable and cost-competitive against fossil based hydrogen.

Similarly, electrochemistry can also be used to produce other chemicals such as small chain hydrocarbons, hydrogen peroxide, ammonia etc. [6–8], which are some of the basic building blocks for our chemical industry. However, these technologies also face the similar constraints as the green hydrogen industry and needs to overcome these challenges to make the technologies cost-competitive. To hasten this energy transition, new innovative approaches are required to facilitate this reduction in capital and operational costs of electrolysis. Below we briefly discuss two such approaches that have the potential to do so.

1.2.1. Photoelectrochemistry

One such technologically attractive pathway is photoelectrochemistry, which is an integrated device that harvests solar energy and directly uses the electrons to split water into hydrogen and oxygen. [9] This is achieved by replacing one of the traditional electrodes in an electrolyzer with a semiconducting electrode. This semiconductor can harvest solar energy and generate energetic electron/hole pairs that can drive a chemical reaction at the electrode surface. A typical photoelectrochemical cell would look like the

1
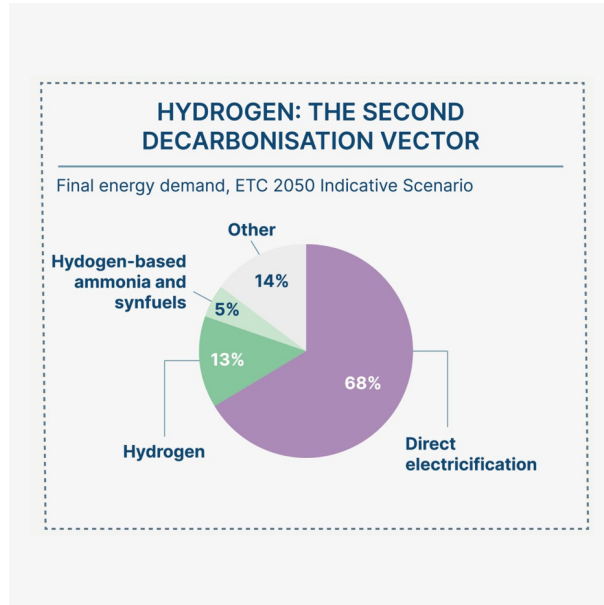
Figure 1.3: Projected share of green hydrogen in the decarbonization strategy [3]

schematic in Figure 1.3. There are several advantages for such a device over traditional photovoltaics + electrolyzers. These devices can make use of the large surface area of the solar cell (that is needed to capture the incoming photons) and hence they can work at much smaller current densities in comparison to electrolyzers, which require lower overpotentials. Additionally, such devices do not require a power converter, which is an expensive component in the electrolyzer balance of plant. The overall efficiencies of such devices can also be higher, since the electrical energy can be directly used in such integrated devices, without any conversion losses. These devices can also be made into a monolithic system, which can lead to a lower capital cost. [9, 10] These advantages have made photoelectrochemical devices a hot research topic over the past decades.

To meet these technical needs, the main active material in these systems, the light absorbing photoelectrode, must fulfil certain physical, chemical and electronic criteria. The most common material for this is a semiconductor, which can absorb light and transfer photogenerated charges to surfaces to perform catalysis. The band edges of the semiconductor should straddle the reaction energies, for it to be effective in such devices. The semiconductor should have a small enough bandgap to effectively capture large part of the solar spectrum and the bandgap should be large enough to generate enough voltage to drive the reactions of interest. [9, 10] The semiconductor bulk should perform effective electron-hole separation and should have low bulk and surface recombination of charges. Additionally, the semiconductor surface should actively catalyse the reactions of interest. There are several candidates, like TiO_2, Fe_2O_3, $BiVO_4$, $CuWO_4$, WO_3, $SnWO_4$, SiC etc. that satisfies most the requirements discussed above. [12, 13] The
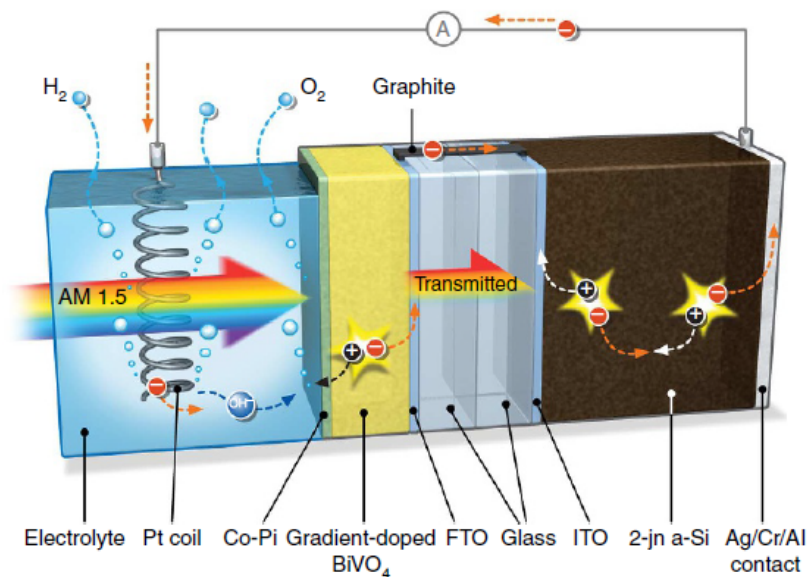
Figure 1.4: Integrated photoelectrochemical cell harvesting sunlight and driving the water splitting reaction [11]

challenge within the research community has been to identify the ideal photoelectrode that satisfies all the above requirement. This ideal material is yet to be discovered. One way to circumvent this issue is to operate tandem devices, which uses two or more photoelectrode materials to collectively satisfy the above requirements and achieve the same task. Such configurations have shown to work, albeit at a lower efficiency than what was initially envisioned.[11] The focus here is now on optimizing such devices to improve their efficiencies and decrease the cost.

While the search for the ideal photoelectrode and optimal system configurations are ongoing, the biggest challenge of these devices is the long term stability of the photoelectrode material. While there is a good understanding of the bulk stability of the photoelectrode under these harsh conditions, the knowledge of stability of the photoelectrode/electrolyte interface is lacking. In this thesis, we investigate some aspects of the stability of the photoelectrode/electrolyte interfaces and discuss the implications of these findings on the practical use of such devices.

1.2.2. Tuning surface electronic properties of (photo-)electrocatalysts

The electrocatalyst surface is another key element of an electrochemical device, as the surface is where the redox reactions takes place. An ideal electrocatalyst should have the right surface electronic properties to absorb the reactants, optimally bind the reaction intermediates, to actively and selectively catalyse the reaction of interest and desorb the targeted products. [14] This activity and selectivity has a direct impact on the operational

efficiency and the operational costs of the system. In addition, often times the ideal catalytic material for the reaction of interest requires the use of rare and expensive metals which can drive up the capital costs of the system. Therefore, to reduce the capital and operational costs of the system, researchers have to often find innovative ways to tune the surface electronic properties of the electrocatalysts while making use of cheaper and more abundant materials.

The common approach to tuning the surface electronic properties of the catalysts is to mix or alloy two or more elements to form a new material with the required properties. [15, 16] While this approach is useful in many cases, they do have certain drawbacks. The mixing or alloying also effects the bulk properties of the material, which is not desirable in some cases. In addition, the mixed or alloyed material can phase separate under certain reaction conditions making this approach ineffective for these scenarios. [17, 18] Therefore, there is a need for alternative approaches that can selectively tune the surface electronic property of the catalyst in a stable manner while making use of cheap and abundant materials. In this thesis, we briefly investigate the use of polymers to tune the surface electronic properties of electrocatalysts to make them active and selective for the reaction of interest.

1.3. Thesis outline

As discussed above, through a series of works, this thesis contributes to the existing knowledge of electrode/electrolyte interfaces. The primary focus of this thesis is on the anode half of the electrochemical cell. However, the findings of this thesis could be easily extended to the cathode half of the electrochemical cell and hence is universal. The first part of this thesis discusses a concept called "photocharging effect of metal oxide photoanodes", which was first presented by the author's research group as a PEC performance improvement strategy. Through a series of works, the author and his colleagues later show that this PEC performance improvement was infact a temporary by-product of the degradation of photoelectrode over time. This thesis also dedicates a chapter to discuss the effect of polymer loading on the surface electronic properties of electrocatalysts.

The author uses the Chapter 2 to summarize his works studying the photoelectrode/ electrolyte interfaces and put forward his broad conclusions and suggestions to the field. In this chapter, he points out that photoelectrodes have additional degradation pathways in comparison to traditional metallic electrodes. He shows that this factor makes it difficult to find a practical photoelectrode material that offers good photoelectrochemical performance and long term stability. He proposes that the photoelectrochemical devices might be better suited for less demanding reaction environments and systems in comparison to water splitting systems.

Chapter 3 was formulated with the need to study the photoelectrochemical/ electrolyte interfaces under operating conditions. Therefore, in this chapter, the authors reveal the new findings they obtained regarding the $BiVO_4$ photoanode/electrolyte inter-

face. In this chapter, they also discuss the novel operando infrared spectroscopy setup they developed to perform these studies. The setup was used to demonstrate the dynamically changing $BiVO_4$/ electrolyte interface, which was then to explain the photocharging effect of $BiVO_4$ photoanodes.

Chapter 4 discusses the photocharging effect of $BiVO_4$ photoanodes from a different perspective. It was motivated by the need to better understand the changes observed on the photocharged $BiVO_4$ sample. The chapter reveals the observations and finding from a series of bulk and surface analysis performed on pristine and photocharged $BiVO_4$ samples. The chapter introduces a new technique of grazing incidence X-ray Raman scattering to study the space charge region of photoelectrodes. The authors use these observations and findings to propose the formation of a heterojunction at the surface of photocharged $BiVO_4$ photoanodes and use this concept to explain the performance improvement they observe.

Chapter 5 discusses the exploratory work that was performed to see if the photocharging effect was specific to $BiVO_4$ photoanodes, or was it also seen in other photoanode materials. In this chapter, the authors show that this effect was also seen in $CuWO_4$ photoanodes, which gave the first indication that the mechanism behind the photocharging effect might be more universal.

Chapter 6 discusses the effect of polymer loading on the surface electronic properties of electrocatalysts. The authors used a recent example of polytetrafluoroethylene loaded water oxidation catalysts to demonstrate alteration of surface electronic properties of electrocatalysts with polymer loading. This work becomes extremely important in the context of increased usage of polymers as ionomers or as membranes within electrolyzer systems, which results in similar polymer/electrocatalyst interfaces.

1

1.4. References

(1) V. Masson-Delmotte et al. *IPCC, 2018: Global warming of 1.5° C. An IPCC special report on the impacts of global warming of 1.5° C above pre-industrial levels and related global greenhouse gas emission pathways, in the context of strengthening the global response to the threat of cli*; tech. rep.; 2018.

(2) Hausfather Zeke ; Tebaldi, C. IPCC 6th Assessment Report - The Physical Science Basis, 2021.

(3) Others, E. T. C. a. *Making the Hydrogen Economy Possible: Accelerating clean hydrogen in an electrified economy*; tech. rep.; Hydrogen Knowledge Centre, 2021.

(4) Schlögl, R. *Green Chemistry* **2021**, *23*, 1584–1593.

(5) Bettoli, A. e. a. *McKinsey Sustainability* **2021**.

(6) Kibria, M. G.; Edwards, J. P.; Gabardo, C. M.; Dinh, C. T.; Seifitokaldani, A.; Sinton, D.; Sargent, E. H. *Advanced Materials* **2019**, *31*, DOI: 10.1002/adma.201807166.

(7) Shi, X.; Back, S.; Gill, T. M.; Siahrostami, S.; Zheng, X. *Chem* **2021**, *7*, 38–63.

(8) Foster, S. L.; Bakovic, S. I.; Duda, R. D.; Maheshwari, S.; Milton, R. D.; Minteer, S. D.; Janik, M. J.; Renner, J. N.; Greenlee, L. F. *Nature Catalysis* **2018**, *1*, 490–500.

(9) Roel van de Krol, M. G., *Photoelectrochemical Hydrogen Production*.

(10) Sixto Giménez, B. J., *Photoelectrochemical solar fuel production*; Springer: Switzerland, 2016.

(11) Abdi, F. F.; Han, L.; Smets, A. H. M.; Zeman, M.; Dam, B.; van de Krol, R. *Nature Communications* **2013**, *4*, 2195.

(12) Kang, D.; Kim, T. W.; Kubota, S. R.; Cardiel, A. C.; Cha, H. G.; Choi, K. S. *Chemical Reviews* **2015**, *115*, 12839–12887.

(13) Chen, Z.; Dinh, H. N.; Miller, E., *Photoelectrochemical water splitting: standards, experimental methods, and protocols*, 2013, p 126.

(14) Ooka, H.; Huang, J.; Exner, K. S. *Frontiers in Energy Research* **2021**, *9*, 1–20.

(15) Escudero-Escribano María, e. a. *Science* **2016**, *352*, 73–76.

(16) Stamenkovic, V.; Mun, B. S.; Mayrhofer, K. J. J.; Ross, P. N.; Markovic, N. M.; Rossmeisl, J.; Greeley, J.; Nørskov, J. K. *Angewandte Chemie* **2006**, *118*, 2963–2967.

(17) Xu, C.; Wang, R.; Chen, M.; Zhang, Y.; Ding, Y. *Physical Chemistry Chemical Physics* **2010**, *12*, 239–246.

(18) Jeon, T. Y.; Yoo, S. J.; Cho, Y. H.; Kang, S. H.; Sung, Y. E. *Electrochemistry Communications* **2010**, *12*, 1796–1799.

2

Advancing the understanding of the semiconductor/electrolyte interface in metal oxide photoelectrodes

For the practical viability of photoelectrochemical devices, the technology should offer longer term operability and stability among other aspects. A pre-requisite to ensuring long term operability is a thorough understanding of the different degradation mechanisms within a photoelectrode. Unfortunately, this information has been lacking due to the complexity of studying these systems and its interfaces. Through a series of works under the title of "photocharging of metal oxide photoanodes" from our research group, extensive effort was made to study this complex metal oxide/ electrolyte interface under ex situ, in situ and operando conditions and reveal new insights. This chapter is the culmination of these research efforts and summarizes the key aspects and lessons learned from these works. In this chapter, we shine light into some of the degradation mechanisms within a photoelectrode and explain how they are different from a metallic electrode. The authors introduce the concept of "surface recombination triggered material degradation" within these photoelectrodes and discusses its implications on the future of photoelectrochemistry.

2.1. Introduction

Clean and sustainable technological solutions are required to tackle the climate emergency[1] and the issues associated with it. An urgent need here is to have technologies that can harvest and store energy from the abundant clean and renewable energy sources like wind and solar. In this context, photoelectrochemistry is a technologically attractive pathway to harvest solar energy and directly produce green chemicals in a decentralized manner. [2, 3] Here, metal oxides semiconductors are an important class of materials that are used as photoelectrodes in such systems. They can potentially offer good stability and have tunable electronic band structures that can align with the redox potentials of desired products. [2] For the technology to be economically viable, it needs to offer good device efficiencies and long term durability at low-costs. While it has been demonstrated in many instances that the efficiencies of these devices can be improved through different innovative device architectures [4, 5], the long term stabilities of these photoelectrode materials is still far below the range where the technology can be viably scaled up. To develop stable photoelectrochemical (PEC) systems and guarantee long term stability, there needs to be a very good understanding about the different degradation mechanisms within a photoelectrode. While significant effort has been put into understanding bulk degradation mechanisms, detailed information regarding the different interfacial degradation mechanisms have been lacking, primarily due to the practical difficulty of studying these interfaces under operando conditions. In addition, a thorough understanding of the semiconductor/electrolyte interface is also important to further optimize the performance of these devices and achieve higher device efficiencies.

While investigating a self-performance improvement mechanism of metal oxide photoelectrodes, which was discovered by our research group in 2016 and dubbed as the "photocharging effect of metal oxide photoelectrodes" [6], we gathered new information that can advance our understanding of the metal oxide/electrolyte interfaces and its degradation mechanisms. This article is a summary of our research efforts on this topic and an account of our conclusions and new insights from this multi-year research effort.

2.2. Differences between metallic and semiconductor electrodes

The main difference between a metallic electrode and a photoelectrode in an electrochemical cell is the presence of energetic holes and electrons within the same electrode under operating conditions. Electron – hole pairs are created within a semiconductor photoelectrode upon the absorption of photons, while metallic electrodes have free electrons that can be conducted through the application of an applied potential. The space charge region in the photoelectrode separates photoexcited electrons from the holes using a built in electric field, directing the electrons to the bulk and holes to the surface in the case of a photoanode and vice versa for a photocathode. [2] Since both energetic electrons and holes are present within the same electrode, both oxidizing and reducing

environments co-exist within the same electrode. Whereas, in the case of metallic electrodes, electrons are transferred between the electrode and redox species by controlling the potential at the electrode. [7] This applied potential driven process implies that each electrode will only either have an oxidation or reduction environment at a given time within the same electrode. This is represented schematically in Figure 2.1. This difference in redox environments and charge transfer mechanisms implies that the degradation mechanisms of the respective electrodes can also be different. This difference is key to understanding the interfacial degradation mechanisms of a photoelectrode, which is explained later in this article.
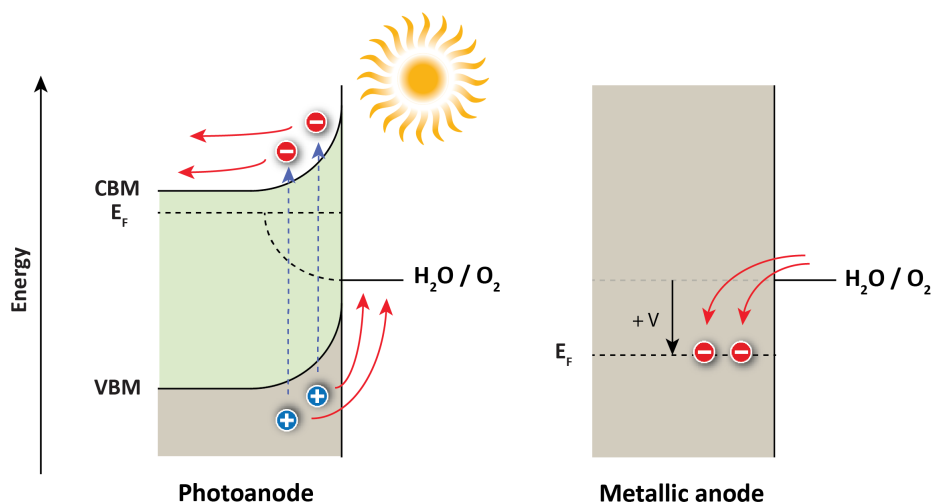
Figure 2.1: Schematic depicting the differences in a semiconductor photoanode and a metallic photoanode. The semiconductor photoelectrode has the presence of both oxidative and reductive environments within the same electrode simultaneously, while the metallic electrode will only contain either oxidative or reductive environment at a time and is determined by the potential applied.

2.3. Photocharging of metal oxide photoanodes

It was observed by Trześniewski et al. [6] that when $BiVO_4$ photoanodes were subjected prolonged illumination under open circuit conditions, their PEC performance improved drastically. This improvement can be seen in the cyclic voltammetries in Figure 2.2 (a), where the photocharged samples demonstrated a cathodic shift in the onset potential and a multi-fold increase in the photocurrent across a wide range of applied potentials. In addition, a cathodic shift in the open circuit potential was also observed during this procedure, as shown in the inset in Figure 2.2 (a). It was seen that this effect was reversible under dark conditions and could be regenerated by subjecting the photoelectrode again to prolonged light exposure. This effect was subsequently termed the photocharging effect. It was observed that the pH of the electrolyte had a drastic effect on the

photocharging enhancement, with alkaline conditions showing the most enhancement while acidic conditions showed negligible enhancement. [8] The same effect was also observed by Liu et al. [9] on their BiVO$_4$ photoanodes, as shown in Figure 2.2 (c). Hole scavenger studies using hydrogen peroxide on photocharged and untreated samples, as shown in Figure 2.2 (b, c) , demonstrated that the enhancement was due to changes both at the surface and bulk of the BiVO$_4$ photoelectrodes. [6, 9] Liu et al. performed electrochemical impedance spectroscopy (EIS) on the untreated and photocharged BiVO$_4$ samples and observed an increase in the charge carrier concentration in the BiVO$_4$ post photocharging. [9] This can be observed in the Mott-Schottky plot in Figure 2.2 (d), where the carrier concentration is inversely proportional to the slope of linear fit.
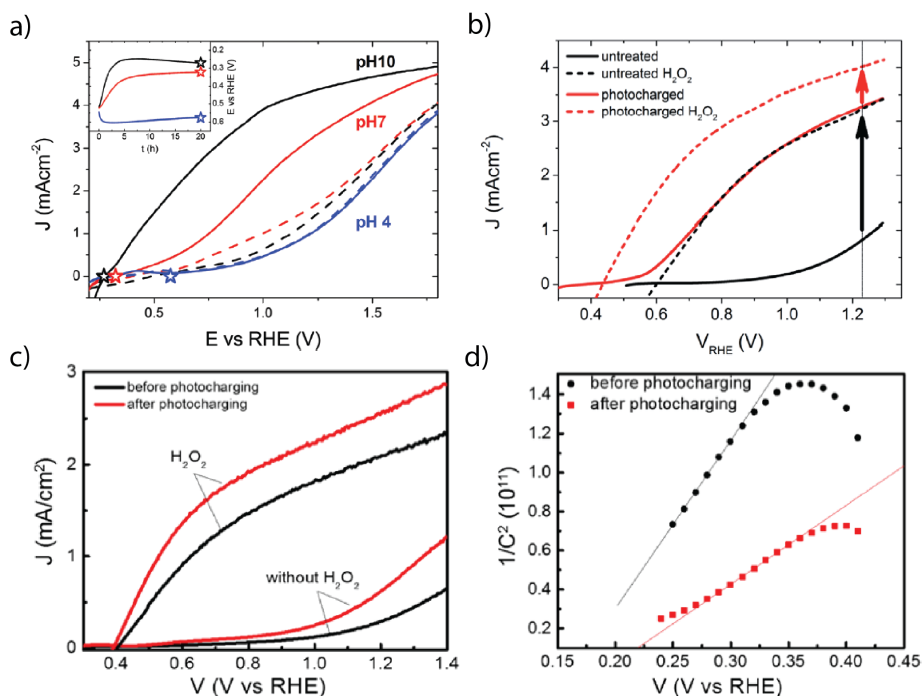
Figure 2.2: (a) Current density vs applied voltage plots of untreated an photocharged samples in PBA (phosphate-borate-acetate) buffer at pH 4,7 and 10. Dashed lines represent untreated samples, while solid lines represent photocharged samples. Inset: Open-circuit voltage vs time trends collected during photocharging at different pH conditions. (b) Current density vs applied voltage plots of untreated and photocharged BiVO$_4$, with H$_2$O$_2$ as hole scavenger, in 0.1 M KPi buffer (pH 7). (c) Similar current density vs applied voltage plot of untreated and photocharged BiVO$_4$, with and without a hole scavenger, obtained by Liu et al. (d) Mott-Schottky plots of untreated and photocharged BiVO$_4$ obtained by Liu et al. The plots (a-b) and (c-d) were adapted with permission from ref [6], [8] and [9], respectively.

Trześniewski et al. performed external quantum efficiency (EQE), or incident photon to current efficiency (IPCE), and internal quantum efficiency (IQE), or absorbed photon to current efficiency (APCE), studies on photocharged BiVO$_4$ samples, as shown in
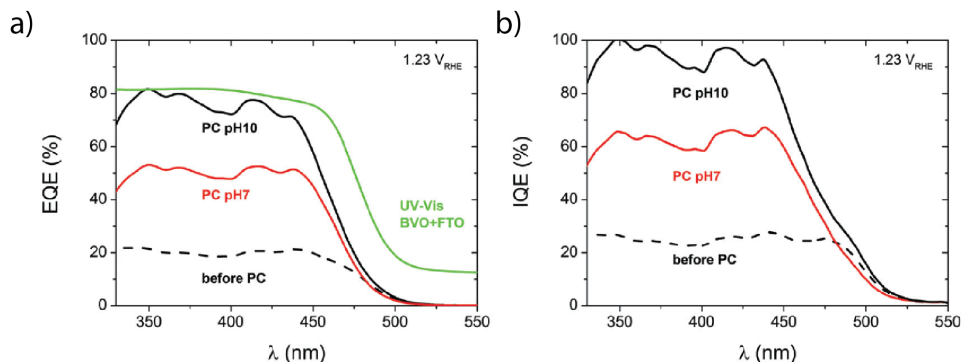
Figure 2.3: (a) External quantum efficiency plot of untreated and photocharged $BiVO_4$ at pH 7 and pH 10 conditions. The plots was adapted with permission from ref [8].

Figure 2.3. [8] While the $BiVO_4$ sample before photocharging showed 20% EQE, the photocharged samples showed 50 and 75% EQE on average (below 450 nm) at pH 7 and pH 10 conditions respectively. When corrected for the photon absorption of the $BiVO_4$ film, this resulted in a near 100% quantum efficiency at pH 10 conditions, as shown in Figure 2.3 (b). The internal quantum efficiency plots are an indication of the efficiency of charge separation and utilization within a photoelectrode. Hence, these results suggest that the photoelectrode is able to achieve near unity charge separation upon photocharging treatment under mildly alkaline conditions.

To understand if this effect was unique to $BiVO_4$ photoanodes, other metal oxide photoanodes were also investigated for photocharging. Venugopal et al. demonstrated that the photocharging effect can also be observed in $CuWO_4$ photoanodes. [10] Here again it was shown that the effect was reversible under dark conditions and could be recharged by subjecting the photoelectrode again to prolonged illumination under open circuit conditions. The current voltage response before and after photocharging of $CuWO_4$ photoanodes is shown in Figure 2.4 (a). The photocharged $CuWO_4$ photoanodes also showed similar response to hole scavenger experiments, suggesting the improvement of the photocurrent was due to both bulk and surface enhancements, similar to photocharged $BiVO_4$ photoanodes. The reversibility and rechargeability of the photocharging effect of $CuWO_4$ photoanodes is shown in Figure 2.4 (b). Similarly, Deng et al. demonstrated the photocharging effect on Fe_2TiO_5/Fe_2O_3 photoanodes [11], showing similar behavior as $BiVO_4$ and $CuWO_4$ photoanodes, as shown in Figure 2.4 (c-d). The photocharging effect has been demonstrated in other metal oxide photoanodes such as Bi_4-TaO_8X [12], Ti doped Fe_2O_3 [13] and Mo doped $BiVO_4$ [14] photoanodes. The reproducibility of a near identical response to photocharging has been demonstrated in different metal oxide photoelectrodes, suggesting the possibility of a common universal mechanism behind the photocharging treatment. To investigate this further, several advanced operando characterization experiments were performed on $BiVO_4$ photoelectrodes and the results are discussed below.

2
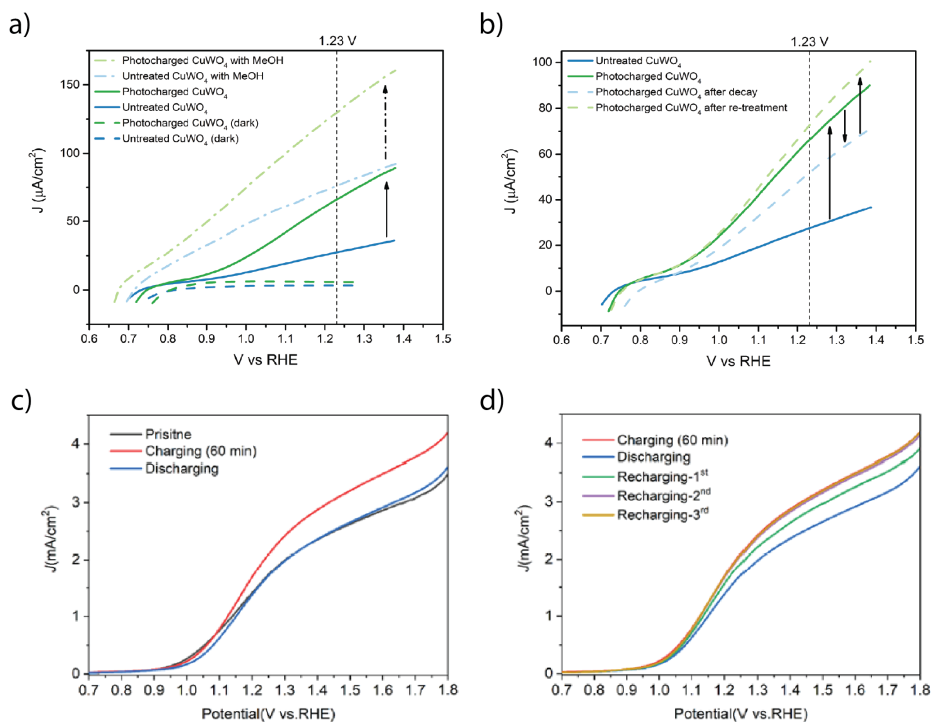
Figure 2.4: (a) Current density vs applied voltage for photocharging treatment performed on $CuWO_4$ photoanodes, clearly showing the improvement from the photocharging treatment. Here methanol was used as a hole scavenger, for the hole scavenger experiments. (b) Current density vs applied voltage plot showing the photocharging, discharging in dark and re-charging of $CuWO_4$ photoanodes. (c) Current density vs applied voltage plot for photocharging treatment performed on Fe_2TiO_5/Fe_2O_3 photoelectrodes. The plot also shows the J-V performance of the discharged electrode. (d) Current density vs voltage plot for photocharging treatment on Fe_2TiO_5/Fe_2O_3 photoelectrodes, showing the J-V characteristics after discharge-recharge cycles. The plots (a-b) and (c-d) were adapted with permission from ref [10] and [11], respectively.

Liu et al. performed intensity modulated photocurrent spectroscopy (IMPS) on $BiVO_4$ photoanodes, before and after the photocharging treatment. [9] Since this impedance technique uses light modulation to probe the photoelectrode, it is a good technique to study the surface rate constants. Using this technique, Liu et al. extracted the rate constants for the charge transfer and charge recombination events at the surface of $BiVO_4$ before and after photocharging, as shown in Figure 2.5. It was observed that the rate constant of recombination decreased post photocharging, as shown in Figure 2.5 (b), indicating a decrease in the surface recombination of charge carriers in photocharged samples. In addition, it was also observed that there is an increase in the rate constant for the charge transfer process, post photocharging, as shown in Figure 2.5 (a). The first observation would suggest a better charge separation at the $BiVO_4$ surface post photocharging, while the improvement in rate constant for charge transfer process would suggest a change in the surface characteristics of photocharged $BiVO_4$ with respect to
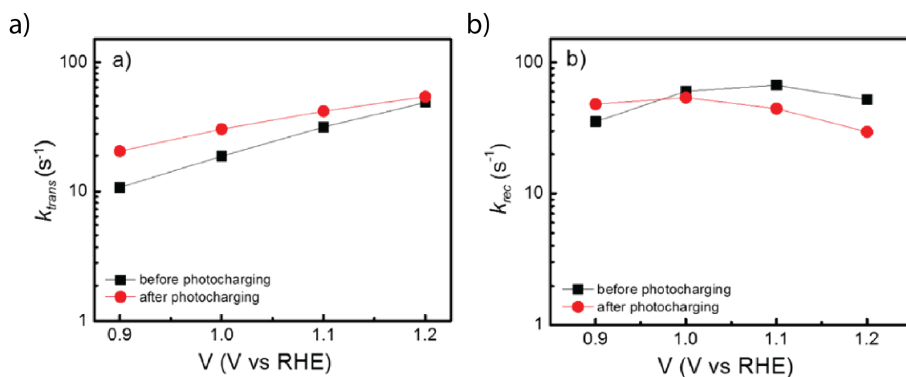
Figure 2.5: (a) Rate constant of charge transfer, extracted from the IMPS spectra. (b) Rate constant of recombination of charge carriers, extracted from the IMPS spectra. The plots were adapted with permission from ref [9]

untreated $BiVO_4$ photoanodes that improves catalytic efficiency.

To further study the changes in the bulk of the $BiVO_4$ during photocharging, Trześniewski and Firet et al. performed X-ray diffraction studies (XRD) [8, 15] on the untreated and photocharged $BiVO_4$ samples shown in Figure 2.6 (a). These plots revealed diffractograms of the pristine and photocharged $BiVO_4$ were near identical, indicating that the average bulk of $BiVO_4$ remained intact during the photocharging treatment and that there were no additional bulk lattice strain or stress that could be responsible for the enhancements. In-situ X-ray absorption spectroscopy (XAS) studies were also performed by Trześniewski et al. to study the effect of the photocharging treatment on the average bulk vanadium oxidation state and its local environment. [8] The vanadium K edge spectra collected from this study under different conditions is shown in Figure 2.6 (b). The XAS spectra in the X-Ray absorption near edge structure (XANES) range for the photocharged and reference samples show near perfect overlap with the ex situ samples, indicating again that the bulk structure remains intact during the photocharging treatment.

Grazing incidence X-ray Raman Scattering (XRS) experiments were performed by Firet et al. to study the changes in the $BiVO_4$ near-surface due to photocharging. [15] Unlike the XRD and XAS measurements, which analyzed the changes in complete bulk $BiVO_4$, the grazing incidence XRS analyzes the changes in the first ~ 60 nm from the surface. This region roughly overlaps with the space charge region of the $BiVO_4$ photoanode [16], and hence the XRS measurements indirectly observe the changes within the space charge region due to the photocharging treatment. The vanadium L_2 and L_3 and oxygen K edge of the reference (as-deposited), dark (sample left in contact with electrolyte under open-circuit conditions in the dark) and photocharged $BiVO_4$ were probed with hard X-rays under ambient conditions and results are presented in Figure 2.6 (c). The vanadium L edge spectra involves transitions from the 2p orbital to the empty 3d orbital. The first main peak between 515 and 520 eV corresponds to the V L_3 edge, while the main peak be-

2

tween 521 and 528 eV corresponds to the V L_2 edge. Due to the O 2p – V 3d hybridization, the L_3 and L_2 peaks are split into e_g and t_{2g} states [17], as shown in Figure 2.6 (c). The O K edge spectra extend upwards from 528 eV. This involves transitions from O 1s to unoccupied O 2p orbitals. The peak at 531 eV and the shoulder peak at 530 eV again show the O 2p – V 3d hybridization and the peaks are split into e_g and t_{2g} states because of this. The peak at 534 eV corresponds to the antibonding π O 2p – Bi 6p states. [18, 19] The peak at 540 eV is corresponding to the excitation to the antibonding σ states originating from the hybridization of both V 4s and Bi 6s and O 2p. [17, 20] The XRS spectra in Figure 2.1 also contains the spectra of reference vanadium samples with +4 and +5 vanadium oxidation states, together with the reference, dark and photocharged $BiVO_4$ samples. The peaks of the reference V^{4+} samples are shifted to lower binding energies compared to the V^{5+} samples. The spectra of the dark and photocharged $BiVO_4$ sample is in between the V^{4+} and V^{5+} reference samples. To further elucidate this, a multiplet analysis was performed on a hypothetical bismuth vanadium oxide, with different vanadium oxidation states, to predict its L edge spectra as shown in Figure 2.1. From this analysis, it is clear that the L_3 and L_2 peak width and ratios can indicate the oxidation state of vanadium in the analyzed compound. Here the L_3/L_2 peak ratio of the photocharged sample is lower in comparison to that of the dark sample, indicating a reduction in the oxidation state of vanadium due to photocharging.

Another main difference between the dark and photocharged $BiVO_4$ spectra in Figure 2.6 (c) is the filling of the V 3d states of the dark sample with electrons, as observed with the difference in the peak height ratio of the V 3d – O 2p peak and the main mixed metal sp - O 2p peak in the O K edge spectra. The lowering of the V 3d – O 2p pre-peak with respect to the main peak is an indication of the filling of the d states. Therefore, the dark samples seem to have a higher concentration of electrons in its d states compared to the photocharged sample. To further elucidate this, ab-initio simulations were performed by Firet et al. at the O K edge and the results were compared to the experimental XRS spectra, as shown in Figure 2.6 (d). Two semi-empirical parameters, dilatorb and screening parameters, were used to simulate the peak ratio. The dilatorb parameter provided the ability to consider the degree of ionicity of the oxygen in the lattice, within the simulations. The screening parameter allowed to account for a non-fully screened hole in the absorbing atom, i.e. part of the electron charge in the conduction band is missing. The best fitting results are shown in Figure 2.6 (d). The dark sample was fitted with a screening parameter of 0.1 and a dilatorb of 0.1, while the photocharging sample was fitted with a screening parameter of 0.2 and a dilatorb of 0.1. The default screening parameter is 0, indicating full screening. The higher screening parameter value for the photocharged sample is an indication of less electrons in the conduction band of the photocharged sample. Since the XRS analysis region overlaps with the space charge region of the photoanode, this result could be interpreted as an improved band bending within the space charge region for the photocharged sample. This improved band bending will remove electrons from the conduction band of the photocharged sample, leading to a higher screening parameter within this region in comparison to the dark sample. These results suggested that the photocharging treatment resulted in an improved band bending within the space charge region. This increased band bending improved the sep-
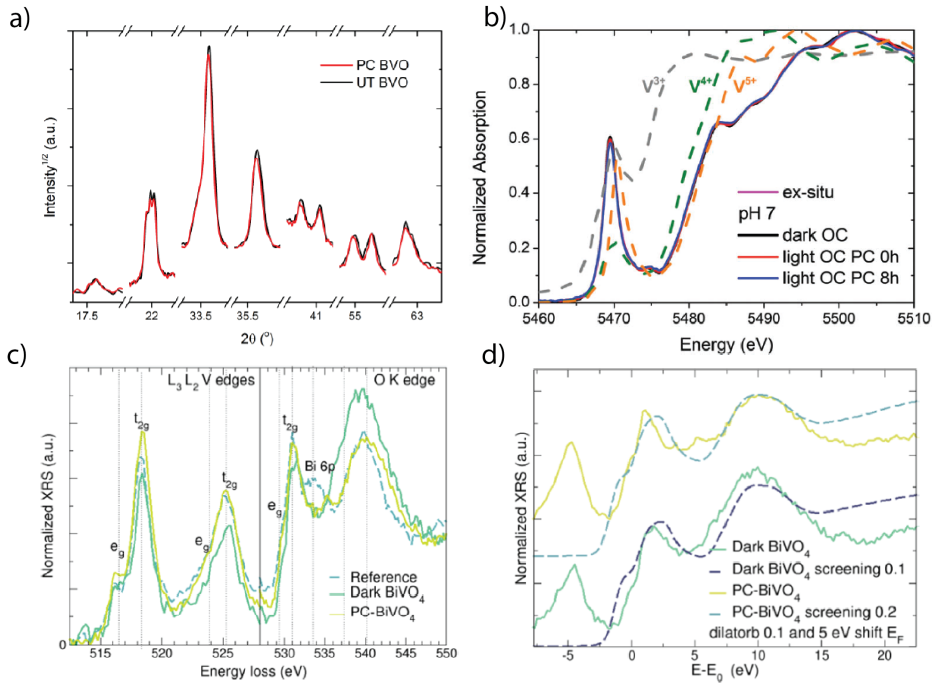
Figure 2.6: (a) XRD plots of the untreated and photocharged $BiVO_4$ photoanodes. (b) Vanadium K edge spectra obtained from in-situ XAS studies on $BiVO_4$ under different conditions. The spectra of reference vanadium species at different oxidation states is also included here. (c) Normalized vanadium L_3 and L_2 and oxygen K edge spectra from the grazing incidence XRS experiments performed on the reference, dark and $BiVO_4$ samples. (d) The oxygen K edge spectra from the XRS studies overlaid with the best representing ab-initio simulations, obtained by varying the dilatorb and screening parameters. The plots (a-b) and (c-d) were adapted with permission from ref [8] and [15], respectively.

aration of charge carriers and suppressed their recombination, leading to improved PEC performance of the photocharged samples.

To better understand the mechanisms for these changes near the surface of the $BiVO_4$ due to photocharging, the photocharged $BiVO_4$ samples were studied using X-ray photoelectron spectroscopy (XPS). The Bi 4f, V 2p, O 1s, B 1s and the valence band spectra of the reference, dark and photocharged $BiVO_4$ samples were acquired and the results are presented in Figure 2.7. The Bi 4f spectra showed a slight broadening and a shift to the lower binding energies upon photocharging. This was accompanied by the appearance of boron peak in the B 1s spectra of the photocharged sample, as shown in Figure 2.7 (b). The V 2p and O 1s spectra also saw a shift to lower binding energies. There was a decrease in the concentration of vanadium post photocharging, as evidenced by the diminishing V 2p peaks in Figure 2.7 (c). In addition, the O 1s peak had a new shoulder peak at 531 eV, which is typically attributed to oxygen containing surface adsorbed species [21–23] but could more likely be oxidized lattice oxygen (O_2^{2-}) ion. [24] The valence band spectra, which represents the density of states, also saw a broadening and a

shift to the lower binding energies. The broadening and shifting of the Bi 4f and valence band spectra was partly assigned to the formation of a bismuth borate layer at the surface of bismuth vanadate during photocharging. The Bi-O-B bonds have an XPS peak at 158.7 eV [25] and hence broadens the spectra of photocharged $BiVO_4$. Similar observations were made by Favaro et al. using in-situ hard X-ray XPS on $BiVO_4$ photoanodes [26], as shown in Figure 2.2. They observed the formation of a bismuth phosphate layer on $BiVO_4$ upon photocharging. The new shoulder peak of the O 1s spectra can also partly be assigned to the oxygen from the surface adsorbed borate species.

The XPS spectra can also shift to lower binding energies with increased band bending. This was previously demonstrated on $BiVO_4$ photoanodes by Hermans et al. [27], by depositing ultrathin metal oxide layers on the $BiVO_4$ and studying the peak shifts with XPS. Since the XRS studies already indicated the presence of improved band bending within the photocharged samples, the shift in the XPS spectra to lower binding energies of the photocharged samples could be ascribed to this. However, the magnitude of such electronic shifts should be the same for the XPS spectra of all the elements analyzed, which is not the case here. Therefore, the shift of the XPS spectra to lower binding energies is considered to be a result of improved band bending and a surface chemical change induced shifting.

The photocharging effect was only observed in illuminated conditions and in the presence of an electrolyte. This indicates that both illumination and the photoanode/electrolyte interface are important in this context. Therefore, to further study this interface under illuminated conditions, an operando infrared spectroscopy setup was built. [28] A schematic of this setup is shown in Figure 2.8 (a). This setup was used to study the changes at the $BiVO_4$/electrolyte under photocharging, decay and applied potential conditions. In the $BiVO_4$ reference spectrum in Figure 2.3, the broad peaks at 682 and 802 cm^{-1} is assigned to the VO_4^{3-} asymmetric stretching vibrations, while the peak at 894 cm^{-1} is assigned to the VO_4^{3-} symmetric stretching vibration. The peak at 640 cm^{-1} is assigned to the Bi-O symmetric stretching vibration. [29–33] The spectra during photocharging in borate buffer electrolyte and ultra-pure water are shown in Figure 2.8 (b) and Figure 2.4. A negative going peak was observed here at 682 cm^{-1}, with shoulder negative going peaks to its left. This is the region for V-O symmetric and asymmetric stretching vibrations. A negative going peak at 682, 802 and 894 cm^{-1} is an indication of a decrease in the concentration of vanadium at the surface of $BiVO_4$ during photocharging. This was the case for both ultra-pure water and borate buffer electrolyte. The Bi-O stretching vibration peak at 640 cm^{-1}, remained intact during the photocharging process. In addition, a broad positive going peak was also observed in the OH stretching vibration region (3000 – 3750 cm^{-1}) [34–37], indicating an increase in the concentration of water near the surface of $BiVO_4$ during the photocharging process. The spectra obtained in the borate buffer electrolyte has additional positive trending features at 1026 and ~ 800 cm^{-1}, due to the stretching vibration of the borate species. [38–40] An increasing peak here is again an indication of the increase in concentration of the borate anion near the $BiVO_4$ surface during photocharging. The changes in the spectra at 1115 and 620 cm^{-1} are due to the changes in the Silicon internal reflection element during il-
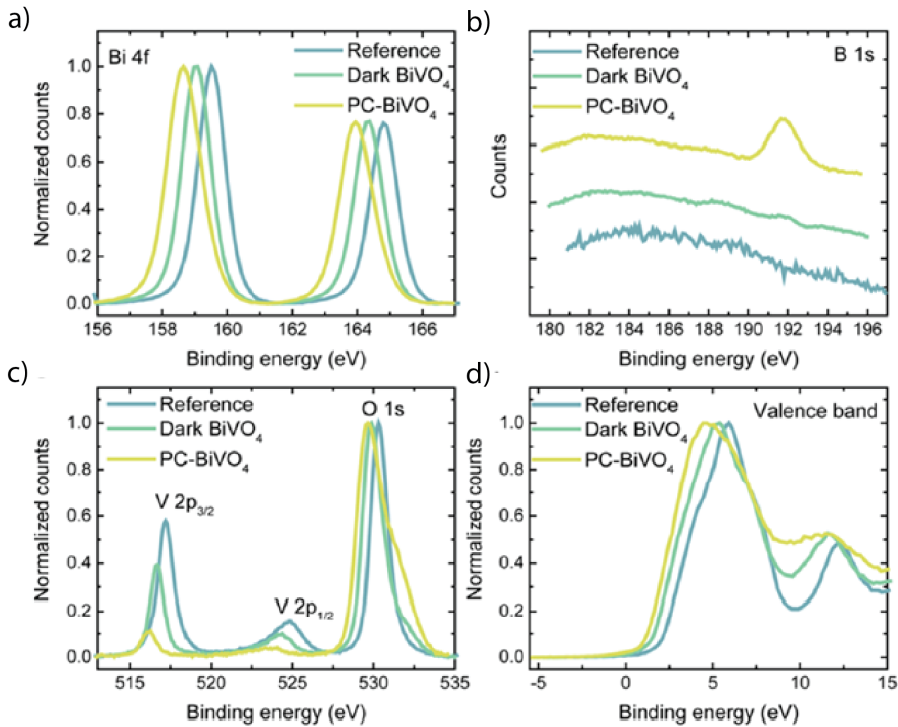
Figure 2.7: (a) Bi 4f (b) B 1s (c) V 2p and O 1s and (d) Valence band XPS of reference, dark and photocharged BiVO$_4$ photoanodes. The spectra was corrected for C1s peak shift. The figure was adapted with permission from ref [15].

lumination. [41, 42] The BiVO$_4$/electrolyte interface was also studied during the decay process, after photocharging, as shown in Figure 2.8 (c) and Figure 2.4. Here a decrease in the concentration Bi-O stretching vibrations was observed, indicating a removal of bismuth ions from the surface during the decay process. The regions for V-O stretching vibrations remained fairly intact. Since the concentration changes observed here were not reversible in the light and dark conditions, the concentration decrease is an indication the permanent removal of that species from the surface of BiVO$_4$. These results indicate that the vanadium ions are preferentially removed during the photocharging process, while the bismuth ions are preferentially removed during the decay process. The removal of vanadium ions changes the Bi:V ratio at the surface, making the surface more bismuth rich during photocharging. During the decay process, with the removal of bismuth ions, the Bi:V ratio at the BiVO$_4$ surface is restored close to its initial state. The BiVO$_4$/electrolyte interface was also studied during applied potential experiments in illuminated and dark conditions, as shown in Figure 2.5. During the potential step experiments under illuminated conditions, decrease in the concentrations of both bismuth and vanadium was observed. Similar observations were also made by Zhang et al.

using online inductively coupled plasma mass spectroscopy measurements. [43] On the contrary, during the potential cycling experiments in the dark conditions, the spectra was completely reversible, indicating that the bismuth and vanadium ions remained on the $BiVO_4$ surface during the potential step experiments in the dark.

The preferential dissolution of vanadium ions under illuminated OCP conditions alters the surface Bi/V ratio and leaves behind a bismuth rich surface. This bismuth rich surface ($BiV_{1-x}O_y$) has a higher band position when compared to pristine $BiVO_4$ [44], creating a heterojunction with an increased band bending. This improved band bending was also confirmed by the XRS results. The improved band bending will improve the bulk charge separation within the photoanode, resulting in enhanced PEC performance after prolonged illumination. The infrared spectroscopy results also showed the preferential dissolution of bismuth ions under dark conditions, after photocharging. This dissolution further restores the Bi/V ratio at the surface, bringing the performance back to the pre-photocharging levels. These processes are schematically shown in Figure 2.9. The temporary improvement in PEC performance was initially viewed as a performance improvement strategy. The increasing photocurrent and the long timescale (minutes – hours) required to produce this enhancement inadvertently masked the short term (seconds – minutes) stability evaluation studies performed on these materials, such as the oxygen evolution reaction (OER) faradic efficiency measurements over time. However, with further research, it was clear that this was a temporary enhancement induced by the degradation of the photoanode itself.
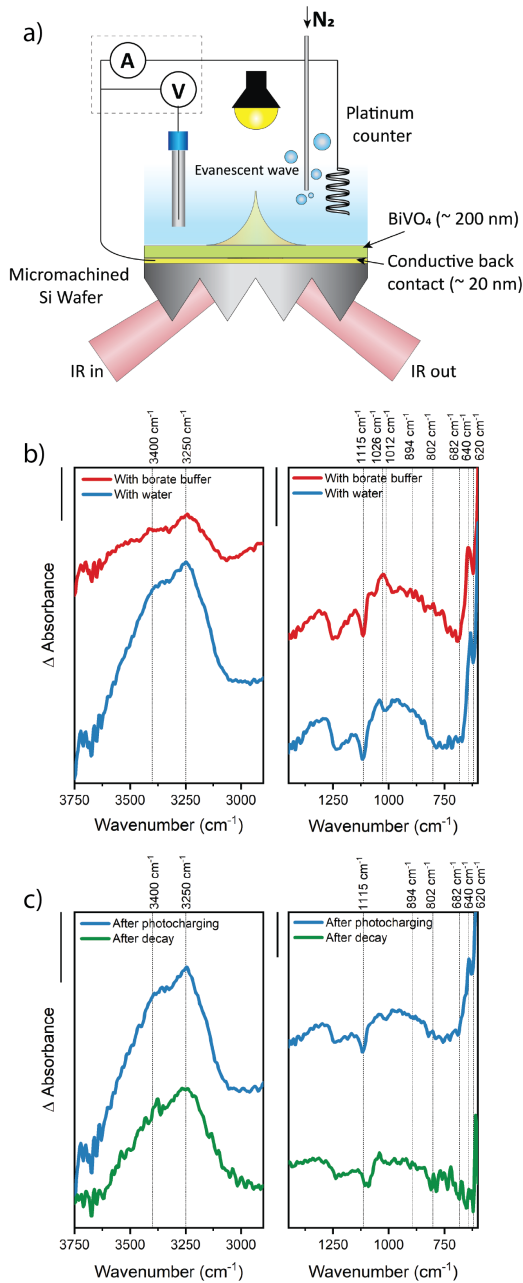
Figure 2.8: (a) Schematic of the operando photoelectrochemical attenuated total reflection infrared spectroscopy setup used in this study. (b) Comparison of the infrared spectra after 3 hours of photocharging in borate buffer electrolyte and ultra-pure water. (c) Comparison of the infrared spectra after 3 hours of photocharging and 2 hours of decay in ultra-pure water. The scale bar is 0.001 units. The plots were adapted with permission from ref [28].

2
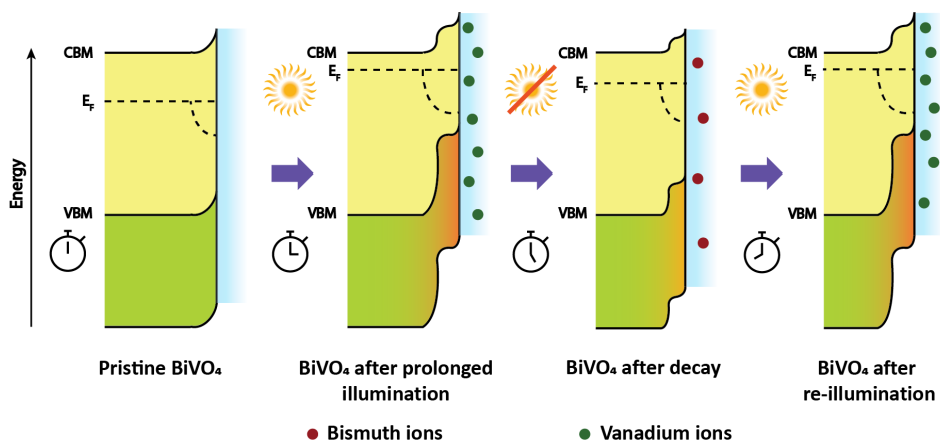
Figure 2.9: Schematic showing the removal of vanadium and bismuth ions from the BiVO$_4$ photoanode surface during the photocharging and decay cycles, respectively, and associated changes in the space charge region of the BiVO$_4$ photoanode. Figure was adapted with permission from ref [15].

2.4. Mechanism of degradation

The degradation of the photoanode material over time, described above, also shines some light into the mechanism behind this degradation. The observation of a decrease in the oxidation state of surface vanadium species and its dissolution after this prolonged illumination is a suggestion of a surface electron induced reduction reaction of surface vanadium species. In addition, an increase in the oxidation state of surface oxygen species, as seen with the emergence of a shoulder peak at 531 eV in the O 1s XPS spectra, under similar conditions is an indication of oxidation of surface lattice oxygen species by energetic holes. This peroxide formation is an intermediate step in the O_2/H_2O redox chemistry, with a reduction potential of 1.23 V vs NHE. This oxidation of lattice oxygen species is considered to be a part of the OER mechanism in many OER catalysts. [45–47] The reduced surface vanadium and the oxidized surface oxygen can also be oxidized and reduced back to their initial oxidation states by energetic holes and electrons, respectively. The standard reduction potentials of these reactions, shown in Figure 2.10, suggest that these steps are thermodynamically feasible. This reduction-oxidation cycle of surface cation/anion species of the photoelectrode is normally considered as "surface recombination" pathways for photogenerated electrons and holes within these materials. This surface recombination is considered to have a negative impact on the device efficiency, since energetic charge carriers are lost through this unwanted step. In case of $BiVO_4$, the vanadium species is reduced from its +5 oxidation state to +4/+3 oxidation states, which are aqueous soluble species and hence readily dissolve into the electrolyte solution. In case of other metal oxide photoanodes, the cation and anion species will undergo this sequential oxidation/reduction cycles as part of this surface recombination step. Equations (1)-(7), shows that these steps are energetically possible for most relevant transition metal oxide species. This dynamic cycling will result in loss of material from the surface over time, impacting the long-term stability of the photoelectrode. The above observations of the photoelectrode dissolution and degradation suggests that these surface recombination process have more serious implications than just its impact on the device efficiency.

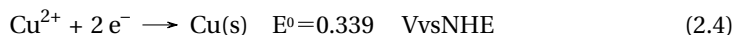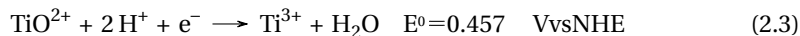$$FeOH^{2+} + H^+ + e^- \longrightarrow Fe^{2+} + H_2O \quad E^0{=}0.900 \quad VvsNHE \tag{2.1}$$

$$FeOOH(s) + 3\,H^+ + e^- \longrightarrow Fe^{2+} + 3\,H_2O \quad E^0{=}0.740 \quad VvsNHE \tag{2.2}$$

$$TiO^{2+} + 2\,H^+ + e^- \longrightarrow Ti^{3+} + H_2O \quad E^0{=}0.457 \quad VvsNHE \tag{2.3}$$

$$Cu^{2+} + 2\,e^- \longrightarrow Cu(s) \quad E^0{=}0.339 \quad VvsNHE \tag{2.4}$$

$$Cu^{2+} + e^- \longrightarrow Cu^+ \quad E^0{=}0.161 \quad VvsNHE \tag{2.5}$$

$$WO_3 + 2\,H^+ + 2\,e^- \longrightarrow WO_2 + H_2O \quad E^0{=}0.036 \quad VvsNHE \tag{2.6}$$

$$W^{6+} + e^- \longrightarrow W^{5+} \quad E^0{=}0.26 \quad VvsNHE \tag{2.7}$$
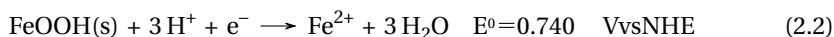
The dynamic oxidation/reduction processes at the photoanode surface, initiated by the surface recombination processes, implies that a photoelectrode will have more degradation pathways in comparison to a metallic electrode. This would suggest that photoelectrodes will be harder to optimize for stability in comparison to a metallic electrode.

2
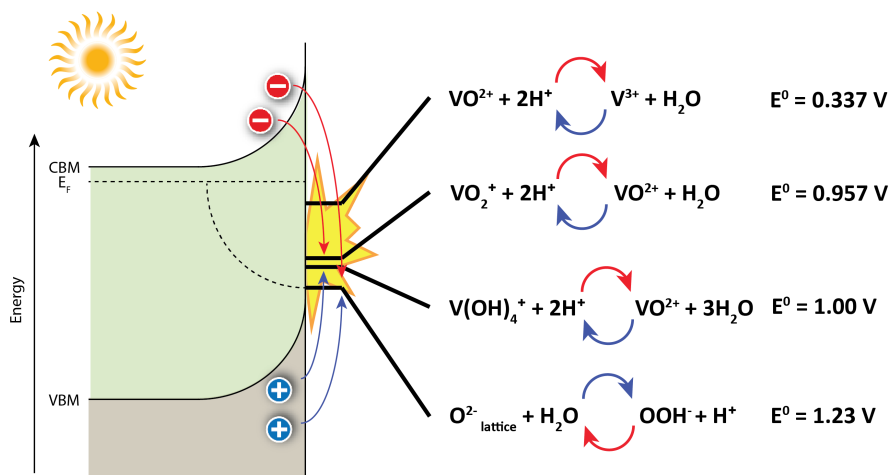
Figure 2.10: Schematic showing the thermodynamically viable redox cycling of the surface anion/cation species of the photoelectrode via surface recombination of charge carriers.

Typically, only the thermodynamic stability of the bulk material within the operational potential window is considered during material selection of these photoelectrodes, and not much attention is given to the surface reactions of individual cation/anion species within the material. From the observations mentioned above, it is obvious that the surface reactions will have an equally important role in effecting the material stability and hence considering this aspect during material selection should be made a high priority.

2.5. Concluding remarks

The stability of a photoelectrode would most likely be a difficult problem to address purely from a material perspective. Solving this challenge would require finding a metal cationic/anionic species that forms a stable semiconducting photoelectrode, and does not undergo surface redox reactions within a large operational potential window. They should at the same time satisfy all the other requirements of a photoelectrode.[48] This will be inherently very difficult to achieve since the research community is already struggling to optimize the photoelectrode properties based on its other requirements.

In the context of water splitting reaction, the very high potentials required for the OER reaction and its inherently slow reaction kinetics implies that the surface charge carriers will be always be competing between the non-faradaic redox reactions at the photoelectrode surface and the faradaic OER reaction, accelerating the photoelectrode degradation in these environments. A better application for such PEC systems would be in lesser thermodynamically demanding and kinetically faster reaction environments. This approach could potentially bring the degradation rates down to appreciable levels and can bring PEC devices closer to practical applications.

2

2.6. Supplementary information
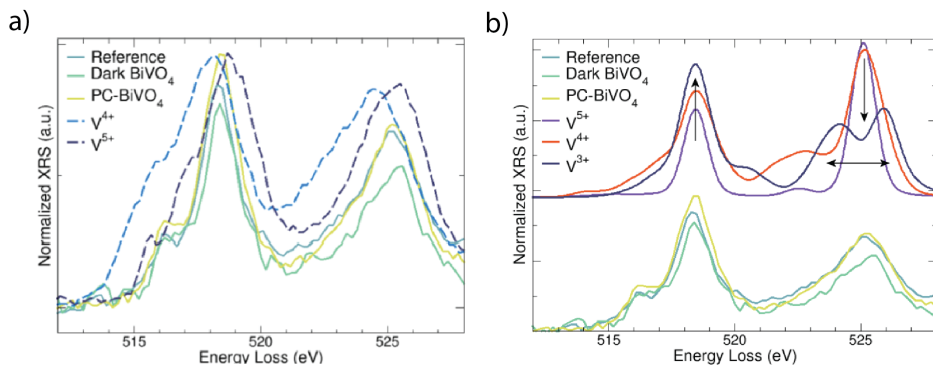
Supplementary Figure S2.1: (a) Vanadium L edge spectra obtained from the XRS measurements. The spectra of the reference V^{5+} and V^{4+} samples are also included in this plot. (b) Multiplet analysis performed on different bismuth vanadium oxides reveal the nature of the vanadium L_3 and L_2 peaks of different peak ratios and peak shapes. Plot adapted with permission from ref [15].

a)

b)
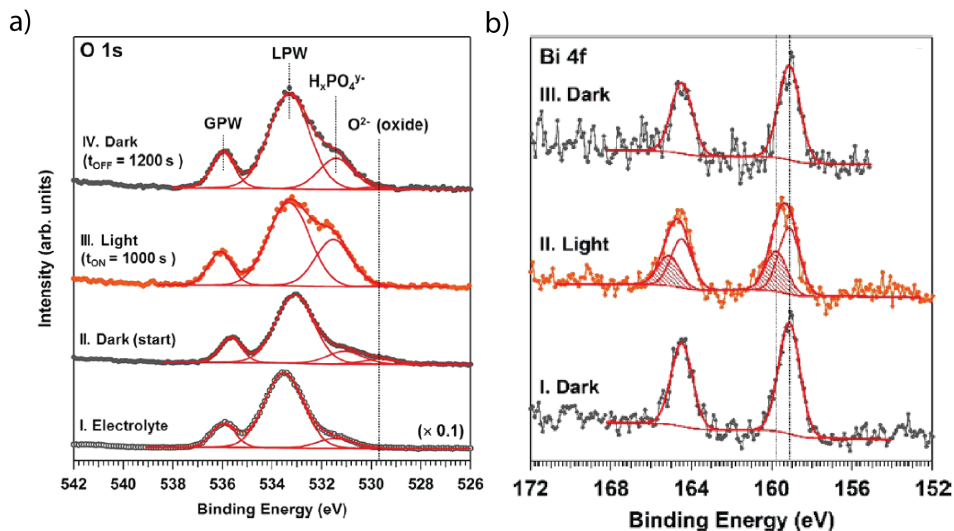
Supplementary Figure S2.2: (a) O 1s spectra obtained using the in-situ XPS measurements on the $BiVO_4$/electrolyte interface under dark and illuminated conditions, showing the emergence of the shoulder peak at 531.5 eV under illumination. (b) Bi 4f spectra obtained using the in-situ XPS measurements on the $BiVO_4$/electrolyte interface under dark and illuminated conditions, showing the broadening of the Bi 4f spectra under illumination. The plots were adapted with permission from ref [26].
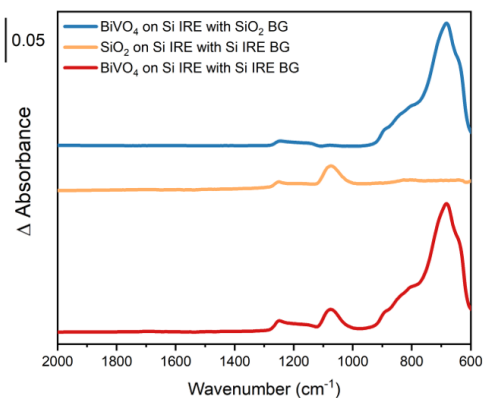
Supplementary Figure S2.3: Infrared spectra of the $BiVO_4$ sample with the Si internal reflection element (IRE) and SiO_2 on Si IRE as the background. Reference spectra of the SiO_2 on the Si IRE element is also shown. Plots were adapted with permission from ref [28].

2
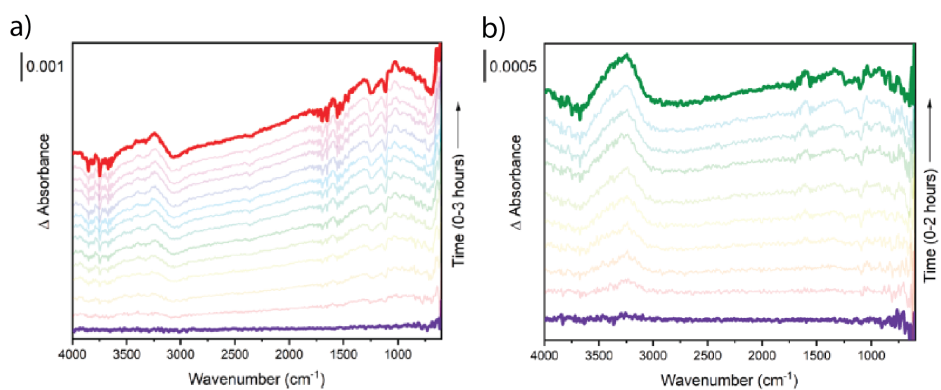
Supplementary Figure S2.4: (a) Transient infrared spectra of the $BiVO_4$/electrolyte interface during the photocharging process. $BiVO_4$/electrolyte interface at $t = 0$ mins after illumination was chosen as the background. (b) Transient infrared spectra of the $BiVO_4$/electrolyte interface during the decay process. $BiVO_4$/electrolyte interface at $t = 0$ mins after switching off the illumination was chosen as the background. Plots were adapted with permission from ref [28].
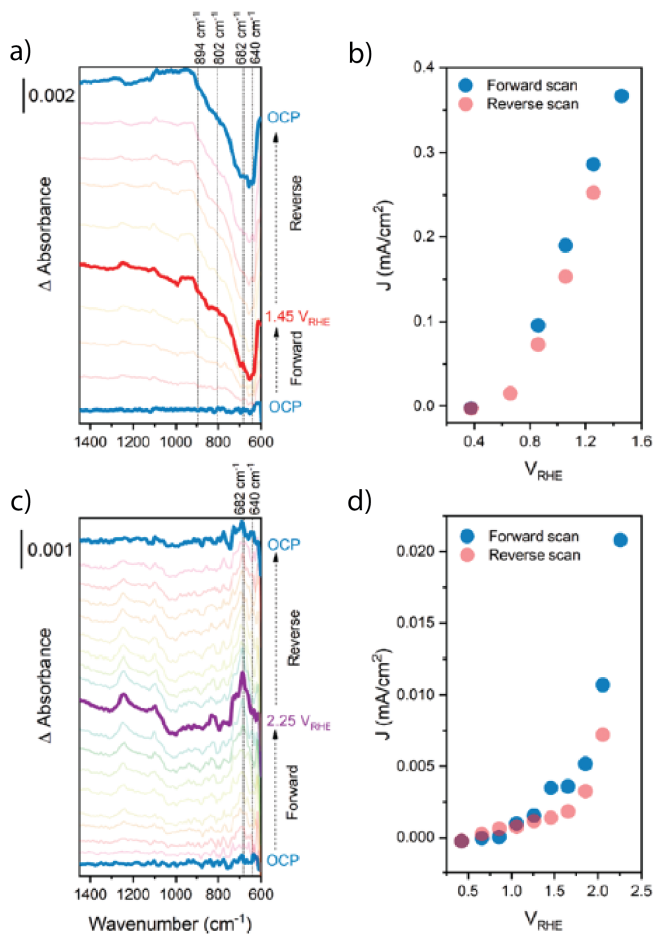
Supplementary Figure S2.5: (a) Infrared spectra of the $BiVO_4$/electrolyte interface during voltage step experiments under illumination. (b) Current density vs applied voltage plot under illumination during the voltage step experiments. (c) Infrared spectra of the $BiVO_4$/electrolyte interface during voltage step experiments under dark conditions. (d) Current density vs applied voltage plot under dark conditions during the voltage step experiments. Plot was adapted with permission from ref [28] .

2.7. References

(1) V. Masson-Delmotte et al. *IPCC, 2018: Global warming of 1.5° C. An IPCC special report on the impacts of global warming of 1.5° C above pre-industrial levels and related global greenhouse gas emission pathways, in the context of strengthening the global response to the threat of cli*; tech. rep.; 2018.

(2) Roel van de Krol, M. G., *Photoelectrochemical Hydrogen Production.*

(3) Sixto Giménez, B. J., *Photoelectrochemical solar fuel production*; Springer: Switzerland, 2016.

(4) Jacobsson, T. J.; Fjällström, V.; Sahlberg, M.; Edoff, M.; Edvinsson, T. *Energy and Environmental Science* **2013**, *6*, 3676–3683.

(5) Cheng, W. H.; Richter, M. H.; May, M. M.; Ohlmann, J.; Lackner, D.; Dimroth, F.; Hannappel, T.; Atwater, H. A.; Lewerenz, H. J. *ACS Energy Letters* **2018**, *3*, 1795–1800.

(6) Trześniewski, B. J.; Smith, W. A. *Journal of Materials Chemistry A* **2016**, *4*, 2919–2926.

(7) Bard, A. J.; Faulkner, L. R.; White, H. S., *Electrochemical methods: fundamentals and applications.* John Wiley & Sons: 2022.

(8) Trześniewski, B. J.; Digdaya, I. A.; Nagaki, T.; Ravishankar, S.; Herraiz-Cardona, I.; Vermaas, D. A.; Longo, A.; Gimenez, S.; Smith, W. A. *Energy & Environmental Science* **2017**, *10*, 1517–1529.

(9) Liu, E. Y.; Thorne, J. E.; He, Y.; Wang, D. *ACS Applied Materials and Interfaces* **2017**, *9*, 22083–22087.

(10) Venugopal, A.; Smith, W. A. *Faraday Discussions* **2019**, *215*, 175–191.

(11) Deng, J.; Lv, X.; Zhong, J. *Journal of Physical Chemistry C* **2018**, *122*, 29268–29273.

(12) Tao, X.; Shi, W.; Zeng, B.; Zhao, Y.; Ta, N.; Wang, S.; Adenle, A. A.; Li, R.; Li, C. *ACS Catalysis* **2020**, *10*, 5941–5948.

(13) Xie, J.; Yang, P.; Liang, X.; Xiong, J. *ACS Applied Energy Materials* **2018**, *1*, 2769–2775.

(14) Tayebi, M.; Tayyebi, A.; Lee, B. K. *Solar Energy* **2019**, *191*, 427–434.

(15) Firet, N. J.; Venugopal, A.; Blommaert, M. A.; Cavallari, C.; Sahle, C. J.; Longo, A.; Smith, W. A. *Chemistry of Materials* **2019**, *31*, 7453–7462.

(16) Peter, L. M.; Gurudayal; Wong, L. H.; Abdi, F. F. *Journal of Electroanalytical Chemistry* **2018**, *819*, 447–458.

(17) Jovic, V.; Laverock, J.; Rettie, A. J. E.; Zhou, J.-S.; Mullins, C. B.; Singh, V. R.; Lamoureux, B.; Wilson, D.; Su, T.-Y.; Jovic, B.; Bluhm, H.; Söhnel, T.; Smith, K. E. *Journal of Materials Chemistry A* **2015**, *3*, 23743–23753.

(18) Cooper, J. K.; Gul, S.; Toma, F. M.; Chen, L.; Glans, P.-A.; Guo, J.; Ager, J. W.; Yano, J.; Sharp, I. D. *Chemistry of Materials* **2014**, *26*, 5365–5373.

(19)   Jovic, V.; Rettie, A. J. E.; Singh, V. R.; Zhou, J.; Lamoureux, B.; Buddie Mullins, C.;
       Bluhm, H.; Laverock, J.; Smith, K. E. *Physical Chemistry Chemical Physics* **2016**, *18*,
       31958–31965.

(20)   Zhao, Z.; Li, Z.; Zou, Z. *Physical Chemistry Chemical Physics* **2011**, *13*, 4746.

(21)   Kim, Y. S.; Ansari, S. G.; Ansari, Z. A.; Wahab, R.; Shin, H. S. *Review of Scientific
       Instruments* **2010**, *81*, 1–5.

(22)   Kwoka, M.; Ottaviano, L.; Passacantando, M.; Santucci, S.; Czempik, G.; Szuber, J.
       Thin Solid Films **2005**, *490*, 36–42.

(23)   Kaciulis, S.; Mattogno, G.; Galdikas, A.; Mironas, A.; Setkus, A. *Journal of Vacuum
       Science & Technology A: Vacuum, Surfaces, and Films* **1996**, *14*, 3164–3168.

(24)   Dupin, J. C.; Gonbeau, D.; Vinatier, P.; Levasseur, A. *Physical Chemistry Chemical
       Physics* **2000**, *2*, 1319–1324.

(25)   Oprea, B.; Radu, T.; Simon, S. *Journal of Non-Crystalline Solids* **2013**, *379*, 35–39.

(26)   Favaro, M.; Abdi, F. F.; Lamers, M.; Crumlin, E. J.; Liu, Z.; Van De Krol, R.; Starr, D. E.
       Journal of Physical Chemistry B **2018**, *122*, 801–809.

(27)   Hermans, Y.; Murcia-López, S.; Klein, A.; van de Krol, R.; Andreu, T.; Morante, J. R.;
       Toupance, T.; Jaegermann, W. *Physical Chemistry Chemical Physics* **2019**, *21*, 5086–
       5096.

(28)   Venugopal, A.; Kas, R.; Hau, K.; Smith, W. A. *Journal of the American Chemical So-
       ciety* **2021**, *143*, 18581–18591.

(29)   Baral, B.; Parida, K. *Inorganic Chemistry* **2020**, *59*, 10328–10342.

(30)   Frost, R. L.; Henry, D. A.; Weier, M. L.; Martens, W. *Journal of Raman Spectroscopy*
       2006, *37*, 722–732.

(31)   Gotić, M.; Musić, S.; Ivanda, M.; Šoufek, M.; Popović, S. *Journal of Molecular Struc-
       ture* **2005**, *744-747*, 535–540.

(32)   Longchin, P.; Pookmanee, P.; Satienperakul, S.; Sangsrichan, S.; Puntharod, R.; Kruefu,
       V.; Kangwansupamonkon, W.; Phanichphant, S. *Integrated Ferroelectrics* **2016**, *175*,
       18–24.

(33)   Pookmanee, P.; Kojinok, S.; Puntharod, R.; Sangsrichan, S.; Phanichphant, S. *Fer-
       roelectrics* **2013**, *456*, 45–54.

(34)   Choi, J. H.; Cho, M. *Journal of Chemical Physics* **2013**, *138*, DOI: 10.1063/1.
       4802991.

(35)   De Marco, L.; Carpenter, W.; Liu, H.; Biswas, R.; Bowman, J. M.; Tokmakoff, A. *Jour-
       nal of Physical Chemistry Letters* **2016**, *7*, 1769–1774.

(36)   Salucci, P. et al. *Science* **2003**, *301*, 1698–1702.

(37)   Auer, B. M.; Skinner, J. L. *Journal of Chemical Physics* **2008**, *128*, DOI: 10.1063/1.
       2925258.

(38)   Peak, D.; Luther, G. W.; Sparks, D. L. *Geochimica et Cosmochimica Acta* **2003**, *67*,
       2551–2560.

(39) Scharifker, B. R.; Habib, M. A.; Carbajal, J. L.; Bockris, J. O. *Surface Science* **1986**, *173*, 97–105.

(40) Lefèvre, G. *Advances in Colloid and Interface Science* **2004**, *107*, 109–123.

(41) Amekura, H.; Umeda, N.; Okubo, N.; Kishimoto, N. *Nuclear Instruments and Methods in Physics Research, Section B: Beam Interactions with Materials and Atoms* **2003**, *206*, 1101–1105.

(42) Hu, Q.; Suzuki, H.; Gao, H.; Araki, H.; Yang, W.; Noda, T. *Chemical Physics Letters* **2003**, *378*, 299–304.

(43) Zhang, S.; Ahmet, I.; Kim, S. H.; Kasian, O.; Mingers, A. M.; Schnell, P.; Kölbach, M.; Lim, J.; Fischer, A.; Mayrhofer, K. J.; Cherevko, S.; Gault, B.; Van De Krol, R.; Scheu, C. *ACS Applied Energy Materials* **2020**, *3*, 9523–9527.

(44) Lee, D.; Wang, W.; Zhou, C.; Tong, X.; Liu, M.; Galli, G.; Choi, K. S. *Nature Energy* **2021**, *6*, 287–294.

(45) Grimaud, A.; Diaz-Morales, O.; Han, B.; Hong, W. T.; Lee, Y. L.; Giordano, L.; Stoerzinger, K. A.; Koper, M. T.; Shao-Horn, Y. *Nature Chemistry* **2017**, *9*, 457–465.

(46) Zhang, N.; Feng, X.; Rao, D.; Deng, X.; Cai, L.; Qiu, B.; Long, R.; Xiong, Y.; Lu, Y.; Chai, Y. *Nature Communications* **2020**, *11*, 1–11.

(47) Li, Z.; Yang, J.; Chen, Z.; Zheng, C.; Wei, L. Q.; Yan, Y.; Hu, H.; Wu, M.; Hu, Z. *Advanced Functional Materials* **2021**, *31*, 1–8.

(48) Van de Krol, R.; Grätzel, M., et al., *Photoelectrochemical hydrogen production*; New York: Springer: 2012.

3

Operando infrared spectroscopy reveals the dynamic nature of semiconductor-electrolyte interface in multinary metal oxide photoelectrodes

Detailed knowledge about the semiconductor/electrolyte interface in photoelectrochemical (PEC) systems has been lacking because of the inherent difficulty of studying such interfaces, especially during operation. Current understanding of these interfaces are mostly from the extrapolation of ex-situ data or from modelling approaches. Hence, there is a need for operando techniques to study such interfaces to develop a better understanding of PEC systems. Here, we use operando photoelectrochemical attenuated total reflection fourier transform infrared (PEC-ATR-FTIR) spectroscopy to study the metal oxide/electrolyte interface, choosing $BiVO_4$ as a model photoanode. We demonstrate that preferential dissolution of vanadium occurs from the $BiVO_4$/water interface, upon illumination in open circuit conditions, while both bismuth and vanadium dissolution occurs when an anodic potential is applied under illumination. This dynamic dissolution alters the surface Bi:V ratio over time, which subsequently alters the band bending in the space charge region. This further impacts the overall PEC performance of the photoelectrode, at a time scale very relevant for most lab scale studies, and therefore has serious implications on the performance analysis and fundamental studies performed on this and other similar photoelectrodes.

3.1. Introduction

Photoelectrochemical (PEC) water splitting is an attractive technological pathway to produce green hydrogen for low capacity, decentralized applications using only sunlight and water as the reactants.[2] Over the past few decades, metal oxide semiconductors have been extensively investigated for their use in photoelectrochemical systems for solar fuel synthesis and water treatment applications. Metal oxides are interesting candidates for such systems because of their perceived high stability, low cost and satisfy the requirements of band positioning with respect to the water oxidation/reduction potentials.[2, 3] They have been used either as a stand-alone photoelectrode [4, 5] or as a passivation layer to protect smaller bandgap and less stable photoelectrodes [6, 7], and as a result the metal oxide/electrolyte interface is a vitally important aspect in photoelectrochemistry.

Most of the early research in photoelectrochemistry focused on finding metal oxides with a single metal component (referred to as binary metal oxides hereafter), that can satisfy the basic requirements of a photoelectrode. Soon it was apparent that these binary metal oxides are not sufficient due to their intrinsic limitations in light absorption, carrier transport and/or stability.[8] To overcome some of these challenges, more recently, multinary metal oxides like $BiVO_4$, $CuWO_4$, Fe_2TiO_5, $CuBiO_4$ etc. have been extensively investigated, as they offer us the ability to tune the optoelectronic properties of these photoelectrodes by varying the metal composition and defect structure in these multinary metal oxides.[2, 8] Even though these materials have surpassed their binary counterparts in terms of performance and efficiency, they are still massively underperforming when compared to their theoretical efficiency limits. Charge carrier recombination at the semiconductor – electrolyte interface (SEI) have been cited as one of the main factors for this reduced performance.[9] Co-catalyst deposition has demonstrated the ability to partly alleviate this problem by improving the charge transfer kinetics of the holes towards water oxidation.[10, 11] However, even with the addition of co-catalysts, these electrodes have not achieved their true potential. In addition, the use of co-catalysts will bring additional processing steps and costs in the manufacturing of these photoelectrodes and can also induce parasitic light absorption in these materials, making them a less attractive solution.[12]

To tackle this fundamental problem, there is a need to study and better understand the semiconductor-electrolyte interface. Such attempts have been limited because of the practical difficulty of studying such interfaces during photo-electrolysis. Most of the knowledge that we have at present about these interfaces has come indirectly from extrapolation of ex-situ data or are based on modelling approaches. Only a handful of in-situ [13–16] and operando studies [17] have been performed on these systems until now. Operando and in-situ studies of these interfaces are of utmost importance as only such works can reveal the true nature of the SEI. In this work, for the first time, we use operando ATR-FTIR spectroscopy to study the $BiVO_4$/electrolyte interface under PEC conditions. Previous works [17, 18] done with PEC-ATR-FTIR spectroscopy on a hematite photoanode used an Otto configuration of ATR [19], obtained by pressing the photoanode against the internal reflection element (IRE) element with an ultrathin layer

of electrolyte in between. Apart from the obvious compromise of the electrochemical aspects of such a configuration, the spectra was also dominated by the absorption of the bulk water as the evanescent wave had to travel through the bulk water to get to the semi-conductor/electrolyte interface. This meant that only a small window, not dominated by the water absorption can be analysed. Here, in a novel approach, ATR in a Kretschmann configuration [19] is used to study the metal oxide/electrolyte interface under operando conditions. A micro-machined Silicon wafer (~ 500 µm) was used as the IRE to facilitate this. This thin wafer minimized the path length of infrared within the bulk of Silicon and thus minimized the resultant phonon absorption of infrared by the bulk of Silicon.[20] This way, the lower wavenumber limit (LWL) of this IRE element was extended to ~ 600 cm^{-1}, enabling the probing of the finger print region. Hence, an extended range of the infrared spectra of interest (600-4000 cm^{-1}) of the BiVO$_4$/electrolyte interface is revealed under electrochemical and photoelectrochemical conditions.

It is shown that, upon illumination in open circuit conditions, the SEI is modified with time as a result of the dissolution of vanadium from the surface of BiVO$_4$ complexes. This dissolution modifies the space charge region and results in an improved charge separation and thus a better PEC performance because of the heterojunction formed by the vanadium deficient surface BiVO$_4$ and the pristine bulk BiVO$_4$. This concept of improved PEC performance from prolonged illumination under open-circuit conditions is known as "photocharging" in previous literature.[21–24] The time scale of this effect was shown to be in the order of minutes to hours.[21–24] Until now, similar enhancements from photocharging have been demonstrated for BiVO$_4$ [21–24] , CuWO$_4$ [25], Fe$_2$TiO$_5$ [26], Bi$_4$TaO$_8$X [27] and in heavily doped binary metal oxide photoanodes [28, 29], indicating that this could be a common phenomenon in multinary metal oxide photoelectrodes. Hence, BiVO$_4$ is chosen in this work as a model multinary metal oxide photoelectrode, and as such, the findings here can be extended to other commonly used multinary metal oxide photoelectrodes. The time-scale of this dissolution and modification of the interface will have drastic implications on the performance analysis and in many fundamental studies that have been performed on these materials. Our ATR-FTIR spectroscopy data also reveals that most of the (photo-)electrochemical performance improvement techniques in literature for improving the PEC performance of multinary metal oxide photoanodes [30, 31], result in similar surface modification and heterojunction formation with the bulk electrode.

3.2. Materials and methods

Preparation of BiVO$_4$ photoanodes

The bismuth vanadate thin film photoanodes were prepared using a spray pyrolysis technique. Details of the deposition procedure can be found here.[32] Briefly, clean FTO substrates (Hartford Glass co.) were first spray coated with ~ 80 nm SnO$_2$ layer at 425 °C. Subsequently, a ~ 200 nm BiVO$_4$ was coated on top at 450 °C. For the operando infrared spectroscopy, BiVO$_4$ was directly deposited on a clean silicon IRE element (Specialized 1, Irubis GmbH), without the intermediate SnO$_2$ layer. A ~ 20 nm conductive ITO layer

was sputtered onto this silicon IRE element, before the deposition of $BiVO_4$. After the $BiVO_4$ deposition, the samples were annealed in air at 460 °C for 2 hours, at a rate of 5 °C/min. The silicon IRE element was cleaned by sonication in concentrated HCl, followed by multiple sonication steps in ultrapure water.

ITO sputter deposition

A ~ 20 nm ITO layer was deposited by DC magnetron sputtering onto a micro-machined Si ATR element (Specialized 1, Irubis GmbH) using an AJA Orion sputtering system. The thickness was chosen such that the layers are thick enough to have good electron conduction, but thin enough to minimize Drude absorption of the infrared by the conductive ITO layer. Prior to the deposition, the substrate was cleaned by sonication in concentrated hydrochloric acid and followed by washing and sonication in ultrapure water. Further, the surface was cleaned using an argon plasma for 2 minutes at 20 W prior to the ITO deposition. The ITO layer was deposited at a rate of 0.169 Å/sec from an ITO target (ITO 90-10%, 99.99% pure, Testbourne Ltd.) at 15 W, at a base pressure of 3 µbar, with substrate rotation.

Photoelectrochemical testing

Photoelectrochemical measurements were performed using a custom built photoelectrochemical cell, in a three electrode configuration with a saturated Ag/AgCl reference electrode (XR300, Radiometer analytical). A platinum coil was used as the counter electrode. Different electrolytes were used throughout this study and are mentioned specifically in the results and discussion section. Potentials and currents during the experiments were measured and controlled using a VersaSTAT 3 potentiostat. The photoelectrochemical experiments were performed in a nitrogen gas purge at 50 sccm, to remove any dissolved gases and with magnetic stirring to ensure adequate mixing. A Newport Sol3A Class AAA solar simulator was used in the experiments to provide a AM1.5G simulated solar illumination. Back side illumination was used in all the experiments. The photocharging of the $BiVO_4$ photoanodes were performed by prolonged illumination of the photoanodes under open-circuit conditions.

Operando ATR-FTIR spectroscopy

Operando ATR-FTIR measurements were performed in a Bruker Vertex 70 spectrometer equipped with a liquid nitrogen cooled MCT detector and a Veemax-III ATR accessory. The $BiVO_4$ coated Si IRE element was loaded onto a custom built cell, which is then placed on the Veemax III ATR accessory, with a 35° angle of incidence. After loading, the setup was left idle for 30 minutes to purge out moisture and CO_2 before the start of experiments. Electrochemical connections were taken by making an electrical contact with the ITO back contact and a coiled platinum wire was used as the counter electrode. A PINE low profile Ag/AgCl electrode was used as a reference and the potentials were controlled using a BioLogic SP-200 potentiostat. Nitrogen gas was purged through the electrolyte at 50 sccm throughout the experiments. A ThorLabs MP405LP1 LED, equipped with a collimator, was used for illumination during the experiments, at a light intensity

of 6 mW/cm^2. The light intensity was measured using a Newport 1919R handheld power meter equipped with a 918D-UV-OD3R detector. The FTIR spectra was obtained in the absorbance mode, by averaging 512 scans. As such, each spectra presented here is an average of data measured over ~ 80 seconds.

3.3. Results

In the present work, photocharging of BiVO$_4$ was performed in ultrapure water, unless otherwise specified, by prolonged illumination of the sample under open-circuit conditions. Figure 3.1 (a) shows the cyclic voltammogram of BiVO$_4$ photoanodes before and after photocharging in ultrapure water. The voltammogram of BiVO$_4$ photocharged in a borate buffer is also shown in Figure 3.1 (a) for reference. As evident here, the PEC performance of BiVO$_4$ improved multifold, post photocharging, in accordance with previous literature.[21, 22] This improvement was accompanied by a cathodic shift in the open circuit potential (Figure S3.1 (a)) and onset potential of the photocurrent. To study the BiVO$_4$/electrolyte interface under (photo-)electrochemical condition, operando PEC-ATR-FTIR spectroscopy setup was developed and schematic of this setup is shown in Figure 3.1 (b). BiVO$_4$ was directly deposited onto the micromachined Si IRE element, after the deposition of a thin conductive ITO layer as a back contact. This configuration ensured that the evanescent wave first passes through the BiVO$_4$/electrolyte interface, before penetrating into the bulk of the electrolyte. In addition, Silicon wafer IRE facilitated annealing the BiVO$_4$ thin film, post deposition at 460 °C, to ensure its transformation to a monoclinic scheelite structure.

The bulk infrared spectra of BiVO$_4$ is shown in Figure 3.1 (c) and the spectrum of the ITO film can be found in supporting information Figure S3.2. A clean Si IRE element was used as the background and the spectra was obtained by background subtraction in the absorbance mode. Figure 3.1 (c) also includes the spectra of a SiO$_2$ layer on the Si IRE element, which was obtained against a Si background. A thick SiO$_2$ layer is formed on the Si IRE element when subjected to high temperature spray pyrolysis of BiVO$_4$, resulting in a broad feature between 1000 – 1300 cm^{-1}, centered around 1075 cm^{-1}. This region is ascribed to the Si-O-Si asymmetric stretching vibrations in SiO2. [33, 34] To obtain the SiO$_2$ spectra, the Si IRE element was subjected to the high temperature process for the same duration of spray pyrolysis, but without depositing BiVO$_4$ on top. The spectra of BiVO$_4$ after the background subtraction with a SiO$_2$ coated Si IRE element is also shown in Figure 3.1 (c). In monoclinic BiVO$_4$, each V atom is coordinated with four O atoms and each Bi atom is coordinated with eight O atoms. Each dodecahedral BiO$_8$ unit is surrounded by eight tetrahedral VO$_4$ units and as such, each O atom is coordinated to two Bi and one V centre. [35] As a result of the structural distortion in the monoclinic structure, the four fold symmetry is lost, resulting in two different V-O bond lengths and four different Bi-O bond lengths within a monoclinic scheelite structure.[35] Due to this low symmetry, many overlapping peaks appear in the infrared spectra resulting in a very broad feature. As seen in Figure 3.1 (c), the BiVO$_4$ FTIR spectra is represented by a broad feature between 600-900 cm^{-1}, peaked around 682 cm^{-1} and with shoulder

3
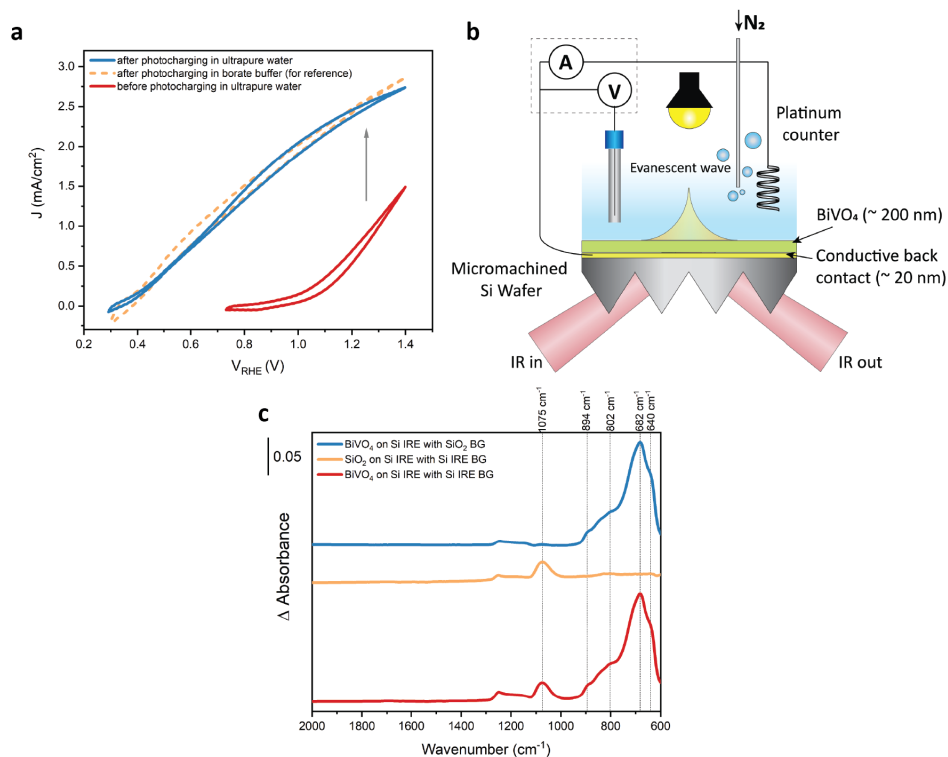
Figure 3.1: (a) Cyclic voltammogram of BiVO$_4$ before and after photocharging in ultrapure water, with the voltammetry performed in a borate buffer electrolyte. The voltammogram of BiVO$_4$ photocharged in a borate buffer is also shown for reference. (b) Schematic of the custom built operando PEC – ATR FTIR cell with a 405 nm LED light source, a saturated Ag/AgCl reference electrode and a platinum counter. (c) Infrared spectra of the reference BiVO$_4$ thin film obtained with different backgrounds. Spectra of SiO$_4$ formed during the BiVO$_4$ deposition process is also shown.

peaks on either side at 640 cm^{-1}, 802 cm^{-1}, 842 cm^{-1} and 892 cm^{-1}. Although there is a general consensus in literature that the infrared spectra of monoclinic BiVO$_4$ has a broad feature in this region, the actual spectral shape and peak assignments vary across different works. [36–40] The discrepancies might stem from the differences in the synthesis technique used to prepare the monoclinic BiVO$_4$, difference in post treatment procedures and/or from the difference in the characteristics of the sample used for the analysis (powder/thin film). All of these parameters, can individually or collectively affect the vibrational frequencies of the resultant structure. For example, it was demonstrated that the symmetric and asymmetric stretching vibrations of the VO$_4^{3-}$ units undergoes a shift to lower wavenumbers with a higher annealing temperature. [40] In another instance, it was shown that monoclinic BiVO$_4$ with different dominant facets can have slightly different vibrational infrared spectra.[36] The broad peaks at 682 cm^{-1} and 802 cm^{-1} in Figure 3.1 (c) are tentatively assigned to the asymmetric stretching vibrations of the VO$_4^{3-}$ unit, whereas the peak at 894 cm^{-1} is assigned to the symmetric stretching vibrations of this

VO_4^{3-} unit. The shoulder peak at 640 cm^{-1} is assigned to the Bi-O symmetric stretching vibrations. Spectra of water was also acquired using this ATR-FTIR setup and is shown in Figure S3.2 (b). The distinct spectra for borate ions and monobasic phosphate ions in water, acquired with water as the background is also shown in Figure S3.2.
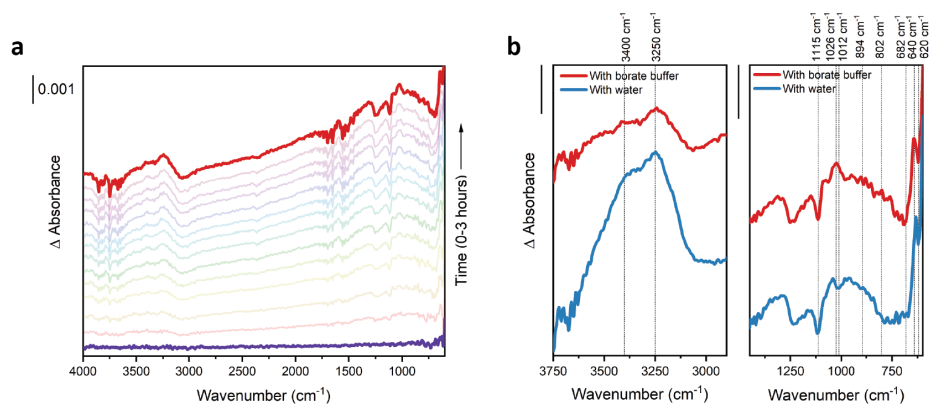
Figure 3.2: (a) Infrared spectra of the BiVO$_4$/electrolyte interface acquired over the course of photocharging in the case of a borate buffer electrolyte. (b) Comparison of relevant regions in the infrared spectra, after 3 hours of photocharging in borate buffer electrolyte and in ultrapure water. The scale bar is 0.001 units.

Next, the BiVO$_4$ was subjected to the photocharging treatment by illuminating the substrate in a borate buffer electrolyte (pH 10), under open circuit conditions for 3 hours in the custom built operando PEC - ATR FTIR cell. Cyclic voltammetry of this BiVO$_4$, before and after the photocharging treatment, is shown in Figure S3.3. The improvement in PEC performance here is very similar to that in photoelectrochemical cell, indicating the successful reproduction of the photocharging effect in the operando cell. The change in the infrared spectra with time, acquired during the course of photocharging, in the case of borate buffer electrolyte is shown in Figure 3.2 (a). The spectra was acquired after background subtraction, with an illuminated BiVO$_4$ sample under open circuit conditions at t = 0 chosen as the background. This ensured that the changes in the infrared spectra due to any sub-minute electronic changes in BiVO$_4$ upon illumination were subtracted out from the resultant spectra and that the changes in the infrared spectra shown in Figure 3.2 (a) are solely due to the photocharging process. Similarly, photocharging was also performed in ultrapure water and with a phosphate buffer. The changes in the infrared spectra and open circuit potential in time is shown in Figure S3.4. In addition, the spectral change of the ITO coated Si IRE element (i.e., without BiVO$_4$) in ultrapure water under illumination, BiVO$_4$ sample illuminated in air (i.e., without any electrolyte/water) and BiVO$_4$ sample left in the dark conditions in water were also obtained and are shown in Figure S3.5.

In Figure 3.2 (a), many changes in the infrared spectra are visible over the course of photocharging. First, the spectra exhibits a positive tilt with time during photocharging. A rough baseline for the borate spectra after photocharging for 3 hours is shown in Fig-

ure S3.4 (d), showing the tilt of the spectra with photocharging. The positive tilt in the spectra is attributed to the Drude absorption of the infrared by the free electrons, which increases at lower wavenumbers. Therefore, an increase in the slope of the spectra with time suggests an increase in the free electron concentration in $BiVO_4$ with photocharging.[41] In fact, similar conclusions were also obtained from electrochemical impedance spectroscopy of photocharged $BiVO_4$. [22, 23] In contrast, the $BiVO_4$ sample illuminated in air, i.e. with no electrolyte or water, and the non-illuminated $BiVO_4$ samples (Figure S3.5), do not attain a similar tilt, suggesting that the electrode/water interface and illumination is important here. This also coincides with the cathodic shift in the open circuit potential with photocharging, as shown in Figure S3.4 (b).

In Figure 3.2 (b), the spectra of $BiVO_4$ after 3 hours of photocharging in borate buffer electrolyte and ultrapure water are plotted together for comparison. Common spectral changes that were observed include a broad positive trending peak at 3250 and 3400 cm^{-1}, which is the region for OH stretching vibrations within the infrared spectra. A positive trending peak in this region suggests an increase in the concentration of OH/water species either at or close to the surface with increased photocharging. It should be noted that the increase in intensity of the OH stretching vibrations only are observed for illuminated samples. A $BiVO_4$ sample illuminated in air also showed a similar increase in intensity of the OH stretching vibrations with time, possibly as a result of the oxidation of moisture in the air by the photogenerated holes to form absorbed OH species at the $BiVO_4$ surface. The other common change is in the region of Si-O-Si and Si-Si/Si-H stretching vibrations. Here, a negative trending peak at 1115 cm^{-1} with a broad shoulder to its left is visible. Such negative trending peaks are seen in the case of SiO_2 when there is a breakage of the Si-O-Si bonds, resulting in Si-O- dangling bonds which has a lower vibrational frequency. [34] A negative going peak in this case, implies that more Si-O-Si bonds are broken with increasing illumination time. The subsequently formed Si-O- bond is clearly visible with a positive trending peak at 1088 cm^{-1} in Figure S3.5 (b). The origin of the negative going peak at 620 cm^{-1} is more ambiguous. Peaks at 620 cm^{-1} have been reported for weak near surface Si-Si stretching vibrations in amorphous silicon substrates. A negative trending peak at 620 cm^{-1} is an indication of a change in the Si-Si stretching vibration with illumination, possibly suggesting the breakage of weak near surface Si-Si bonds in the silicon based IRE element.[42] Alternatively, this negative trending peak at 620 cm^{-1} could also be attributed to the wagging mode of Si-H bonds at the surface of the Si IRE element. Si-H bonds could be formed at the surface during the acid cleaning step of the Si IRE element and is now removed during the light treatment. These changes are also visible when the sample is illuminated in air, as seen in Figure S3.5 (b). More research needs to be performed to reveal the exact identity of this peak at 620 cm^{-1}. Additionally, a small change in the background moisture and CO_2 content with time is also visible within the photocharging spectra due to the unusually long-time scale of the measurements.

Both spectra in Figure 3.2 (b) contain a negative trending peak at 682 cm^{-1}, accompanied by a broad shoulder peak(s) to its left, which is also going down. The shape of this shoulder peak is slightly different in the case of borate and water. The peaks at 682 cm^{-1}

and 802 cm^{-1} were assigned to V-O asymmetric stretching vibrations, whereas the peak at 894 cm^{-1} was assigned to V-O symmetric stretching vibrations. It should also be noted that the intensity of the peak at 640 cm^{-1}, which was assigned to Bi-O symmetric stretching vibrations, is stable or only changes very slightly during photocharging. A decrease in the intensity of the V-O stretching vibration peaks with photocharging indicates a decrease in the concentration of vanadium from the BiVO$_4$ surface. It should be noted that this decrease in the intensity of the V-O stretching vibrations was not observed when BiVO$_4$ was illuminated in air. These data indicate that this decrease in the vanadium concentration is an interfacial process and that it only happens at the BiVO$_4$/water interface. The vanadium species is selectively removed from the surface during photocharging, leaving behind a bismuth rich surface. X-ray Photoelectron Spectroscopy (XPS) data of photocharged BiVO$_4$, from previous reports [22, 24], also indicated a similar decrease in the surface vanadium concentration post photocharging which is in agreement with the observations from the infrared spectra of photocharged BiVO$_4$ in this work.

The other main difference in the spectra in Figure 3.2 (b) of BiVO$_4$ photocharged in a borate buffer, compared to a sample photocharged in water, is in the region between 800 – 1050 cm^{-1}. In the case of borate, a positive trending peak at 1026 cm^{-1} is visible. This peak is not visible in the case of water. Instead, a negative trending peak at 1012 cm^{-1} is visible in the case of sample photocharged in water, which is not seen in the case of borate buffer electrolyte. The peak at 1012 cm^{-1} is attributed to V=O stretching vibrations.[43–45] BiVO$_4$ can sometimes have V=O bonds at the surface due to the abrupt termination of the surface. The negative trending peak at this position again suggests the removal of this vanadium species from the surface during photocharging. In the case of the borate buffer electrolyte, the positive trending peak at 1026 cm^{-1} (and a broad peak underneath it) is assigned to an increase in the concentration of the borate/boric acid species in the inner sphere with photocharging. [46] A similar increase in the concentration of the electrolyte anionic species at the BiVO$_4$ surface with illumination was also observed with in-situ hard X-ray XPS. [13] The broad positive going peak of borate partially overlaps with the negative going shoulder peak of the V-O stretching vibrations, explaining the difference in the shape of this shoulder peak between borate and water. The negative trending peak at 1012 cm^{-1} might also be present in the case of photocharging in borate buffer electrolyte but it is masked by the broad positive going borate peaks and hence is not visible.

It has been shown in earlier reports that the photocharging effect was reversible in the dark. [21] This phenomenon occurred when the sample was left in open circuit conditions in the dark for a prolonged time after photocharging, resulting in the enhancement effect from photocharging to diminish. This is observed by an inferior current-voltage response from cyclic voltammetry after the decay, when compared to a photocharged sample, as shown in Figure S3.6 (a). The change in the infrared spectra during this dark decay process was also studied over time and the spectra is shown in Figure 3.3 (a). To make the identification easier, the spectra after the 2 hour dark decay process is compared with a sample photocharged for the same duration and both spectra are shown in Figure 3.3 (b). As seen with the photocharging process, the decay process

also shows an increase in OH$^-$/water concentration near/at the surface with time. Additionally, the decreasing peak of Si-O-Si bond breakage at 1115 cm^{-1} that was present in the case of the photocharged sample, is not visible in the case of the decayed sample. Instead, the dark sample has a decreasing peak at a slightly lower vibrational frequency, which was assigned to the stretching vibrations of Si-O$^-$ species. Si-O$^-$ species were formed from the bond breakage of the Si-O-Si under illumination, and the decreasing peak at this position for the decayed sample suggests the passivation or re-formation of these Si-O-Si bonds in the dark.

3
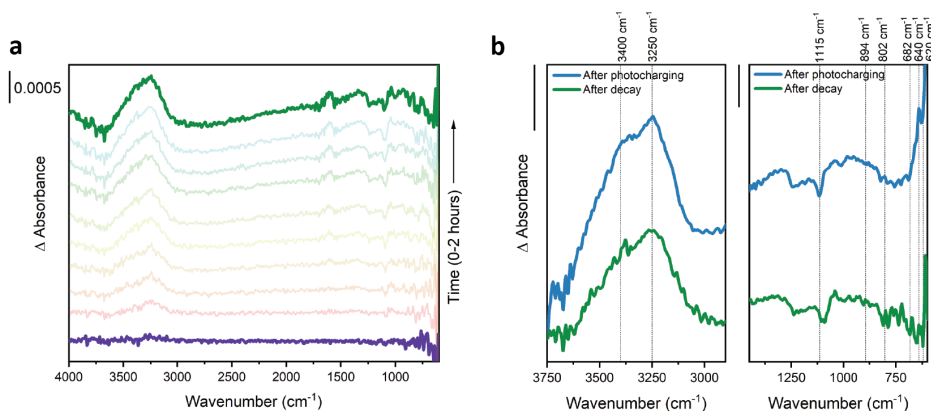
Figure 3.3: (a) Infrared spectra of the BiVO$_4$/electrolyte interface acquired over the course of the decay process in the dark in ultrapure water. (b) Comparison of the infrared spectra of BiVO$_4$ after 2 hours of photocharging and decay in ultrapure water. The decay spectra was scaled by a factor of 2. The scale bar is 0.001 units.

The main distinction between the infrared spectra of photocharged sample and the decayed sample in Figure 3.3 (b) is in the region between 600 – 900 cm^{-1}. As discussed before, during photocharging, the peaks ascribed to the V-O stretching vibrations decreased in intensity, while the peaks ascribed to the Bi-O stretching vibration at 640 cm^{-1} remained intact. In contrast, during the decay of the photocharging effect in the dark, a decreasing peak associated with the Bi-O stretching vibration was observed. On the other hand, the region of V-O stretching vibration is fairly intact during this decay process. This suggests that the bismuth rich surface formed during photocharging is slowly removed during the decay in the dark, further changing the Bi:V ratio at the BiVO$_4$ surface. The other main distinction is that the infrared spectra during the decay process does not tilt like the spectra in the case of photocharging. This is clear when the spectra after two hours of decay is compared to the spectra after two hours of photocharging in ultrapure water, as shown in Figure S3.6 (b). Very small changes in the carrier concentration might occur in BiVO$_4$ even during decay process because of the removal of bismuth ions in the dark (removal process could inject some electrons into the bulk). These small changes will have an effect on the slope of the spectra, but as shown in Figure S3.6 (b), they are negligible when compared to the changes under illumination.
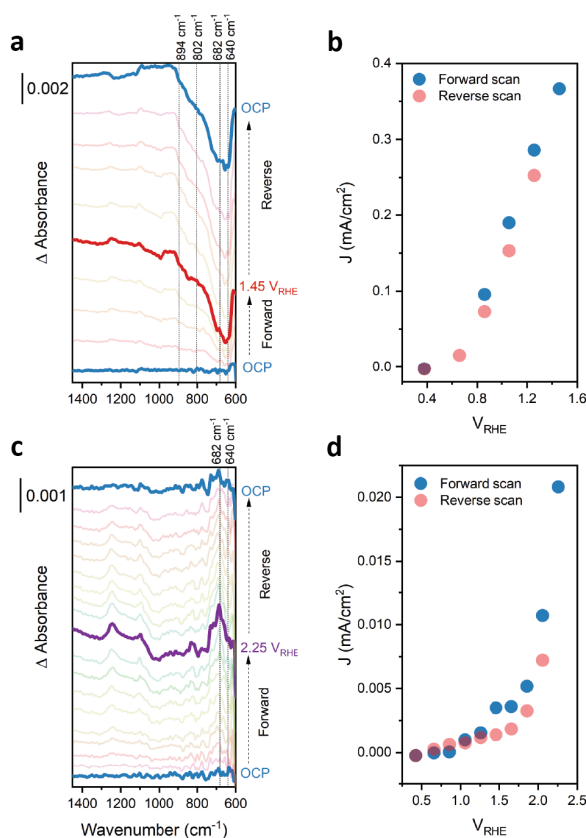
Figure 3.4: (a) Infrared spectra of the $BiVO_4$/electrolyte interface acquired at different anodic potentials during a potential step scan under illumination. (b) Current density versus applied potential plot when the potential was stepped under illumination. (c) Infrared spectra of the $BiVO_4$/electrolyte interface acquired at different potentials during a potential step scan in the dark. (d) Current density versus applied potential plot when the potential was stepped under dark conditions.

Further experiments were designed to mimic the photocharging of $BiVO_4$ in the dark by applying an anodic potential for a prolonged time. This was done to see if the PEC enhancement from photocharging can be replicated by providing an external applied voltage which is equivalent or higher than the photovoltage obtained from illumination. Although applying anodic potentials for prolonged times did not lead to enhancement in the PEC performance (Figure S3.7), further insights can be obtained on the dissolution of the photoanodes and its effect on infrared spectrum. Therefore, the changes in the infrared spectra of the $BiVO_4$/electrolyte interface, when an anodic potential was applied under illuminated and dark conditions in a phosphate buffer electrolyte, were also studied in this work. In Figure 3.4 (a), the development of infrared spectra during a potential step scan of $BiVO_4$ under illumination is shown. Here, the potential was systematically changed (step size of 0.2 V) in ~ 4 minute intervals from open circuit conditions to 1.45 V_{RHE}, and then reversing the potential back to open circuit potential conditions in a

3

similar stepwise manner, with the infrared spectra being recorded at each potential step. Initial open circuit conditions were chosen as the background, for overall spectral background subtraction. The recorded current transient at the end of each potential step is plotted against the applied potential in Figure 3.4 (b). Similarly, the infrared spectra was also recorded during a potential step scan in the dark conditions and is shown in Figure 3.4 (c). Here the potential was stepped evenly from open circuit conditions to 2.25 V_{RHE} and back to open circuit conditions and its current-voltage response is plotted in Figure 3.4 (d). As discussed earlier, the region between 600 – 900 cm^{-1} in the infrared spectra is dominated by the absorption from the molecular vibrations in $BiVO_4$. It is observed that the infrared spectra in Figure 3.4 (a), when the potential is ramped up and cycled back to open circuit conditions, is not completely reversible. Here, peaks at 640 cm^{-1} , 682 cm^{-1}, 802 cm^{-1} and 894 cm^{-1}, pertaining to Bi-O and V-O stretching vibrations, are observed to increase in intensity in the negative direction with applied potential under illumination. It is interesting to note that, both V-O and Bi-O stretching vibrations are going down in the case when a potential is applied in the presence of illumination, implying that both bismuth and vanadium are removed from the surface. In contrast, during photocharging, only the vanadium species were removed from the surface during the course of prolonged illumination. The larger intensity of the negative going peaks suggests that the rate of this removal is also higher when a potential is applied in the presence of illumination. On the other hand, in case of potential cycling in the dark in Figure 3.4 (c), the region between 600 – 900 cm^{-1} seems to be completely reversible, implying that no bismuth or vanadium is removed from the surface during potential cycling in the dark. There are some potential induced features that are visible within the infrared spectra in the dark between 600 – 900 cm^{-1}, but these features disappear when the potential is cycled back to open circuit potential. These potential induced features are attributed to potential induced alterations of the molecular vibrations of $BiVO_4$ and/or to the vibrations from the surface absorbed species, e.g., water oxidation intermediates, formed as a result of the applied anodic potential. Infrared signatures for different water oxidation intermediates on the $BiVO_4$ surface might also be expected when the potential is applied under illumination. The wavenumbers of these adsorbed intermediates are expected to be in the region of 700 – 950 cm^{-1}. [17] However, the strong overlap with the $BiVO_4$ bulk adsorption spectra and negative trending peaks because of the cation dissolution, in this region, might overshadow the wavenumbers of these adsorbed intermediates which typically have low intensities. The full range spectra, in the case of applied potential under dark and illumination, is shown in Figure S3.8. The spectra in Figure 3.4 (a) and (c) and Figure S3.8, also include some potential induced changes in the OH stretching vibrations and Si-O-Si stretching vibrations are also visible. The P-O stretching vibrations of the phosphate buffer ions have a strong overlap with the Si-O-Si stretching vibrations and hence it is difficult to isolate and study any potential induced changes of the buffer ions.

3.4. Discussion

Prior research into the photocharging of $BiVO_4$ had indicated that the enhancement from photocharging is both a bulk and a surface effect. [21, 22, 24] In-situ EXAFS and X-ray diffraction data suggested that the bulk structure of $BiVO_4$ was not effected with the photocharging treatment [22, 24], while intensity modulated photocurrent spectroscopy (IMPS) on photocharged $BiVO_4$ suggested that the bulk charge separation and surface charge transfer improved upon photocharging. [23] All previous works on photocharging had been performed in the presence of a buffer electrolyte. Our recent work with grazing incidence X-ray Raman Scattering had revealed that the space charge region was modified with the photocharging treatment and it resulted in an increase in the band bending post photocharging. [24] With the data available at that time, it was speculated that this was a result of the chemisorption of the buffer anions on the $BiVO_4$ surface and the resultant formation of a heterojunction close to the surface. In the current work, photocharging of $BiVO_4$ was performed in ultrapure water (i.e., no buffer anions present in the electrolyte), suggesting that the chemisorption of anions is not the primary reason for the photocharging process, contrary to our earlier speculations. These anions might still be playing a role in the photocharging process, which will be discussed later.
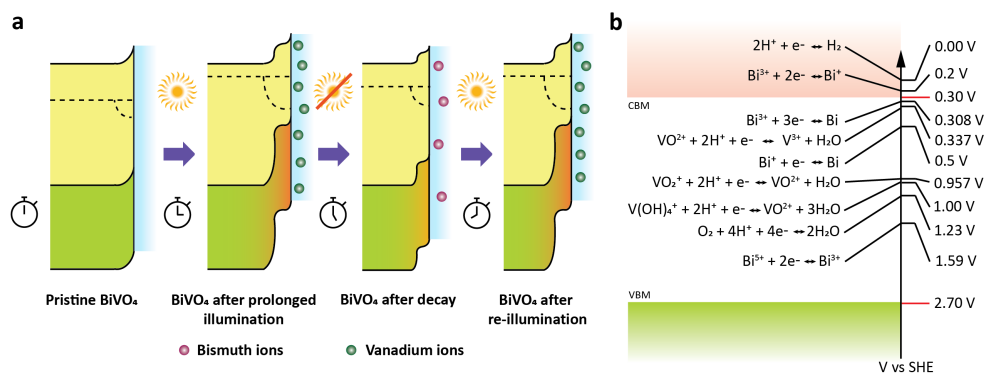
Figure 3.5: Figure 5 : (a) Schematic of the dynamic nature of the metal oxide/electrolyte interface when subjected to illumination and dark cycle for a prolonged time, under open circuit conditions. (b) Data of relevant standard reduction potentials plotted in the SHE scale along with the Conduction Band Minimum (CBM) and Valence Band Maximum (VBM) positions of $BiVO_4$. Data was aggregated from different sources. [47, 48]

Operando infrared spectroscopy of the $BiVO_4$/water interface revealed that when an anodic potential is applied under illumination, both surface bismuth and vanadium ions are removed from the $BiVO_4$ surface. Similar observations were also made by Zhang et al. [47], where they used operando inductively coupled plasma mass spectroscopy (ICPMS) to study the photostability of $BiVO_4$. The rate of dissolution of bismuth and vanadium were also observed to heavily depend on the nature of the co-ions in the electrolyte. Similarly, several works in literature investigating the long term PEC stability of $BiVO_4$ in similar conditions have observed a gradual increase in the photocurrent over the first few hours ($\sim 20 - 30$ hours) of the stability tests, but have failed to unambiguously ex-

plain this behaviour. [10, 48] The infrared spectroscopy data in this work, when $BiVO_4$ is illuminated under open circuit conditions, only vanadium dissolution is observed from the $BiVO_4$ surface. When an anodic potential is applied in the dark conditions in a phosphate buffer electrolyte, the infrared spectra was completely reversible and no bismuth or vanadium dissolution was observed. This result also agrees with the work from Zhang et al. [47], where they observed negligible dissolution of bismuth or vanadium when a potential was applied in the dark.

It should be noted from the above observations that the PEC performance enhancement with illumination (with or without applied potential) is always accompanied by the dissolution of bismuth and/or vanadium species. In contrast, when an anodic potential is applied in the dark conditions, no PEC performance enhancement or dissolution is observed. This indicates the dissolution of vanadium and/or bismuth is critical to have any observable PEC performance enhancement. The removal of vanadium and/or bismuth at different rates from the surface of $BiVO_4$, as in the case of photocharging or when an anodic potential is applied under illumination, will alter the Bi:V ratio at the surface over time. Typically, it is observed that the dissolution rates of bismuth is much lower than that of vanadium. [22, 47] This change in surface the Bi:V ratio over time will also explain the change in the open circuit potential over time that is seen during photocharging. Open circuit potential, also known as corrosion potential, is a useful tool in corrosion chemistry to track the changes in the surface composition due to dissolution or formation of oxide/hydroxide. [49, 50] Figure S3.9 shows the temporal evolution of the open circuit potential and the change in the infrared absorbance at 682 cm^{-1} with time. As evident here, the change in the open circuit potential with time closely follows the change in the infrared absorbance, confirming that they are directly related. The cathodic shift in the open circuit potential during photocharging is thus also an indication of the change in the surface composition of $BiVO_4$.

The preferential removal of vanadium from the surface upon illumination will result in a bismuth dominated surface on top of the pristine bulk $BiVO_4$. Gao et al. studied photo-polarized $BiVO_4$ under a Transmission Electron Microscope (TEM) and observed the development of a thin evenly distributed amorphous layer at the surface of $BiVO_4$, 3 nm thick, after the prolonged photo-polarization. [48] However, the exact composition of this layer was not revealed. XPS data from previous works suggested an increase in the concentration of bismuth at the $BiVO_4$ surface post photocharging.[22, 24] The infrared data from the current work also indicates that surface vanadium is preferentially removed from the surface of $BiVO_4$ during photocharging. Therefore, it can be conclusively suggested that this amorphous layer is a result of the preferential vanadium dissolution upon illumination and thus leaves a bismuth rich surface to form the SEI. A surface layer formation on $BiVO_4$ surface by the chemisorption of anions from the electrolyte, in conditions akin to photocharging, was revealed using in-situ hard X-ray XPS by Favaro et al.[13] The infrared spectra in this work also indicated an increase in the concentration of anionic OH$^-$ and borate stretching vibrations with the removal of vanadium. These ions are possibly substituting the vacancies created by the removal of vanadium species, to maintain the charge balance. Therefore, the photocharging pro-

cess can be considered as a sequential process where vanadium dissolution is followed by hydroxyl or anion uptake at the photoanode surface.

Lee et al. recently reported the effect of surface composition on the PEC properties of $BiVO_4$. [51] Their work suggested that a "bismuth rich" bismuth vanadate will push the band edge positions towards the vacuum level. Such a shift in the band positions will result in a heterojunction between this bismuth rich surface and the pristine bulk $BiVO_4$. This resultant heterojunction will increase the band bending within the space charge region and thereby improve the charge separation of photo-generated charge carriers close to the SEI. Improved PEC performance of a bismuth oxide coated bismuth vanadate photoelectrode was demonstrated by Ye et al. [52], and the performance improvement was attributed to electronic nature of the $Bi_2O_3/BiVO_4$ heterojunction. The improved charge separation within this heterojunction can also be responsible for the improved PEC performance observed after photocharging. Figure 3.5 (a) summarizes this whole process from the formation of the heterojunction to the improved PEC performance. When pristine $BiVO_4$ is illuminated for a prolonged time, vanadium dissolution from the surface of $BiVO_4$ occurs, leaving behind a bismuth rich surface. This bismuth rich surface has band positions closer to the vacuum level and thus results in a heterojunction between the bismuth rich surface and pristine bulk $BiVO_4$. It should be noted that the exact composition of this surface layer is not clear yet. This layer can be a complex mix of BiO_x, $BiVO_4$ with a bismuth rich surface along with a bismuth borate layer (in the presence of a borate buffer). All these layers have the tendency to push the band positions at the surface closer to the vacuum level and thus creating a heterojunction and improving the band bending in the space charge region. When the photocharged $BiVO_4$ is further subjected to the decay process in the dark, slow bismuth dissolution occurs, reducing the band bending within this heterojunction. On re-exposure to prolonged illumination, the cycle repeats. In essence, any surface treatment technique that alters the surface Bi:V ratio of $BiVO_4$, or any multinary metal oxide, might produce a similar PEC performance enhancement. It has been previously reported in literature that applying a cathodic potential in the dark to $BiVO_4$ for a short duration significantly improved its PEC performance. [30] It was suggested here that the enhancement is a result of the creation of "oxygen vacancies" as a result of the reduction process. We also looked into this process by applying a potential cathodic with respect to the open circuit potential in the dark and recording the infrared spectra. As shown in Figure S3.10, the surface Bi:V ratio can also be altered by applying a cathodic potential in the dark for a short duration. This will also result in a similar heterojunction formation and provide similar enhancements as in the case of photocharging.

Information regarding the exact mechanism behind the corrosion of $BiVO_4$ is lacking in literature. Different possibilities have been suggested for this, including oxidation of Bi^{3+} to Bi^{5+} and oxidation of lattice O^{2-} to O^- at the $BiVO_4$ surface by the photogenerated holes. [53] These oxidation processes can destabilize the lattice and induce corrosion of bismuth and/or vanadium. V^{5+} in $BiVO_4$ is already at its highest valency and thus cannot be oxidized further. However, V^{5+} at the surface can be reduced to V^{4+}/V^{3+} in the presence of water/protons by photogenerated electrons at the surface of $BiVO_4$. All

these alternatives are thermodynamically possible, as summarized in Figure 3.5 (b). The thermodynamic equilibrium data of lattice oxygen oxidation process in $BiVO_4$ was not available. From the infrared spectroscopy data during photocharging, a decrease in the V-O stretching vibration was observed while the Bi-O stretching vibrations remained intact. This would suggest that the corrosion process is initiated either by the oxidation of lattice O or by reduction of V^{5+} at the surface of $BiVO_4$ and subsequent dissolution of vanadium. In-situ hard X-ray XPS data on $BiVO_4$ in similar photocharging conditions revealed that the oxidation state of bismuth remained unchanged at +3 upon illumination. [13] The O1s XPS data from their work and other works [22, 24] however showed a shoulder peak at 531.5 eV, which was attributed to oxygen in surface absorbed species, but could also be a result of the formation of O⁻ species at the surface. [54] When an anodic potential is applied under illumination, intensity of both V-O and Bi-O stretching vibrations decreased. With the application of an anodic potential in addition to the illumination, there is potentially more driving force for the 2 electron oxidation of Bi^{3+}, inducing bismuth dissolution along with vanadium as observed in this work. The oxidation of surface bismuth and oxygen is very slow, when an anodic potential is applied in the dark conditions, owing to the low carrier concentrations in the dark. This explains why no bismuth or vanadium dissolution was observed when the potential was cycled in the dark conditions.

3.5. Conclusions

An operando PEC-ATR-FTIR spectroscopy setup was developed and used to study the $BiVO_4$/electrolyte interface during water electrolysis. Operando measurements suggests that, upon illumination in open circuit conditions, preferential dissolution of vanadium occurs from the $BiVO_4$ surface, which indirectly enhances the PEC performance of the photoanode. In contrast, when an anodic potential is applied under illuminated conditions, dissolution of both bismuth and vanadium was observed. Remarkably, it was noted that cation dissolution from $BiVO_4$ is almost always accompanied by improved PEC performance. Our experiments indicate that the difference in the dissolution rates of vanadium and/or bismuth under illumination alters the surface Bi:V ratio, and results in a bismuth rich surface on top of the pristine bulk $BiVO_4$. This is considered to create a heterojunction between the bismuth rich surface and the pristine bulk $BiVO_4$, which significantly improves band bending near the interface. We believe that the improvement in band bending is directly responsible for improved PEC performance from the photocharging treatment. The slow dissolution rates of the cations from $BiVO_4$ implies that the semiconductor/electrolyte interface is slowly modified over time and hence this interface is very dynamic. Our results also suggest that the change in the open circuit potential over time, rather than the photocurrent, is a better indicator of the stability of the photoanode material or of the semiconductor/electrolyte interface.

$BiVO_4$ was used as a model multinary photoanode in this study, however, similar PEC performance enhancements from photocharging have been reported for other multinary metal oxides like $CuWO_4$, Fe_2TiO_5 and in heavily doped metal oxide photoelec-

trodes [25–28] suggesting that this might be a very common phenomenon in different multinary metal oxide photoelectrodes. The time scale of this dissolution (minutes to hours) implies that this effect is very relevant to a lot of lab scale studies and fundamental research performed on these materials, and as such, should be accounted for.

3

3.6. Supplementary information
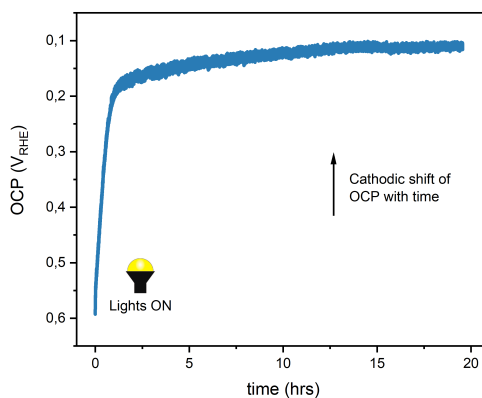
Supplementary Figure S3.1: Change in the open circuit potential with time during photocharging of BiVO$_4$ in ultrapure water.

Figure 3.1 (a) shows the absorption spectra of the 20 nm conductive ITO thin film deposited onto the Si IRE element. A Si IRE element in the same conditions was chosen as the background. The increasing absorption with lower wavenumbers here is a result of the Drude absorption of the infrared by the free carriers in the ITO layer. In Drude absorption, the absorption coefficient is inversely proportional to the square of the wavenumber, resulting in the quadratic shape of the spectra in Figure 3.1 (a). The downward going peak at ~ 1100 cm^{-1} and at 613 cm^{-1}, is a result of the difference in absorption by the Si-O-Si stretching vibrations and Si-Si stretching vibrations respectively, between the ITO deposited sample and the background Si IRE element. Some Si/SiO$_2$ from the surface is removed during the argon plasma cleaning of the Si IRE element, before the ITO layer deposition. Figure 3.1 (b) shows the spectra of water acquired with this operando cell. The penetration depth of the evanescent wave in the current configuration of the PEC ATR-FTIR cell is about ~ 700 nm into the electrolyte from the electrode/electrolyte interface, with the sensing capability decreasing exponentially from the surface. This implies that the infrared spectra will be dominated by absorption of species close to/at the surface compared to the bulk absorption. In Figure 3.1 (b), the broad peak between 2750 cm^{-1} and 3700 cm^{-1} are due to the overlaid symmetric and asymmetric stretching vibrations of water, whereas the peak at 1640 cm^{-1} is due to the bending vibrations of water. The increasing absorption feature below 920 cm^{-1} are a result of the absorption of infrared by the libration modes of water and the downward going peak at 613 cm^{-1} is again due to the difference in Si-Si stretching vibrations between the spectra and the background. The combination mode of the librations and the bending mode is also visible around 2110 cm^{-1} in Figure 3.1 (b). The upward going peak at 1248 cm^{-1} and the downward going peak at 1100 cm^{-1} is result of the change in the Si-O stretching vibrations at the SiO$_2$/water interface, upon the addition of water.
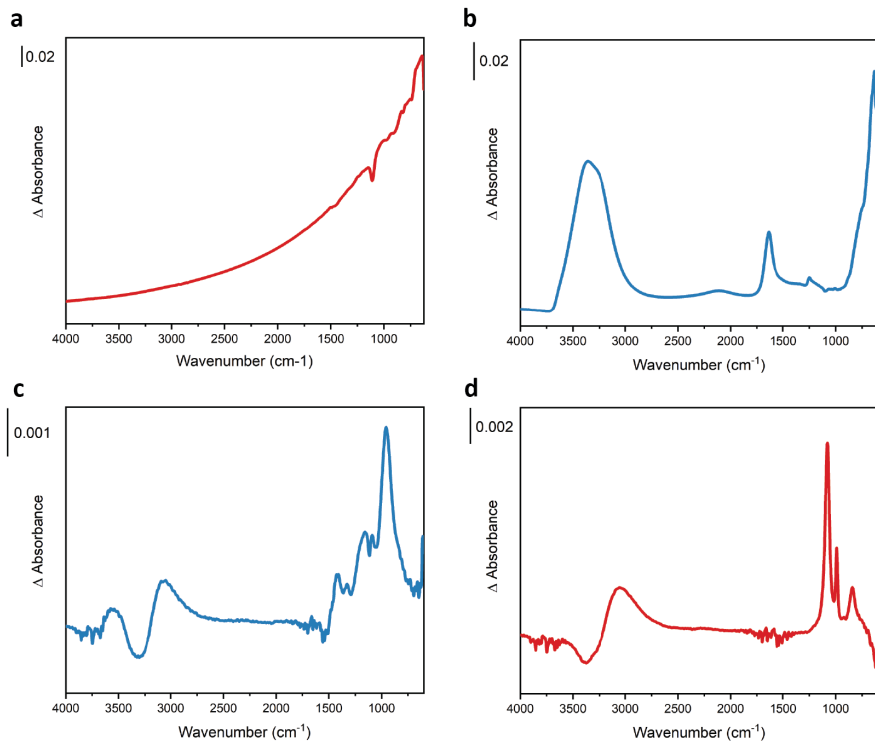
Supplementary Figure S3.2: (a) Spectra of ITO acquired with a clean Si IRE as the background in the absorbance mode (b) Spectra of water acquired with a clean Si IRE in air as the background (c) Spectra of borate buffer electrolyte (pH 10) acquired with ultrapure water as the background in the ATR mode (d) Spectra of phosphate buffer electrolyte (K_2HPO_4, pH 9.1), acquired with ultrapure water as the background in the ATR mode
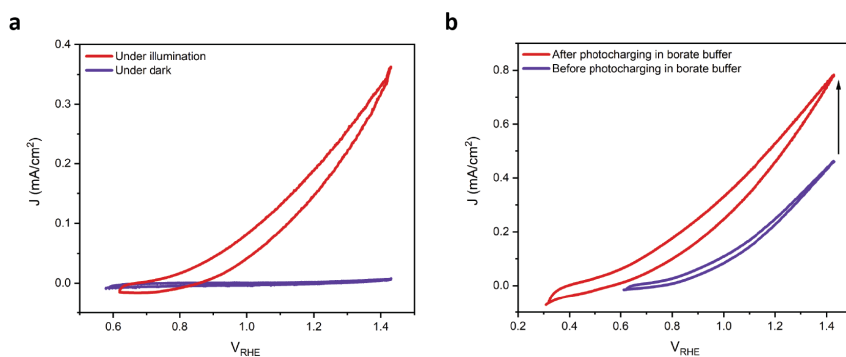
Supplementary Figure S3.3: (a) Cyclic voltammetry of the $BiVO_4$ sample in the custom built PEC- ATR-FTIR cell in dark and light conditions (b) Cyclic voltammetry of the $BiVO_4$ sample before and after photocharging in the custom built PEC-ATR-FTIR cell
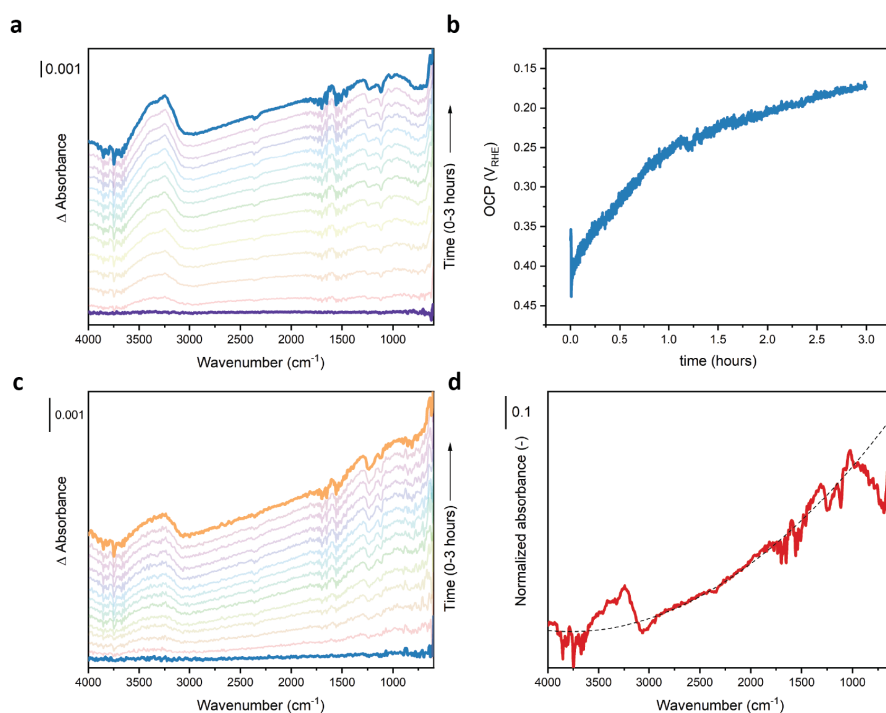
Supplementary Figure S3.4: (a) Infrared spectra of the BiVO$_4$/electrolyte interface acquired over the course of photocharging in the case of a ultrapure water (b) Change in the open circuit potential versus time during this photocharging treatment in ultrapure water (c) Infrared spectra of the BiVO$_4$/electrolyte interface acquired over the course of photocharging in the case of a phosphate buffer electrolyte (d) Rough quadratic fit to show the tilt in the spectra of the photocharged samples with time.

a

b

c

d
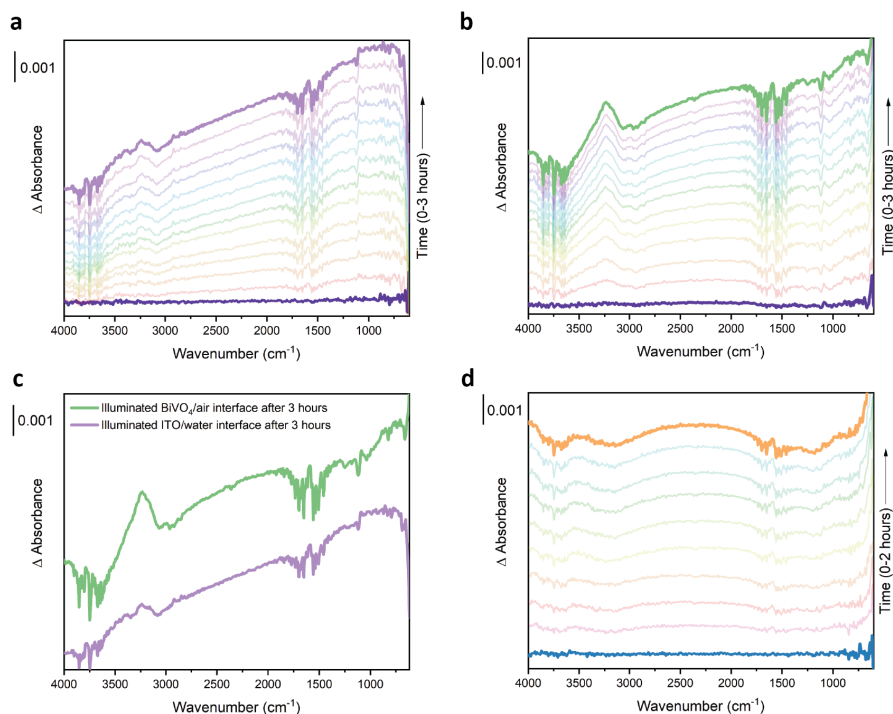
Supplementary Figure S3.5: (a) Infrared spectra of the ITO/water interface acquired over the course of prolonged illumination (b) Infrared spectra of the $BiVO_4$/air interface acquired over the course of prolonged illumination (c) Comparison of the ITO/water and $BiVO_4$/air spectra after 3 hour illumination (d) Infrared spectra of the $BiVO_4$/water interface acquired for samples left in the dark conditions.
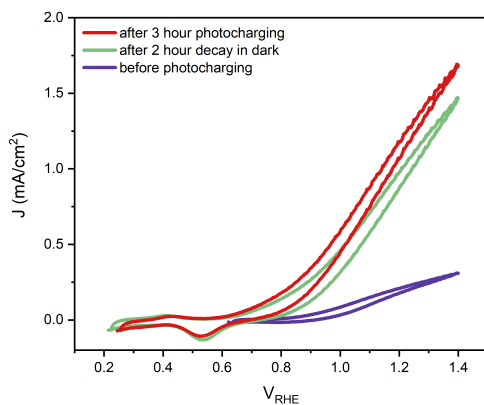
Supplementary Figure S3.6: (a) Cyclic voltammetry of the pristine, photocharged and decayed $BiVO_4$ samples (b) Infrared spectra of $BiVO_4$ after 2 hour photocharging and 2 hour decay in ultrapure water.

3
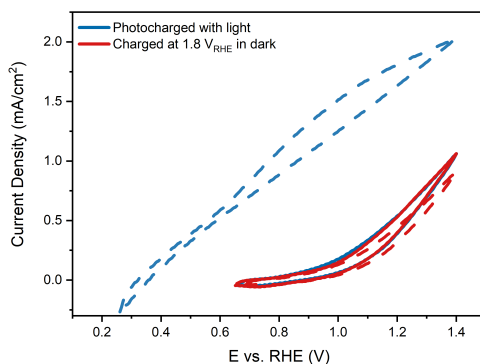
Supplementary Figure S3.7: Cyclic voltammetry of the BiVO$_4$ sample treated with an anodic potential in the dark for a prolonged time. Cyclic voltammetry of a photocharged BiVO$_4$ sample is shown for reference. Solid lines represent voltammetries before the treatment and dotted line represent voltammetries after the treatment
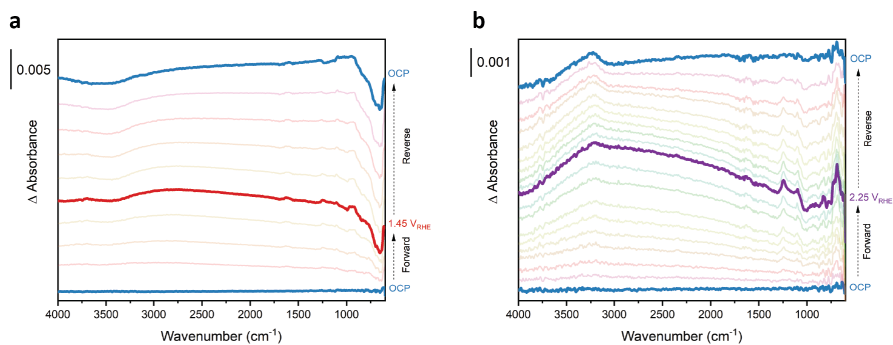
Supplementary Figure S3.8: (a) Infrared spectra of the BiVO$_4$/electrolyte interface during potential stepping in the light (b) Infrared spectra of the BiVO$_4$/electrolyte interface during potential stepping in the dark
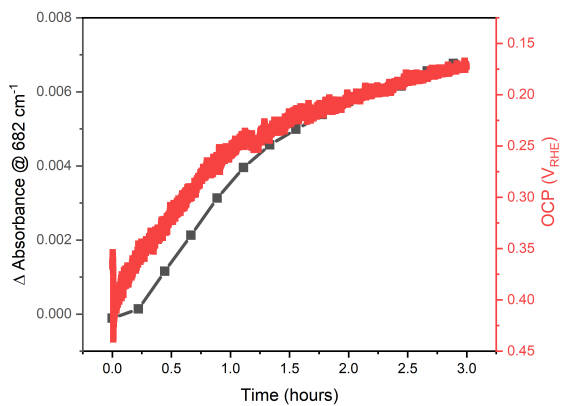
Supplementary Figure S3.9: Temporal evolution of the open circuit potential and the total absorbance at 682 cm^{-1} during photocharging in ultrapure water.
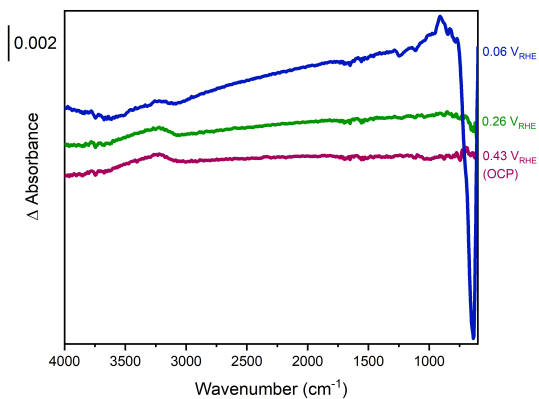
Supplementary Figure S3.10: Infrared spectra of the BiVO$_4$/electrolyte interface when the potential was stepped cathodically (with respect to the open circuit potential).

3.7. References

(1) Venugopal, A.; Kas, R.; Hau, K.; Smith, W. A. *Journal of the American Chemical Society* **2021**, *143*, 18581–18591.

(2) Krol, R. v. d.; Grätzel, M., *Photoelectrochemical Hydrogen Production*; New York: Springer: 2012, pp 3–67.

(3) Yang, Y.; Niu, S.; Han, D.; Liu, T.; Wang, G.; Li, Y. *Advanced Energy Materials* **2017**, *7*, 1–26.

(4) Huang, D.; Wang, K.; Li, L.; Feng, K.; An, N.; Ikeda, S.; Kuang, Y.; Ng, Y.; Jiang, F. *Energy and Environmental Science* **2021**, *14*, 1480–1489.

(5) Pan, L.; Kim, J. H.; Mayer, M. T.; Son, M. K.; Ummadisingu, A.; Lee, J. S.; Hagfeldt, A.; Luo, J.; Grätzel, M. *Nature Catalysis* **2018**, *1*, 412–420.

(6) Digdaya, I. A.; Han, L.; Buijs, T. W.; Zeman, M.; Dam, B.; Smets, A. H.; Smith, W. A. *Energy and Environmental Science* **2015**, *8*, 1585–1593.

(7) Bae, D.; Seger, B.; Vesborg, P. C.; Hansen, O.; Chorkendorff, I. *Chemical Society Reviews* **2017**, *46*, 1933–1954.

(8) Gim, S.; Bisquert, J., *Photoelectrochemical Solar Fuel Production*; Cham: Springer: 2016.

(9) Zachäus, C.; Abdi, F. F.; Peter, L. M.; van de Krol, R. *Chemical Science* **2017**, *8*, 3712–3719.

(10) Lee, D. K.; Choi, K. S. *Nature Energy* **2018**, *3*, 53–60.

(11) Zhong, D. K.; Choi, S.; Gamelin, D. R. *Journal of the American Chemical Society* **2011**, *133*, 18370–18377.

(12) Trotochaud, L.; Mills, T. J.; Boettcher, S. W. *The Journal of Physical Chemistry Letters* **2013**, *4*, 931–935.

(13) Favaro, M.; Abdi, F. F.; Lamers, M.; Crumlin, E. J.; Liu, Z.; Van De Krol, R.; Starr, D. E. *Journal of Physical Chemistry B* **2018**, *122*, 801–809.

(14) Nakamura, R.; Imanishi, A.; Murakoshi, K.; Nakato, Y. *Journal of the American Chemical Society* **2003**, *125*, 7443–7450.

(15) Nakamura, R.; Nakato, Y. *Journal of the American Chemical Society* **2004**, *126*, 1290–1298.

(16) Imanishi, A.; Okamura, T.; Ohashi, N.; Nakamura, R.; Nakato, Y. *Journal of the American Chemical Society* **2007**, *129*, 11569–11578.

(17) Zandi, O.; Hamann, T. W. *Nature Chemistry* **2016**, *8*, 778–783.

(18) Zhang, Y.; Zhang, H.; Liu, A.; Chen, C.; Song, W.; Zhao, J. *Journal of the American Chemical Society* **2018**, *140*, 3264–3269.

(19) Kas, R.; Ayemoba, O.; Firet, N. J.; Middelkoop, J.; Smith, W. A.; Cuesta, A. *ChemPhysChem* **2019**, *20*, 2904–2925.

(20) Morhart, T. A.; Unni, B.; Lardner, M. J.; Burgess, I. J. *Analytical Chemistry* **2017**, *89*, 11818–11824.

(21) Trześniewski, B. J.; Smith, W. A. *Journal of Materials Chemistry A* **2016**, *4*, 2919–2926.

(22) Trześniewski, B. J.; Digdaya, I. A.; Nagaki, T.; Ravishankar, S.; Herraiz-Cardona, I.; Vermaas, D. A.; Longo, A.; Gimenez, S.; Smith, W. A. *Energy & Environmental Science* **2017**, *10*, 1517–1529.

(23) Liu, E. Y.; Thorne, J. E.; He, Y.; Wang, D. *ACS Applied Materials and Interfaces* **2017**, *9*, 22083–22087.

(24) Firet, N. J.; Venugopal, A.; Blommaert, M. A.; Cavallari, C.; Sahle, C. J.; Longo, A.; Smith, W. A. *Chemistry of Materials* **2019**, *31*, 7453–7462.

(25) Venugopal, A.; Smith, W. A. *Faraday Discussions* **2019**, *215*, 175–191.

(26) Deng, J.; Lv, X.; Zhong, J. *Journal of Physical Chemistry C* **2018**, *122*, 29268–29273.

(27) Tao, X.; Shi, W.; Zeng, B.; Zhao, Y.; Ta, N.; Wang, S.; Adenle, A. A.; Li, R.; Li, C. *ACS Catalysis* **2020**, *10*, 5941–5948.

(28) Xie, J.; Yang, P.; Liang, X.; Xiong, J. *ACS Applied Energy Materials* **2018**, *1*, 2769–2775.

(29) Tayebi, M.; Tayyebi, A.; Lee, B. K. *Solar Energy* **2019**, *191*, 427–434.

(30) Wang, S.; Chen, P.; Yun, J.-H.; Hu, Y.; Wang, L. *Angewandte Chemie* **2017**, *129*, 8620–8624.

(31) Meng, Q.; Zhang, B.; Fan, L.; Liu, H.; Valvo, M.; Edström, K.; Cuartero, M.; de Marco, R.; Crespo, G. A.; Sun, L. *Angewandte Chemie - International Edition* **2019**, *58*, 19027–19033.

(32) Abdi, F. F.; Firet, N.; van de Krol, R. *ChemCatChem* **2013**, *5*, 490–496.

(33) Rappich, J.; Lewerenz, H. J. *Thin Solid Films* **1996**, *276*, 25–28.

(34) Amekura, H.; Umeda, N.; Okubo, N.; Kishimoto, N. *Nuclear Instruments and Methods in Physics Research, Section B: Beam Interactions with Materials and Atoms* **2003**, *206*, 1101–1105.

(35) Fatwa Firdaus, A. Towards highly efficient bias-free solar water splitting - PhD Thesis, Ph.D. Thesis, TU Delft, 2013, pp 20–24.

(36) Baral, B.; Parida, K. *Inorganic Chemistry* **2020**, *59*, 10328–10342.

(37) Frost, R. L.; Henry, D. A.; Weier, M. L.; Martens, W. *Journal of Raman Spectroscopy* **2006**, *37*, 722–732.

(38) Gotić, M.; Musić, S.; Ivanda, M.; Šoufek, M.; Popović, S. *Journal of Molecular Structure* **2005**, *744-747*, 535–540.

(39) Longchin, P.; Pookmanee, P.; Satienperakul, S.; Sangsrichan, S.; Puntharod, R.; Kruefu, V.; Kangwansupamonkon, W.; Phanichphant, S. *Integrated Ferroelectrics* **2016**, *175*, 18–24.

(40) Pookmanee, P.; Kojinok, S.; Puntharod, R.; Sangsrichan, S.; Phanichphant, S. *Ferroelectrics* **2013**, *456*, 45–54.

(41) Karabudak, E.; Yüce, E.; Schlautmann, S.; Hansen, O.; Mul, G.; Gardeniers, H. *Physical Chemistry Chemical Physics* **2012**, *14*, 10882–10885.

(42) Oh, Y.-J.; Cho, S. M.; Chung, C.-H. *Journal of The Electrochemical Society* **2005**, *152*, C348.

(43) O'Dwyer, C.; Lavayen, V.; Newcomb, S. B.; Santa Ana, M. A.; Benavente, E.; González, G.; Sotomayor Torres, C. M. *Journal of The Electrochemical Society* **2007**, *154*, K29.

(44) Marzouk, M. A.; El-Kheshen, A. A.; Sayed Ahmed, S. A.; Aboelenin, R. M. *Silicon* **2018**, *10*, 509–517.

(45) Ramana, C. V.; Hussain, O. M.; Pinto, R.; Julien, C. M. *Applied Surface Science* **2003**, *207*, 135–138.

(46) Peak, D.; Luther, G. W.; Sparks, D. L. *Geochimica et Cosmochimica Acta* **2003**, *67*, 2551–2560.

(47) Zhang, S.; Ahmet, I.; Kim, S. H.; Kasian, O.; Mingers, A. M.; Schnell, P.; Kölbach, M.; Lim, J.; Fischer, A.; Mayrhofer, K. J.; Cherevko, S.; Gault, B.; Van De Krol, R.; Scheu, C. *ACS Applied Energy Materials* **2020**, *3*, 9523–9527.

(48) Gao, R.-T.; Wang, L. *Angewandte Chemie* **2020**, *132*, 23294–23299.

(49) Zhang, X. G. In *Corrosion and Electrochemistry of Zinc*; Springer Science & Business Media: 1996, pp 125–156.

(50) Momeni, M.; Wren, J. C. *Faraday Discussions* **2015**, *180*, 113–135.

(51) Lee, D.; Wang, W.; Zhou, C.; Tong, X.; Liu, M.; Galli, G.; Choi, K. S. *Nature Energy* **2021**, *6*, 287–294.

(52) Ye, K. H.; Yu, X.; Qiu, Z.; Zhu, Y.; Lu, X.; Zhang, Y. *RSC Advances* **2015**, *5*, 34152–34156.

(53) Toma, F. M. et al. *Nature Communications* **2016**, *7*, 1–11.

(54) Dupin, J. C.; Gonbeau, D.; Vinatier, P.; Levasseur, A. *Physical Chemistry Chemical Physics* **2000**, *2*, 1319–1324.

4

Chemisorption of anionic species from the electrolyte alters the surface electronic structure and composition of photocharged BiVO$_4$

Photocharging has recently been demonstrated as a powerful method to improve the photo-electrochemical water splitting performance of different metal oxide photoanodes, including BiVO$_4$. In this work, we use ambient-pressure X-ray Raman scattering (XRS) spectroscopy to study the surface electronic structure of photocharged BiVO$_4$. The O K edge spectrum was simulated using the Finite Difference Method Near Edge Structure (FDMNES) method, which revealed a change in electron confinement and occupancy in the conduction band. These insights, combined with ultraviolet-visible spectroscopy (UV-vis) and X-ray photoelectron spectroscopy (XPS) analyses, reveal that a surface layer formed during photocharging creates a heterojunction with BiVO$_4$, leading to favorable band bending and strongly reduced surface recombination. The XRS spectra presented in this work exhibit good agreement with soft X-ray absorption near-edge structure (XANES) spectra from literature, demonstrating that XRS is a powerful tool to study the electronic and structural properties of light elements in semiconductors. Our findings provide direct evidence of the electronic modification of a metal oxide photoanode surface as a result of the adsorption of electrolyte anionic species under operating conditions. This work highlights that the surface adsorption of these electrolyte anionic species is likely present in most studies on metal oxide photoanodes and has serious implications for the photo-electrochemical performance analysis and fundamental understanding of these materials.

4.1. Introduction

Bismuth vanadate ($BiVO_4$) is an extensively investigated n-type metal oxide semiconductor that has shown promising properties for photo-electrochemical (PEC) water splitting.[2] It has generated the highest photocurrent for a metal oxide photoanode to date [3] and the band gap of 2.4 eV could potentially be suitable to make $BiVO_4$ a good top absorber in tandem PEC devices with a low band gap bottom absorber.[4] In addition, the opto-electronic properties of $BiVO_4$ are easily modified: the material can accommodate a large number of defects and dopants, enabling a high degree of material engineering making $BiVO_4$ a suitable model photoanode.[5] Many improvements in the PEC performance of $BiVO_4$ have used the addition of dopants to improve electron conductivity [4, 6], or the addition of co-catalysts to improve the kinetics of the oxygen evolution reaction (OER).[7, 8]

Interestingly, recent work by Zachäus et al.[9] showed that surface recombination is one of the major performance-limiting factors for $BiVO_4$. In fact, the presence of a cobalt phosphate (CoPi) catalyst on the surface of $BiVO_4$ suppresses surface recombination by aiding the transfer of holes from the semiconductor valence band (VB) to the OER intermediates. While CoPi effectively suppresses surface recombination, it also introduces parasitic light absorption, which is unwanted in a practical device.[10] Recently, the photocharging (PC) technique has been introduced on $BiVO_4$ photoanodes, which drastically reduced the onset potential for OER and increased the photocurrent density and fill factor of$_4$ photoanodes to prolonged exposure to AM 1.5 illumination under open circuit conditions in a neutral electrolyte. After extensive material characterization, it was shown that the surface structure of $BiVO_4$ was altered upon photocharging.[11, 12] This treatment lead to a suppression of the surface recombination of photogenerated charge carriers, improving the overall photo-electrochemical performance of $BiVO_4$. In a follow-up work, the pH of the electrolyte was found to have a significant effect on the photocharging enhancement, where an alkaline solution increased the PEC performance more compared to a neutral or slightly acidic electrolyte.[12] Using Intensity-Modulated Photoelectron Spectroscopy (IMPS) and a hole scavenger, Liu et al. quantified the enhancement from photocharging in the bulk and at the surface of $BiVO_4$ in a potassium phosphate buffer.[13] It was demonstrated that photocharging of $BiVO_4$ resulted in a significant enhancement in both the bulk charge separation and surface charge transfer efficiencies. Similar photo-electrochemical enhancements have also been recently shown in other metal oxide photoanodes such as WO_3 [14], $CuWO_4$ [15] and doped Fe_2O_3 [16, 17], showing that the photocharging treatment can be extended beyond $BiVO_4$, and is a potentially generalizable phenomenon.

Recently, Favaro et al. [18] have reported the formation of a $Bi_x(PO_4)_y$ layer at the surface of a $BiVO_4$ photoanode when illuminated in a phosphate buffer under open circuit conditions. A similar copper borate layer was formed during the examination of $CuWO_4$ when it was photocharged in a borate buffer.[15] These results suggest that an overlayer is formed at these metal oxide photoanode surfaces upon illumination by the chemisorption of the electrolyte anionic species. It was proposed that this semiconduct-

ing overlayer then creates a heterojunction with the underlying photoanode, improving the charge separation close to the surface and thus suppressing the surface recombination of the photo-excited charge carriers. To better explain the enhancements in charge separation and suppression of surface recombination of the photocharged electrodes, it is necessary to gain further insights into the modification of the electronic structure of the metal oxide photoanodes by this light-induced overlayer. This knowledge can help to improve the general understanding of an illuminated metal oxide/electrolyte interface, which is crucial for the development of PEC water splitting devices. In this work, $BiVO_4$ is used as a model photoanode to study the changes in its electronic structure during photocharging in a borate electrolyte using a combination of X-ray photoelectron spectroscopy (XPS), ultraviolet-visible spectroscopy (UV-vis) and ambient-pressure (in air) X-ray Raman scattering (XRS) spectroscopy. XPS only penetrates the first ~ 5 nm of the $BiVO_4$ film and therefore provides surface-sensitive information, while both UV-vis and XRS techniques provide bulk-sensitive information. A surface hydroxide layer was found to form spontaneously even when the $BiVO_4$ electrode was placed in the electrolyte in the dark. A bismuth borate layer was formed under the photocharging conditions, creating a heterojunction that resulted in an improved charge separation and decreased charge carrier recombination near the surface as discovered through ab-initio simulations of the O K edge spectra of $BiVO_4$. These findings validate the previous hypotheses proposed in literature [15, 18], about improved band bending in the space charge region (SCR) as a result of the light-induced heterojunction formation. These results highlight the complex and dynamic nature of metal oxide-electrolyte interfaces, and give new insights into the mechanisms for PEC performance enhancement of photocharged $BiVO_4$ photoanodes. More importantly, this work highlights that the surface adsorption of anionic electrolyte species on metal oxide surfaces cannot be ignored, as it has serious implications on the fundamental understanding and performance analysis of metal oxide photoanodes.

4.2. Materials and methods

Fabrication of $BiVO_4$ thin film photoanodes

Thin films of $BiVO_4$ were deposited on fluorine-doped tin oxide (FTO) substrates via spray pyrolysis. The details of the experimental procedure can be found elsewhere.[19] In short, FTO substrates were first coated with ~ 80 nm of SnO_2 while the substrate temperature was kept at 425 °C, and subsequently coated with 200 nm of $BiVO_4$ while the substrate was kept at 450 °C. The samples were then annealed in an air-flushed tube furnace for 2 h at 460 °C.

X-ray Raman scattering spectroscopy

All X-ray Raman scattering spectroscopy data were gathered using the dedicate[20] These experiments were performed in air under atmospheric conditions. A pink beam from four U26 undulators was monochromatized to a 9,686 eV elastic energy, first by using a cryogenically cooled Si(111) monochromator and then a Si(311) Channel Cut post-monochromator. The beam was focused using a mirror system in Kirkpatrick-Baez ge-

ometry yielding a spot size of approximately 50 x 100 μm^2 (V x H) at the sample position. Given the experimental setup, the signal coming from 36 spherically bent Si(660) analyzer crystals in the vertical scattering plane was exploited. The overall energy resolution was 0.7 eV, and the mean momentum transfer was 6.2 ± 0.4 Å^{-1}.

The reference sample used for this study was a BiVO$_4$ film prepared as described above and measured without any further treatment at a 0.5° angle relative to the incidence beam (penetration depth ~60 nm). Pellets of cellulose and vanadium oxide (V$_2$O$_4$ and V$_2$O$_5$ Sigma-Aldrich) were also measured at a 0.5° angle. A grazing incidence angle is required to ensure surface-sensitive measurements when a hard X-ray beam is used. Before the XRS measurements, the dark and PC sample were kept in open circuit conditions in a flow cell with a 0.1 M sodium borate buffer (sodium tetraborate decahydrate (Sigma Aldrich 99.5%) in MilliQ water, while NaOH was added until pH 10 was reached) for 12h in the dark and under illumination, respectively. The flow cell was further equipped with a glass Ag/AgCl reference electrode (XR300, Radiometer Analytical) and a coiled Pt wire as counter electrode both in the dark (dark sample) and under illumination (photocharged sample, 100 mW/cm^2 Xe lamp with water filter). After 12 h, the electrodes were removed from the electrochemical cell, quickly dried under a flow of nitrogen and moved to the experimental hutch for the XRS measurements. The preparation procedure was performed very quickly to ensure the XRS measurements could start less than 15 min after the sample was removed from the electrochemical cell. During the XRS measurements, the incident energy was scanned at a fixed analyzer energy of 9.7 keV in order to create energy losses in the vicinity of the core-electron excitations of interest (L$_{2,3}$ of V and K edge of O). The data collected by 3 pixelated Maxipix detectors [21] were integrated over appropriated Regions Of Interest (ROI), then averaged over the 36 Si(660) analyser crystals and treated with the XRS-tools program package. A background accounting for the valence Compton profile was subtracted as described elsewhere.[22] Finally, a normalization over an area of 40 eV across the edge was applied.

Eight energy loss scans per sample were measured at room temperature, each one at a new sample position to avoid beam radiation damage. All XRS measurements were checked for consistency prior to summation to rule out radiation damage of the sample induced by the X-ray beam.

Ab initio XRS simulations at the O K edge were performed with the Finite Difference Method Near Edge Structure (FDMNES) software package.[23, 24] The calculated spectra were compared to both photocharged and dark samples. The input parameter files of the calculations are reported in the Supporting Information (SI). The vanadium L edges were simulated with Crispy [25] using a multiplet analysis approach.

X-ray photoelectron spectroscopy
XPS spectra were obtained using a Thermo Scientific K-alpha apparatus equipped with an Al K-alpha X-ray Source and a Flood Gun for charge compensation of the sample. Parameters used for the measurements were: spot size of 400 μm, pass energy of 50 eV, energy step size of 0.1 eV, dwell time of 50 ms, 10 scans in the vicinity of the Bi 4f,

C 1s, Na 1s, O 1s and V 2p orbital binding energy with alternative scan numbers for B 1s (200 scans) and the valence band (50 scans). Samples were rinsed and dried before measuring.

UV-Vis spectroscopy
UV-Vis transmission measurements were performed on the reference, dark and the photocharged $BiVO_4$ samples using a Perkin Elmer Lambda 900 UV/Vis/NIR spectrometer. The transmission measurements were performed inside an integration sphere in the transmittance mode (%T). Data was recorded with a 15° tilt in the sample, with respect to the incident light beam to minimize reflection. A scan rate of 250 nm/min and an integration time of 0.2 s were used for the data capture. The absorption coefficient and the Tauc plot were calculated from the transmittance data using the formulas in the SI.

High-resolution Scanning Electron Microscopy
HR-SEM images were taken with a Nova NanoSEM at an accelerating voltage of 10 kV.

4.3. Results

To gain further insights into the mechanisms of the photo-electrochemical enhancement that arise from the photocharging procedure in $BiVO_4$, several material properties of $BiVO_4$ were investigated before and after photocharging. In particular, the influence of placing the photoanodes in solution under open circuit conditions with and without illumination were examined. A reference $BiVO_4$ sample (as-deposited) was compared to both a $BiVO_4$ film that was kept under open circuit conditions and AM 1.5 light illumination (i.e. photocharged) for 12 h, and a $BiVO_4$ film that was kept in open circuit for 12 h in the dark. The samples are referred to as untreated $BiVO_4$, photocharged $BiVO_4$ (PC-$BiVO_4$) and dark $BiVO_4$, respectively. The samples were studied through several spectroscopic techniques, including UV-Vis spectroscopy, XPS and XRS. Both XPS and XRS give electronic and structural information on the film, however due to the difference in penetrating depth of the X-rays in the different experiments, XPS gives information about the surface of the films while XRS provides information on the structure up to 60 nm into the bulk of $BiVO_4$.

X-ray photoelectron spectroscopy
XPS measurements were performed on reference, dark and PC-$BiVO_4$ films, and the results are shown in Figure 4.1. The presented spectra are background subtracted and energy corrected with the C 1s signal (Figure S4.1 (d)). Several trends can be observed between the different samples. The Bi 4f peaks are shown in Figure 1a, and a shift was observed from 159.5 eV for the reference sample to 159.0 eV and 158.7 eV for the dark and photocharged $BiVO_4$, respectively. This shift is accompanied by slight broadening of the Bi 4f peaks for the dark and the photocharged samples, as shown with the increase in full width at half-maximum (FWHM) in Table S4.2. A signal from the B 1s spectrum is not present in the reference sample, while it appears very small in the dark and is much more pronounced in the PC-$BiVO_4$, as seen in Figure 4.1 (b). In Figure 4.1 (c), the main signal from the oxygen (O 1s) spectra was observed to decrease slightly in binding energy from 530.3 eV for the reference sample to 529.9 eV and 529.6 eV for the dark and
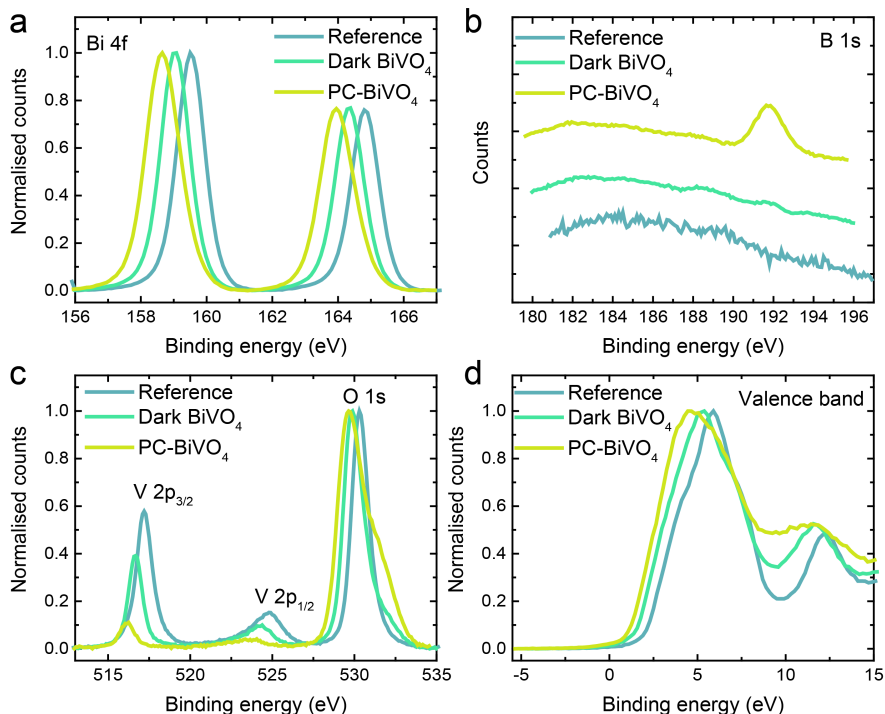
We therefore ascribe the shift and the broadening of the Bi 4f peak, the emergence of the O 1s shoulder together with the B 1s peak to reveal the formation of a surface bismuth borate layer during photocharging. This surface borate layer is very similar to the phosphate layer found by Favaro et al. In addition to the XPS data given for Bi, B and O, we also observed a shift toward lower binding energies for the V 2p signal, which indicates a reduction in the oxidation state of the vanadium.[12]

When considering the difference between the dark and photocharged samples, it is interesting to note that the electronic features of the dark sample show an intermediate phase between the photocharged and the reference sample. Since the dark sample has no clear B 1s signal, yet still has a partial shoulder in the O 1s spectrum, it is likely that this sample instead has a surface coverage of bismuth hydroxide as previously reported.11 Since the binding energies for Bi-O-B and Bi-O-H are almost identical (the electronegativity values of H and B are 2.2 and 2.0, respectively), the distinction is difficult to make without analysing the B 1s signal as well.

The valence band (VB) of the reference, dark and PC-BiVO$_4$ electrodes was also examined, and is shown in Figure 4.1 (d). It can be seen from this figure that similar to the previously observed shifts in the binding energy of Bi, O and V, there is also a shift in the valence band energy toward lower binding energies when looking at the reference, dark and PC-BiVO$_4$ samples, respectively. A broadening to lower binding energy of the valence band spectra of the dark and PC-BiVO$_4$ is also visible here, due to the convolution of the VB spectra of bismuth hydroxide/bismuth borate and bismuth vanadate, respectively. These results indicate that the bismuth borate layer formed on the surface has a valence band closer to the Fermi level of the composite system. The exact composition of the bismuth borate surface layer is unknown, but from prior work on bismuth borate glasses, we can estimate the band gap of the bismuth borate layer to be equal to or larger than that of BiVO$_4$.[21, 27]

The unidirectional peak shifts in the Bi 4f, V 2p, O 1s and VB XPS spectra to lower binding energies are in part an electronic effect. Band bending caused by the equilibration of the Fermi level of BiVO$_4$ and the chemisorbed anionic surface layer shifts the XPS spectra. Similar XPS peak shifts were observed by Hermans et al. [28] where different metal oxide surface layers were deposited on BiVO$_4$, and the peak shifts were attributed to a change in Fermi level position because of the surface layer induced band bending. NiO and CoO$_x$ surface layers lead to an upward band bending whereas indium-doped tin oxide induced a downward band bending in BiVO$_4$, due to the differences in their respective work functions compared to that of BiVO$_4$. The core level XPS spectra shifted to lower binding energies with the deposition of NiO and CoO$_x$ overlayers, similar to the shifts seen with dark and PC-BiVO$_4$ in this study. Note that band bending induced shifts should be equal in magnitude for different core levels. Table S4.3 shows that the shifts for V and Bi are larger than for O, meaning that the V and Bi shifts also have a chemical component to them, assigned above as a reduction in V oxidation state and the appearance of the Bi borate surface layer.

The formation of the bismuth borate layer at the surface forms a heterojunction with the $BiVO_4$ as well as induces an upward band bending, and reduces photogenerated charge recombination at the semiconductor-liquid junction (SLJ). The cathodic Fermi level shift that was observed with the open circuit potential (OCP) measurements for the dark and photocharged samples, as shown in Figure S4.2, is another evidence of the band bending observed through the XPS shifts.

Ultraviolet-visible spectroscopy

UV-vis spectroscopy was performed before and after the photocharging process to determine if there were any optical changes in the $BiVO_4$ films during the treatment that may arise from the formation of the bismuth borate surface layer. In Figure 4.2 (a), the spectra of a dark (green) and photocharged (yellow) sample are shown together with their corresponding spectra before treatment. A small increase in absorption is found within the band gap of $BiVO_4$ for the photocharged sample, while the dark sample does not show this increase in absorption. Just outside the band gap energy, between 475 and 700 nm, the photocharged sample shows a very distinct absorption feature.
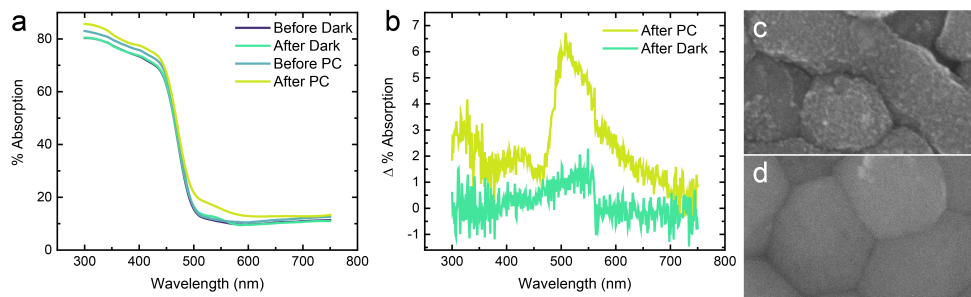
Figure 4.2: (a) UV-vis absorption spectra of a dark $BiVO_4$, before (purple) and after (green) the treatment and photocharged $BiVO_4$ before (blue) and after (yellow) the treatment. (b) Difference spectra between before and after showing a defect-related feature in the PC sample. (c) HR-SEM image of PC-$BiVO_4$, showing small particles (white spots), finely dispersed over the $BiVO_4$ grains. (d) HR-SEM image of dark $BiVO_4$. Width of HR-SEM images is 520 nm.

The absorption increase inside the band gap could explain part of the improved OER activity of the PC-$BiVO_4$ sample, but cannot account for the observed 3-fold increase in the incident photon-to-current conversion efficiency (IPCE).[11] To determine whether the choice of buffer anion has any effect on this absorption feature, photocharging was performed in a phosphate buffer at pH 10. This treatment revealed a very similar improvement within the absorption spectra post photocharging (Figure S4.3 (a)). When subtracting the spectrum of the before-PC from the after-PC spectrum (Figure 4.2 (b)), a feature emerges that resembles either a surface plasmon resonance (SPR) mode with a peak in absorption around 520 nm or a defect-related absorption in PC-$BiVO_4$. The dark sample only has a minor increase in this region, but still shows a feature with a peak centered around 520 nm. Plasmonic features of vanadium oxide are only found in the infra-red [29], and those for metallic vanadium are found in the UV region [30],

whereas metallic bismuth nanoparticles in an oxide medium can give rise to plasmonic features around 500 nm.[21, 31] However, the Bi 4f XPS spectra does not show any indication of the presence of metallic bismuth in the PC-BiVO$_4$. Therefore, we tentatively assign this feature to a defect-related light absorption in PC-BiVO$_4$. In fact, such above bandgap optical features have been observed with some metal oxides [32, 33] and have often been attributed to defect-related light absorption, induced by surface oxygen vacancies. Therefore, the anion adsorption on the BiVO4$_4$ surface upon photocharging could have introduced surface oxygen vacancies through surface restructuring. A high resolution scanning electron microscopy (HR-SEM) image of PC-BiVO$_4$ (Figure 4.2 (c)) shows severe roughening of the surface on the nanoscale, compared to the dark and reference sample (Figure 4.2 (d) and S4.3 (c), respectively). This surface roughening could be a result of the surface restructuring to accommodate the buffer anion adsorption.

X-ray Raman scattering

To gain further insight into the structural and electronic changes induced by the photocharging treatment, the vanadium L$_2$ and L$_3$ edge and the oxygen K edge were probed using X-ray Raman scattering spectroscopy in near in situ conditions. X-ray absorption spectroscopy uses soft X-rays to probe light elements (<1 keV); however, these X-rays require ultra-high vacuum (UHV) conditions and are therefore less suitable for in situ studies. Instead, XRS allows the use of hard X-rays to probe elements with core-electron excitation energies in the soft X-ray regime i.e. lower than 1 keV. The use of hard X-rays leads to a bulk sensitive approach and can offer the possibility of working under operando conditions. In this work, we were able to study the BiVO$_4$ structure at room temperature and pressure and measure spectra immediately after the photocharging treatment was performed. Real operando conditions would greatly complicate the analysis of the O K edge spectrum since the electrolyte also contains oxygen, and instead this near in situ approach was adopted. A grazing incidence angle was maintained to avoid contributions from the oxygen-containing FTO substrate and to increase the footprint of the X-ray beam on the sample. The vanadium L$_3$ and L$_2$ edges and oxygen K edge can be probed within the same measurement since their absorption energies are very close. The electronic structure of the various BiVO$_4$ samples is obtained from XRS data by simulating the data with ab-initio based calculations.

The effect of photocharging on the electronic states in the conduction band of BiVO$_4$ was studied by comparing a photocharged (PC) sample and a 'dark' sample to a reference sample. To try and preserve the operando state, the samples were not rinsed but only dried before being transferred to the XRS measurement chamber. All samples were fabricated according to the same procedure and XRS measurements were taken under identical settings. The XRS spectra of the three samples are shown together in Figure 4.3.

The region from 515 to 545 eV covers the core-electron excitations of interest, namely the vanadium L$_2$ and L$_3$ and oxygen K edges. For low transferred momenta, the orbital selection rule dictates $\delta l = \pm 1$, where l is the azimuthal quantum number. Therefore, the vanadium L edge excitation results in a transition to the first available vanadium d orbital, and the oxygen K edge excitation transitions to the first unoccupied oxygen p
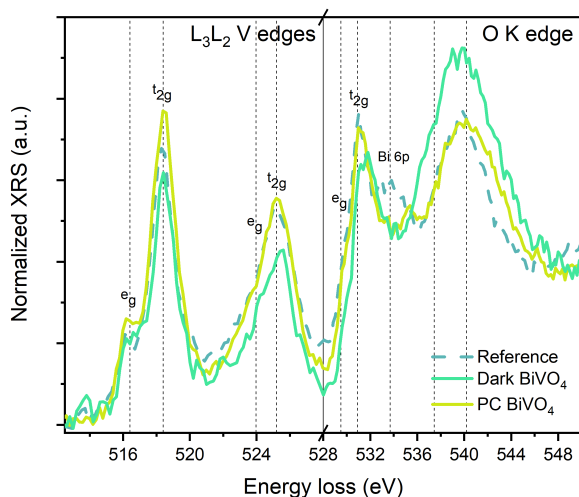
Figure 4.3: Normalised XRS spectra of the vanadium L_2, L_3 and the oxygen K edge region of a reference, dark and PC-BiVO$_4$ sample. The changing ratio of the O K edge peaks reveals a filling with electrons of the pre-edge peak (O 2p - V 3d e_g/t_{2g}) for the dark sample.

orbital.

The XRS spectrum of the reference thin film BiVO$_4$ sample (dashed blue line in Figure 4.3) is discussed first. Four main peaks with shoulders to the left of the first three peaks are easily discernible. The first main peak between 515-520 eV corresponds to the V L$_3$ edge: the excitation from V 2p3/2 to conduction band V 3d states; the second main peak from 521 – 528 eV is the V L$_2$ edge: the excitation from 2p1/2 to the conduction band V 3d states.[34] The L$_3$ region consists of a main peak at 518 eV and a shoulder at 516 eV, which are the t_{2g} (main peak) and e_g (left shoulder) states of the VO$_4$ structure within the BiVO$_4$ lattice.[34, 35] The V 3d orbitals are hybridized with the O 2p orbital. The L2 edge is excited to the same (hybridized) V 3d t_{2g} and e_g states, however, this part of the spectrum is noisier than the V L$_3$ edge because the core-hole lifetime at the L$_2$ edge is shorter resulting in a broader spectrum. All excited state energies that are visible in Figure 4.3 are given in Table 4.1 with their corresponding orbital transitions. Overall, the XRS spectrum shows good agreement with soft X-ray XANES spectra of BiVO$_4$ in literature[34, 35]

The oxygen K excitations extend from 528 eV upwards, and consist of transitions from the occupied O 1s orbital close to the core of the oxygen atom, to the unoccupied O 2p states. A peak at 531 eV and its shoulder at 530 eV show the O 2p – V 3d hybridization, and thus represent the same orbitals as the V L$_2$ and L$_3$ edge spectrum. Therefore, again these peaks are split into the e_g and t_{2g} states according to the tetrahedral crystal field splitting.[34] A second strong peak in the spectrum at 534 eV corresponds to

Table 4.1: All Assigned Peaks of the Reference $BiVO_4$ sample, as depicted in Figure 3

Probed edge	Energy (eV)	Electronic transition
V L_3		From $2p_{3/2}$ to unoccupied V 3d states
	516	to e_g V 3d – O 2p ($d_{x^2-y^2}$, d_{z^2})
	518	to t2g V 3d – O 2p (d_{xy}, d_{xz}, d_{yz})
V L_2		From $2p_{1/2}$ to unoccupied V 3d states
	523	to to e_g V 3d – O 2p
	525	to t_{2g} V 3d – O 2p
O K		From O 1s to unoccupied O 2p states
	530	to e_g V 3d – O 2p
	532	to t_{2g} V 3d – O 2p
	534	to π^* Bi 6p – O 2p
	540	to σ^* from V 4s and Bi 6s with O 2p

4

anti-bonding π O 2p - Bi 6p states.[35, 36] The final peak at 540 eV is the excitation to anti-bonding states of σ character originating from the hybridization of both V 4s and Bi 6s with O 2p.[34, 37] Since the hybridization between V and O is stronger than between Bi and O, the O K edge spectra mainly consist of V – O states.[37]

According to Cooper et al., the hybridized V 3d – O 2p orbitals are not simply split into the e_g and t_{2g} tetrahedral molecular orbitals, instead, three different V 3d contributions should be present in the spectrum.[35] This is due to the fact that the monoclinic scheelite (ms) form of $BiVO_4$ has lattice distortions causing the tetrahedral and dodecahedral symmetries to be broken. In fact, two separate V-O bond lengths and 4 separate Bi-O bond lengths are reported.[37] Therefore, the VO_4 has a C2 symmetry, leading to triplet splitting of the V 3d orbitals. This is not easily discernible from the measured spectrum because of the lower resolution of XRS compared to standard soft X-ray XANES. However, it is important to realize that the broad peaks observed are composed of overlapping contributions of several orbitals.

XRS spectra of V^{4+} and V^{5+} reference samples were collected to help interpret the oxidation state of V in $BiVO_4$. These reference spectra were plotted together with those of reference, dark and photocharged $BiVO_4$ and are presented in Figure 4.4 (a). As is evident from the figure, the peaks of the V^{4+} reference sample (dark blue) are shifted to lower binding energies as compared to the peaks of the V^{5+} sample (purple). This is in very good agreement with the other studies in literature.[38, 39] Another interesting aspect is that the peaks in the V L edge spectra for the reference, dark and PC-$BiVO_4$ are in between the V^{4+} and V^{5+} L edge reference spectra. From this, it can be concluded that the spray deposited $BiVO_4$ has a mix of V^{4+} and V^{5+} oxidation states. In an ideal $BiVO_4$ lattice, the vanadium species should have a 5+ oxidation state. However, it is very common to have intrinsic defects in the structure, in the form of oxygen vacancies. These oxygen vacancies are responsible for the n-type character of monoclinic $BiVO_4$. Due to
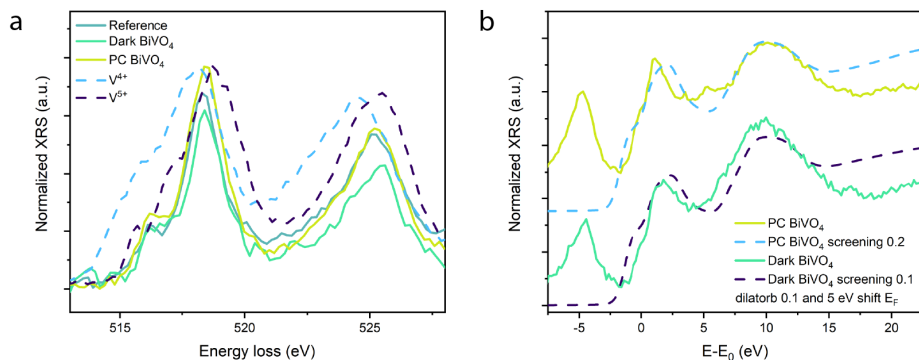
Figure 4.4: (a) XRS spectra of the vanadium oxides (V_2O_4 and V_2O_5) are presented together with the reference, dark and PC-BiVO$_4$ to show the effect of changing V oxidation state on the peak position in the V L$_2$ and L$_3$ edge spectra. (b) The O K edge spectra of the dark and PC sample are overlaid with ab initio simulations including the semi-empirical dilatorb and screening parameters.

4

these oxygen vacancies, to maintain charge neutrality, some vanadium species in the BiVO$_4$ lattice could exist in the 4+ oxidation state. Rossell et al.[40] quantified the vanadium oxidation state in monoclinic BiVO$_4$ using energy-loss spectroscopy and suggested that the surface vanadium ions predominantly exist in a ∼ 4+ oxidation state, due to the presence of a significant amount of oxygen vacancies.

To better understand these results, it is important to consider the penetration depth of the performed XRS measurements. Due to the grazing incidence angle of 0.5°, only the first 60 nm are probed. Additionally, the spray deposited BiVO$_4$ is highly nanostructured and hence has a high surface-to-volume ratio. Therefore, the obtained vanadium L edge spectra for the reference, dark and photocharged samples could be an average of the surface and bulk oxidation state of vanadium who fall between the 4+ and 5+ oxidation state. These results are in alignment with the XRD diffractograms that show a strong resemblance between the reference and photocharged samples, both having monoclinic scheelite BiVO$_4$ features (Figure S4.4).[41] The reference, dark and photocharged BiVO$_4$ have similar vanadium L edge peak positions. However, the dark and PC-BiVO$_4$ show a slightly different ratio in intensity between the V L$_3$ and L$_2$ edges compared to the reference spectra. A multiplet analysis was performed to predict the shape of the V L edge spectra for a vanadium species in its V^{4+} and V^{5+} oxidation state, in a hypothetical bismuth-vanadium oxide compound. These results are shown in Figure S4.5 and suggest that there could be a decrease in the oxidation state of vanadium, with an increase in the L$_3$/L$_2$ peak ratio. The V L$_3$/L$_2$ peak ratio is indeed higher for the dark and PC-BiVO$_4$ compared to the reference (Table S4.3) and would suggest a decrease in the oxidation state of vanadium, possibly from the creation of additional oxygen vacancies at the surface. This would be in agreement with the above bandgap absorption feature seen in the absorption spectra of the PC-BiVO$_4$ and with the shift in the V 2p XPS spectrum. However, the low resolution of the XRS technique coupled with the surface and bulk averaging of the

XRS technique, makes this comparison difficult. Screening of V 2p XPS spectra by the surface adsorbed layer also makes the comparison of the V 2p XPS spectra difficult. Additional experiments will be needed to study and quantify the vanadium oxidation state change in the dark and the photocharged sample, which is out of the scope of this work.

A disappearance of the O 2p - Bi 6p peak at 534 eV was observed for both the PC sample and the dark sample. As mentioned previously, the Bi – O hybridization is not very strong, therefore a small change in the electronic structure can make the Bi 6p signal less visible, this appears to be the case for the dark sample. Bismuth borate withdraws bismuth from $BiVO_4$, which leads to the reduction of the O 2p – Bi 6p signal in the XRS spectrum of the photocharged $BiVO_4$. The broadening of the mixed metal sp – O 2p peak implies the existence of multiple orbitals that partly overlap in energy. This can be caused by the presence of multiple V oxidation states that all have molecular orbitals of slightly different energy.

The main difference between the dark and PC-$BiVO_4$ XRS spectra is the filling with electrons of the V 3d states of the dark sample, as observed from a difference in peak height ratio between the pre-edge peak (V 3d – O 2p) and the main peak (mixed metal sp – O 2p) in the O K edge spectrum. This lowering of the pre-edge peak implies a filling of the d states, resulting in a higher concentration of electrons for the dark sample compared to the reference and photocharged samples. The reason for this difference is not immediately obvious, so to further elucidate and quantify the influence of the photocharging treatment on the electronic structure of $BiVO_4$, ab initio simulations at the O K edge were performed with the FDMNES program package. The calculated spectra were compared to the experimentally obtained XRS spectra (the input parameter files of the calculations are shown in the SI). In order to simulate the peak height ratios observed in the experimental XRS spectra, two semi-empirical parameters, the dilatorb and screening parameter were used in the calculations. The dilatorb and screening parameters allow the ability to tune the height of the pre-edge peaks and their position with respect to the main edge. Moreover, the dilatorb parameter allows the ability to consider the degree of ionicity of oxygen in the lattice structure by modifying the valence orbitals. Modifying this parameter means either dilating or contracting the valence orbitals, which is a necessary procedure when modelling anions with this package since the default is fully covalent, not considering the ionic character of oxygen.[42] Anions have a more negative charge and are larger than their covalent radius because of the extra electrons that the anions take from the cations. The effect of changing the dilatorb parameter is shown in Figure S4.6.

The screening parameter is used to simulate a not fully screened core-hole in the absorbing atom, meaning that part of the electron charge in the conduction band is missing. When the total excited electron is present in the conduction band, no charge is missing and the core-hole is considered fully screened. The screening parameter generally points to a correlation effect caused by the presence of the excited 3d electrons that hinder the screening process. In this respect, the screening value is an indication of the filling with electrons of the conduction band. However, oxygen electrons can behave

unexpectedly to the removal of electrons, and it is therefore not always possible to predict the pattern in the O K edge spectra as a function of electron depletion. Instead, the screening parameter can help making the trends of the spectra quantifiable. The effect of changing the screening parameter is shown in Figure S4.7.

If the effects of the dilatorb and the screening value are now combined, it is possible to effectively simulate the XRS spectra. The best fitting simulations are shown in Figure 4.4 and S4.6. The reference spectrum (Figure S4.8) was fitted with a dilatorb value of 0.1 and no screening potential. The dark sample is fitted with a screening value of 0.1 and the dilatorb set to 0.1. The photocharged sample on the other hand is fitted with a screening parameter of 0.2 and a dilatorb value of 0.1. The default value for the screening parameter is 0 in the FDMNES software, so the lack of a defined screening value in the reference sample should be understood as full screening. The trend in the screening between the different samples is therefore: reference > dark > photocharged $BiVO_4$. The difference in screening value between the dark and PC spectra can be explained by the photocharged sample having less electrons in the conduction band than the dark sample in the area measured by XRS, which also explains the pre-edge filling of the dark sample observed in Figure 4.3. The screening value of 0.2 for PC-$BiVO_4$ is significantly higher with respect to the value of 0 that was used for the reference sample, showing strong structural changes in $BiVO_4$ as a result of the photocharging treatment. A higher screening value also indicates a shift to a lower Fermi level since less electrons are present in the conduction band. Less electrons for the photocharged sample might seem counterintuitive, but in fact it is a consequence of improved band bending induced by the heterojunction between $BiVO_4$ and the surface formed bismuth borate layer. The fact that electrons are driven away from the surface by band bending is responsible for the strong suppression of surface recombination induced by the photocharging treatment. The decrease in Fermi level is also introduced in the simulations. The dark sample also has less electrons compared to the reference sample and a lower Fermi level, but the changes are smaller as compared to the photocharged sample.

4.4. Discussion

The XPS analysis confirmed the formation of a bismuth borate surface layer on $BiVO_4$, upon photocharging. The shifts of the core level XPS spectra, to lower binding energies upon photocharging, suggested that this borate surface layer induced an upward band bending within $BiVO_4$ (Figure 4.5 (a)). Similar conclusions could be drawn in the case of the dark samples. After 18 h under open circuit conditions in the dark, the dark sample has an OH coverage that initially improves the photo-electrochemical performance of the sample (Figure S4.9). This improvement is, however, smaller than the PEC improvement of the PC samples and is not maintained over time because the OH species are removed from the surface during water oxidation. Both the dark and photocharged samples demonstrated a higher open circuit potential in the dark than the reference sample (Figure S4.2), resulting in a Fermi level closer to the conduction band in the bulk, as depicted in Figure 4.5 (a). To determine whether the bismuth borate and OH surface layers

had any effect on the bulk structure of $BiVO_4$, both UV-Vis and XRS measurements were performed. The UV-Vis spectra revealed a change in absorption post photocharging, with the formation of an above bandgap absorption feature. This feature was attributed to a defect-related absorption, possibly from the creation of surface oxygen vacancies. To gain a deeper understanding of the electronic effect of the bismuth borate layer on $BiVO_4$, XRS measurements were performed. These results showed that the hybridized Bi 6p – O 2p orbital disappeared, which corresponds well with the formation of a Bi surface layer. In addition, the ab-initio simulations of the O K edge spectra revealed a decrease in the Fermi level of the PC-$BiVO_4$. This can be explained by band bending induced by the surface borate layer. Bismuth borate has a larger band gap than $BiVO_4$ and according to the valence band spectra (Figure 4.1 (d)) its valence band lies closer to the Fermi level than the valence band of $BiVO_4$. This means that the heterojunction of $BiVO_4$ and bismuth borate will create strong band bending and a significant space charge region (SCR) of several tens of nanometers (Figure 4.5 (a)).[43, 44] The SCR coincides with the region that is probed by XRS. Since the band bending forces electrons toward the back contact, the SCR will contain fewer electrons than in the case of a flat band situation. The monolayer of OH on the surface of the dark $BiVO_4$ sample has a similar band bending effect that directs the electrons toward the back contact, away from the surface.
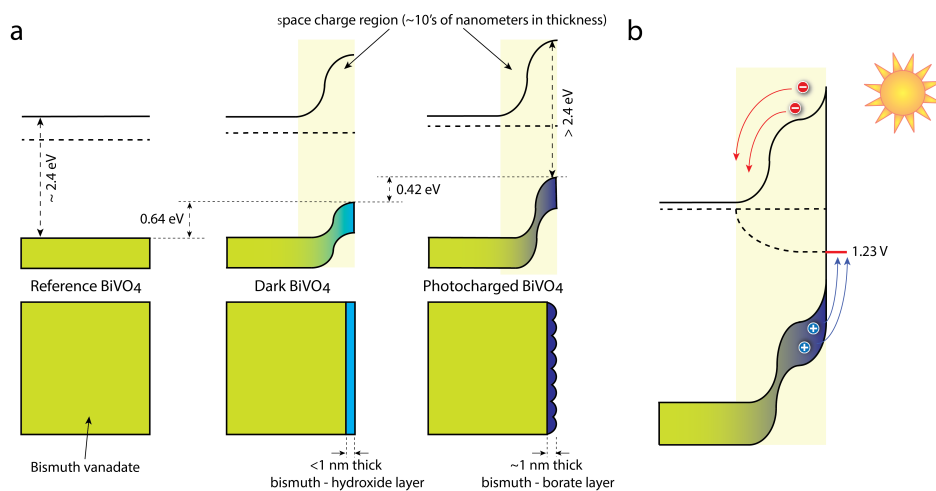
Figure 4.5: The effect of photocharging on the band gap region and the Fermi level of $BiVO_4$. (a) The hydroxide (dark sample) and bismuth borate (PC sample) surface layers have a valence band closer to the Fermi level, introducing band bending at the surface. The band bending directs electrons towards the bulk of $BiVO_4$, leading to a reduced electron concentration in the space charge region for PC-$BiVO_4$. Note that the bulk band gap size is not altered by the PC treatment (Figure S4.10). (b) The effect of photocharging on a $BiVO_4$ photoanode in contact with an electrolyte under illumination. The additional band bending improves the charge separation, leading to the unrivaled PEC properties of PC-$BiVO_4$.

The XRS results from this work suggest that there is a severe alteration in the surface electronic structure when $BiVO_4$ comes in contact with an electrolyte, even without illumination. This is also supported by the changes visible in the data obtained from XPS

and HR-SEM. The initiator of this surface restructuring could be the surface adsorption of electrolyte anionic species, borate in the case of the PC-$BiVO_4$ and hydroxide in the case of dark $BiVO_4$. The heterojunctions formed as a result of this surface adsorption improve the charge separation close to the surface, and thus suppress surface recombination. Since other metal oxides [14–16] were also shown to photocharge like $BiVO_4$, these findings could be generalized.

Additionally, this time-dependent surface layer formation shows that the metal oxide/electrolyte interface is very dynamic. Reversibility of the photocharging effect [11] in the dark could be explained by the desorption of this buffer anion surface layer under dark conditions, which was also shown by Favaro et al. [18] The dynamic nature of the metal oxide/electrolyte interface makes it difficult for the photoanode material to be stable for long-term operation. The constant switching between the dark and light conditions, as in a practical case where intermittent sunlight drives the reaction, would imply constant surface restructuring of the photoanode material. Some material from the surface could be lost in each of these restructuring steps, in addition to other corrosion mechanisms occurring at the surface of a photoanode material.

It is important to emphasize that this surface layer formation, in the dark and under illumination, from the electrolyte anionic species has been "ever-present" in metal oxide photoanodes. This work highlights that the choice of electrolyte/buffer solutions needs to be considered when making comparisons of PEC performance of different systems with the same metal oxide semiconductor. The surface layer formed would be different with different electrolytes and hence the resultant heterojunction would be different as well. However, the importance or the effect of the electrolyte has been largely unnoticed in the PEC research field when analysing material surfaces after photo-electrochemical measurements. This current study is a strong indicator that the effect of surface adsorption of electrolyte anionic species can have serious implications on PEC measurements and should be given due regard for future works in the field.

4.5. Conclusions

The photocharging treatment of $BiVO_4$ was studied using a sequence of XPS, UV-Vis and XRS techniques. The XPS studies revealed the formation of a surface borate layer on the $BiVO_4$ surface, upon illumination in open circuit conditions. The borate anion from the electrolyte covalently bonded with the bismuth ions in the $BiVO_4$, resulting in a $BiVO_4$/bismuth borate heterojunction near the surface. This heterojunction resulted in improved band bending near the surface, improving the charge separation and suppressing the surface recombination of charge carriers. The improved band bending, as a result of the heterojunction, explains the enhancement in the PEC performance of photocharged $BiVO_4$. In a similar manner, a $BiVO_4$ sample kept under open circuit conditions in the dark formed an OH layer at the surface, leading to a relatively smaller degree of band bending and a short-lived PEC performance enhancement.

The UV-Vis studies showed the formation of a new absorption feature, outside the bandgap of $BiVO_4$, upon photocharging. This feature was attributed to a defect-related absorption, resulting from the surface restructuring during photocharging. This surface restructuring during photocharging was confirmed using HR-SEM images. A combination of XRS studies and ab-initio simulations on the oxygen K edge spectra revealed a decrease in the electron occupancy in the space charge region of the dark and PC-$BiVO_4$, confirming the improvement in band bending after the dark and photocharging treatment. Additionally, the XPS, UV-Vis and XRS measurements indicated a decrease in the oxidation state of the surface vanadium species due to the anion adsorption. Further experiments are required to quantify this change.

A strong agreement was found between the XRS spectra obtained in this work and soft X-ray XANES spectra from others, indicating that XRS is a very powerful tool to study semiconductors in (near) in-situ conditions with a larger probing depth than allowed by soft X-ray techniques. The dynamic nature of the metal oxide/electrolyte interface will have strong implications on the long-term stability of metal oxide photoanodes. The effect of surface adsorption of electrolyte anionic species on the surface structure of metal oxide photoelectrodes is often overlooked within the PEC research field. Our results show that this time-dependent surface adsorption of electrolyte anionic species on the metal oxide photoanode surface plays an important role in defining the electronic and catalytic properties of a photoanode. Anionic adsorption was shown to form a heterojunction at the surface which improved charge separation and suppressed surface recombination. The effect of the electrolyte on the metal oxide photoanode surface and the time-scale of the surface adsorption of these anions cannot be ignored, and hence should be taken into consideration while performing analyses and gaining mechanistic understanding of reactions on metal oxide photoanodes surfaces.

4

4.6. Supplementary information
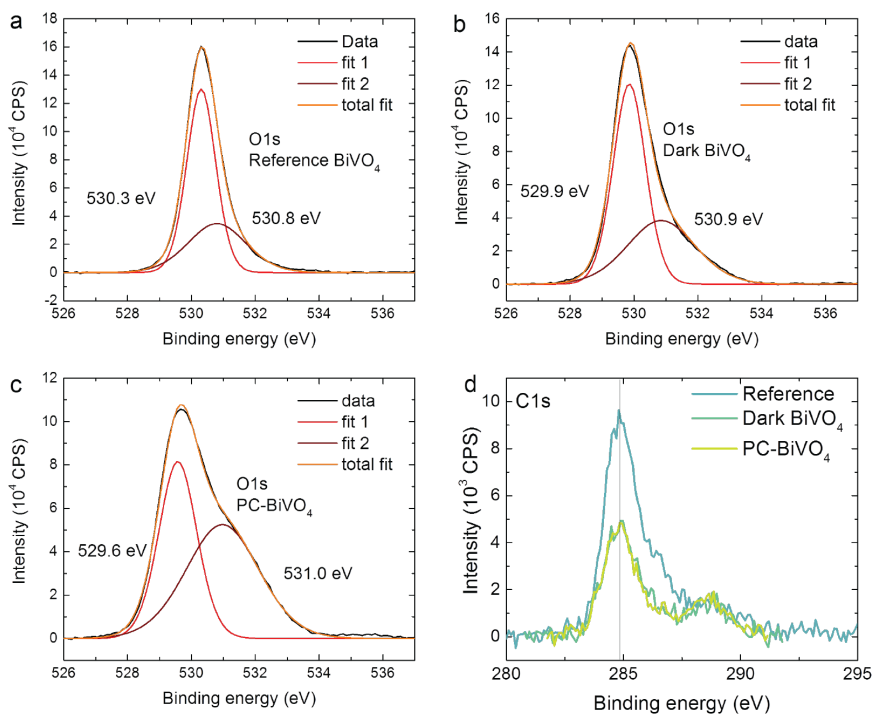
Supplementary Figure S4.1: Deconvoluted O 1s XPS spectra for (a) reference $BiVO_4$, (b) dark $BiVO_4$ and (c) PC-BiVO$_4$. (d) C1s spectra showing the C correction to 284.8 eV.

Table 4.2: Gaussian fits of Bi 4f spectra from Figure 4.1 (a). All values are given in eV.

		Ref	Dark	PC
Centre	Bi $4f_{5/2}$	164.82	164.34	163.97
FWHM	Bi $4f_{5/2}$	1.05	1.07	1.27
Centre	Bi $4f_{7/2}$	159.52	159.04	158.67
FWHM	Bi $4f_{7/2}$	1.04	1.07	1.26

Table 4.3: Gaussian peak fits of core level spectra and valence band onset values from Figure 4.1. All values are given in eV.

	Ref	Dark	Ref-Dark (Dark shift)	PC	Ref-PC (PC shift)
O 1s main	530.29	529.85	0.44	529.57	0.72
O 1s shoulder	530.8	530.85	-0.05	530097	-0.17
V $2p_{3/2}$	517.21	516.67	0.54	516.16	1.05
Bi $4f_{5/2}$	162.82	164.34	0.48	163.97	0.85
VB onset	1.94	1.42	0.52	1.06	0.88
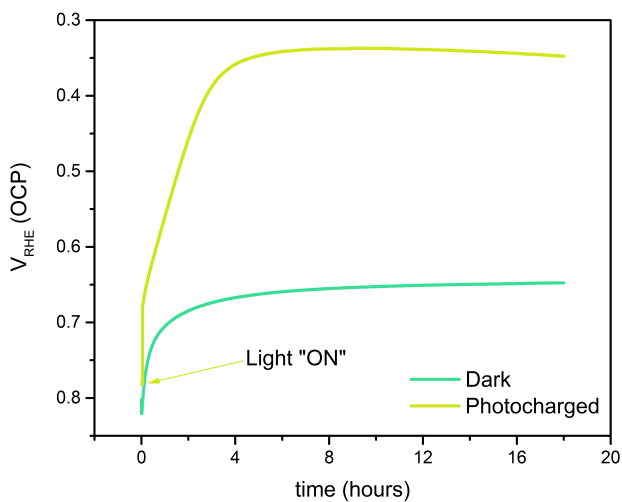
Supplementary Figure S4.2: Plot of OCP vs time for dark and PC-BiVO$_4$.

4
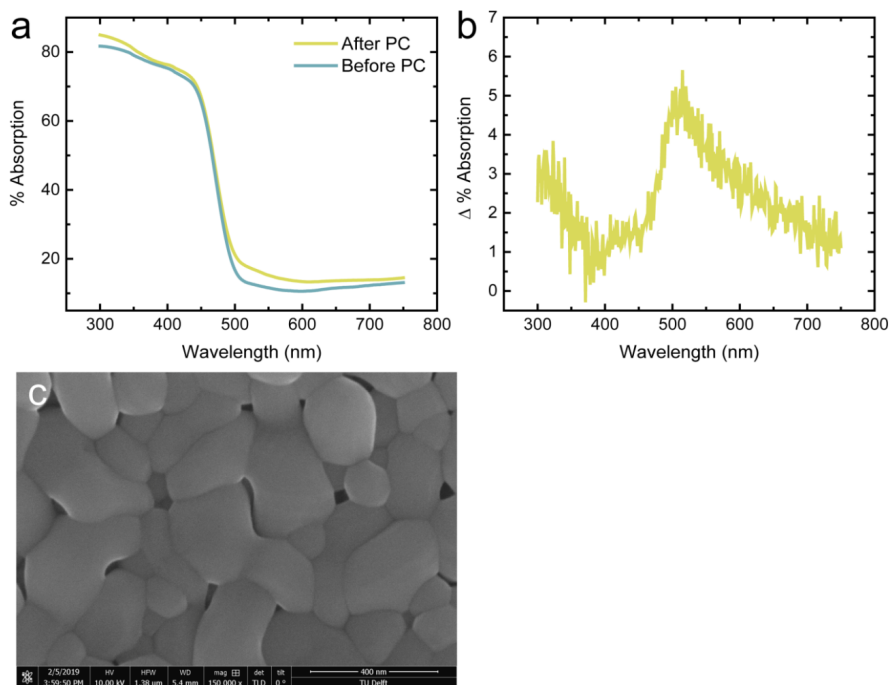
Supplementary Figure S4.3: (a) UV-vis absorption and (b) difference spectra of a before and after photocharging sample in phosphate buffer. After photocharging in phosphate buffer at pH 10, the PC sample also displays a plasmonic feature at 520 nm, indicating the optic response stems from the $BiVO_4$, rather than the electrolyte. (c) HR-SEM images of reference $BiVO_4$, not displaying surface roughnening. Scale bar is 400 nm.
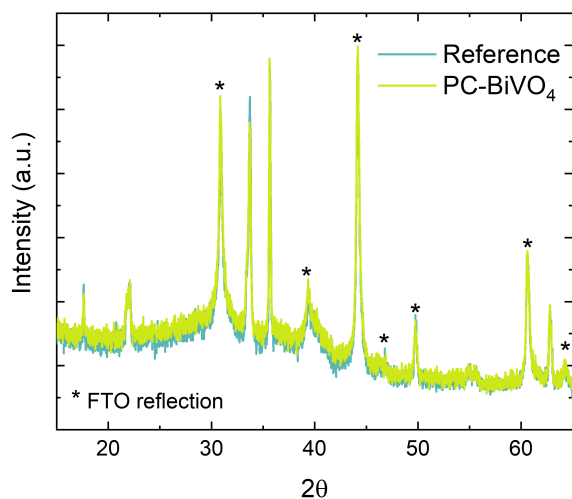
Supplementary Figure S4.4: X-ray diffraction patterns of a reference and PC-BiVO$_4$ sample. The peak at 17.5° 2θ only exists in monoclinic scheelite. Note that these XRD patterns were recorded using a cobalt (λ=1.7903 Å) radiaton source, changing the XRD pattern compared to more commonly used copper (λ=1.5406 Å) sources.
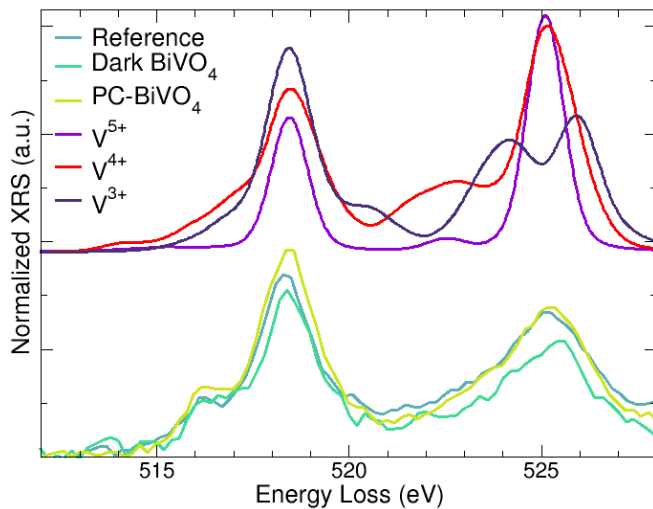
Supplementary Figure S4.5: A multiplet analysis of the vanadium L$_3$ and L$_2$ edge reveals the oxidation state of vanadium in the first 60 nm of BiVO$_4$ to be lower than +5. Arrows indicate trends: the L$_3$ increases in height and the L$_2$ edge decreases and broadens when the oxidation state decreases. Note: analysis was normalised with respect to E^0. Therefore the shift in energy as a function of oxidation state cannot be derived from the simulated spectra.

4
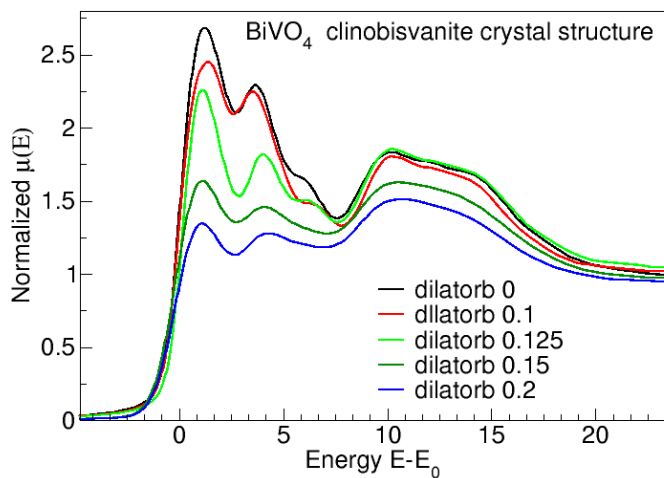
Supplementary Figure S4.6: The effect of increasing the dilatorb parameter on the BiVO$_4$ crystal structure.
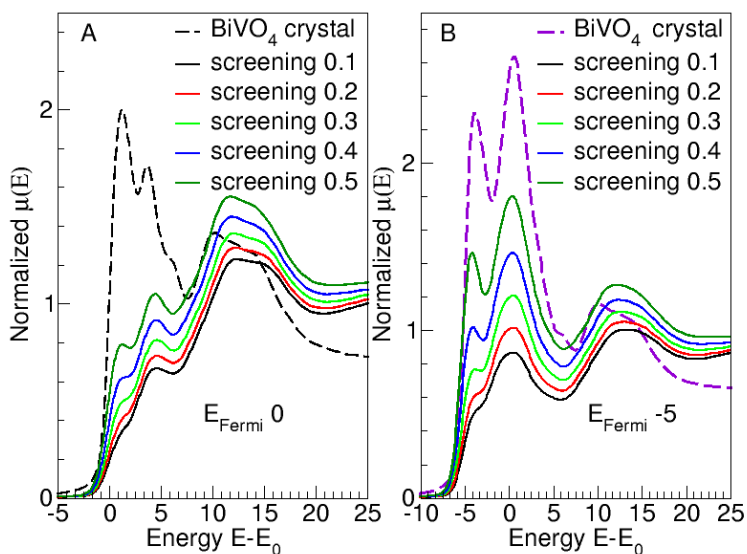
Supplementary Figure S4.7: Simulated O K edge spectra. The effect of changing the screening parameter on the BiVO$_4$ crystal structure for (a) a standard and (b) a 5 eV shifted Fermi level case.
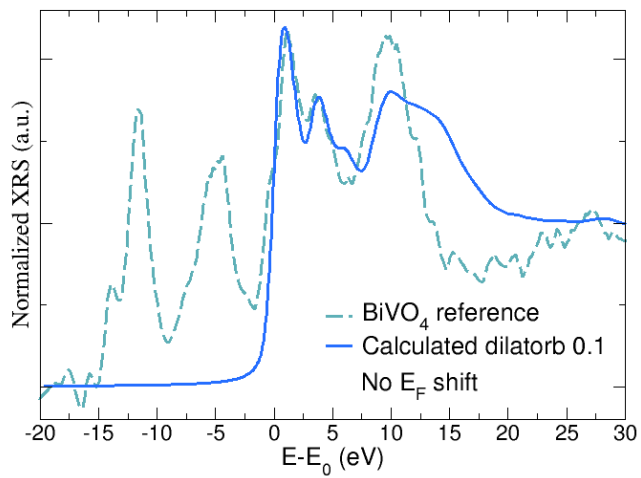
Supplementary Figure S4.8: Simulated O K edge spectra overlaid on XRS reference $BiVO_4$ spectrum. Reference $BiVO_4$ was simulated with a dilatorb value of 0.1, no screening parameter and no Fermi level shift.

4
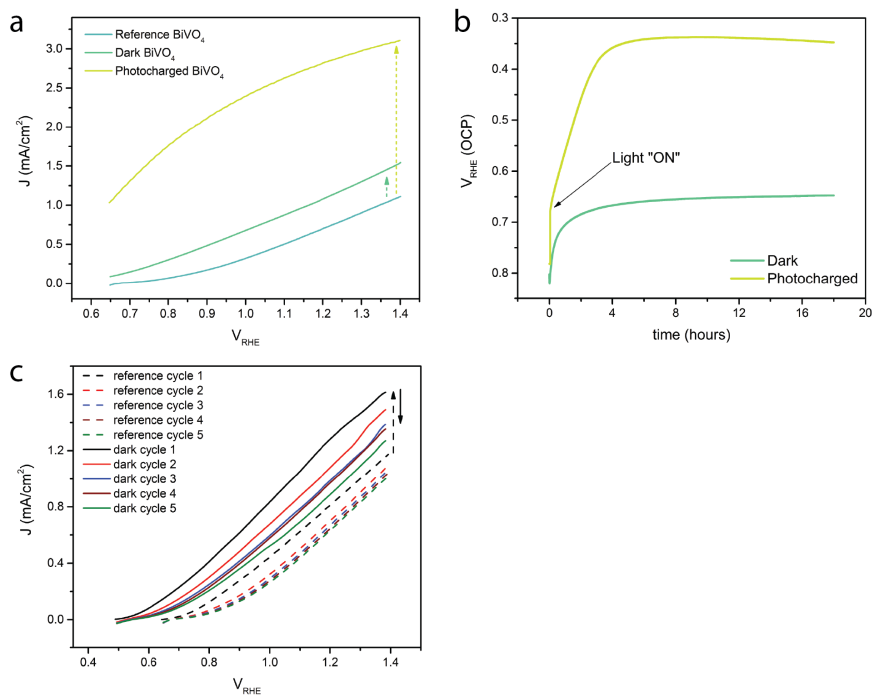
Supplementary Figure S4.9: (a) Plot showing the anodic scans of the CV's of the reference, dark and PC BiVO$_4$ (b) Improved performance of the BiVO$_4$ sample post dark treatment and the sudden decay of the performance once the surface adsorbed OH species is consumed for the water oxidation reaction.
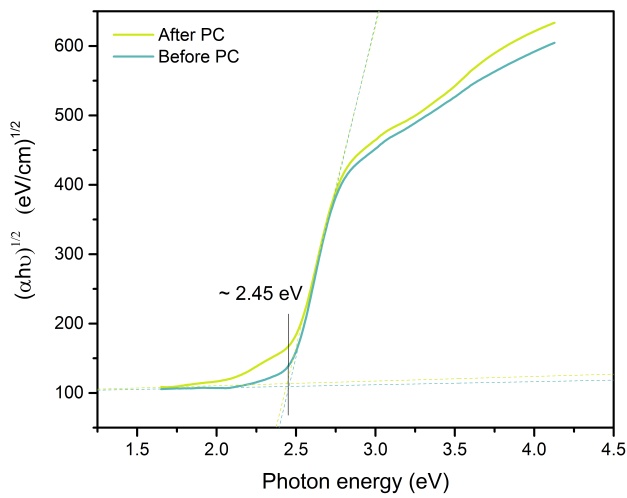
Supplementary Figure S4.10: Tauc plot of the absorbance spectra in Figure 4.2 (a) (of the main article).

The absorption coefficient (α) was calculated as per the equation,

$$\alpha = 2.303 A / t$$

where A is the absorbance and t is the thickness of the $BiVO_4$ sample. A thickness of 200 nm of the deposited $BiVO_4$ was used for the calculations. The absorbance was calculated from the measured transmittance (%T) data as per the equation,

$$A = 2 - log(\%T)$$

The bandgap of the $BiVO_4$ was determined using the relation presented by Tauc and Davis and Mott [45, 46],

$$(\alpha h\nu)^{1/n} \propto (h\nu - E_g)$$

Where n can take different values depending on the type of bandgap. $BiVO_4$ has an in-direct bandgap bandgap semicondutor [47] and hence n=2 was used to make the calculation in Figure S4.10. E_g in the above equation is the bandgap and is obtained by extrapoltion to the baseline, as in Figure S4.10.

FDMNES input file

! Fdmnes indata file
! Calculation for the O K edge in BiVO4
! Finite difference method calculation with convolution

Filout
./bvo4_cry_o_dlorb_0.2_sp_scr_0.1_new

Range   ! Energy range of calculation (eV)
-20. 0.2 -5 0.05 0. 0.1 5 0.2 10. .5 40. 1 80. ! first energy, step, intermediary energy, step ...,
last energy
Radius   ! Radius of the cluster where final state calculation is performed
8.0

   ! For a good calculation, this radius must be increased up to 6 or 7 Angstroms

! SCF

! R_self
! 7

! N_self
! 100

Green

! state_all

Edge
K

Z_absorber
8

Atom
83 1 6 1 3
23 2 3 2 3 4 0 2
8 2 2 0 2 2 1 4

Dilatorb
0 1 0.2

Screening
2 1 0.1

Spgroup
15:b1

Crystal
7.2532 11.702 5.096 90 134.234 90
1 0.0000 0.2500 0.6337
2 0.0000 0.2500 0.1352
3 0.1490 0.5060 0.2100
3 0.2580 0.3790 0.4510

!!!Convolution keyword : broadening with a width increasing versus energy as an arctangent
Estart
-20
Convolution
42 11 10
Gamma_hole
0.5
Gamma_fix
Gaussian
1.0
End

4.7. References

(1)   Firet, N. J.; Venugopal, A.; Blommaert, M. A.; Cavallari, C.; Sahle, C. J.; Longo, A.; Smith, W. A. *Chemistry of Materials* **2019**, *31*, 7453–7462.

(2)   Alexander, B. D.; Kulesza, P. J.; Rutkowska, I.; Solarska, R.; Augustynski, J. *Journal of Materials Chemistry* **2008**, *18*, 2298.

(3)   Han, H. S.; Shin, S.; Kim, D. H.; Park, I. J.; Kim, J. S.; Huang, P.-S.; Lee, J.-K.; Cho, I. S.; Zheng, X. *Energy & Environmental Science* **2018**, *11*, 1299–1306.

(4)   Abdi, F. F.; Han, L.; Smets, A. H. M.; Zeman, M.; Dam, B.; van de Krol, R. *Nature Communications* **2013**, *4*, 2195.

(5)   Sharp, I. D.; Cooper, J. K.; Toma, F. M.; Buonsanti, R. *ACS Energy Letters* **2017**, *2*, 139–150.

(6)   Pilli, S. K.; Furtak, T. E.; Brown, L. D.; Deutsch, T. G.; Turner, J. A.; Herring, A. M. *Energy & Environmental Science* **2011**, *4*, 5028.

(7)   Zhong, D. K.; Choi, S.; Gamelin, D. R. *Journal of the American Chemical Society* **2011**, *133*, 18370–18377.

(8)   Lee, D.; Kvit, A.; Choi, K.-S. *Chemistry of Materials* **2018**, *30*, 4704–4712.

(9)   Zachäus, C.; Abdi, F. F.; Peter, L. M.; van de Krol, R. *Chemical Science* **2017**, *8*, 3712–3719.

(10)   Trotochaud, L.; Mills, T. J.; Boettcher, S. W. *The Journal of Physical Chemistry Letters* **2013**, *4*, 931–935.

(11)   Trześniewski, B. J.; Smith, W. A. *Journal of Materials Chemistry A* **2016**, *4*, 2919–2926.

(12)   Trześniewski, B. J.; Digdaya, I. A.; Nagaki, T.; Ravishankar, S.; Herraiz-Cardona, I.; Vermaas, D. A.; Longo, A.; Gimenez, S.; Smith, W. A. *Energy & Environmental Science* **2017**, *10*, 1517–1529.

(13)   Liu, E. Y.; Thorne, J. E.; He, Y.; Wang, D. *ACS Applied Materials and Interfaces* **2017**, *9*, 22083–22087.

(14)   Breuhaus-Alvarez, A. G.; DiMeglio, J. L.; Cooper, J. J.; Lhermitte, C. R.; Bartlett, B. M. *The Journal of Physical Chemistry C* **2019**, *123*, 1142–1150.

(15)   Venugopal, A.; Smith, W. A. *Faraday Discussions* **2019**, *215*, 175–191.

(16)   Xie, J.; Yang, P.; Liang, X.; Xiong, J. *ACS Applied Energy Materials* **2018**, *1*, 2769–2775.

(17)   Deng, J.; Lv, X.; Zhong, J. *Journal of Physical Chemistry C* **2018**, *122*, 29268–29273.

(18)   Favaro, M.; Abdi, F. F.; Lamers, M.; Crumlin, E. J.; Liu, Z.; Van De Krol, R.; Starr, D. E. *Journal of Physical Chemistry B* **2018**, *122*, 801–809.

(19)   Abdi, F. F.; Firet, N.; van de Krol, R. *ChemCatChem* **2013**, *5*, 490–496.

(20)   Huotari, S.; Sahle, C. J.; Henriquet, C.; Al-Zein, A.; Martel, K.; Simonelli, L.; Verbeni, R.; Gonzalez, H.; Lagier, M.-C.; Ponchut, C.; Moretti Sala, M.; Krisch, M.; Monaco, G. *Journal of Synchrotron Radiation* **2017**, *24*, 521–530.

4

(21) Singh, S. P.; Karmakar, B. In *Bismuth: Characteristics, Production and Applications*; Materials Science and Technologies: NY: 2012; Chapter 9.

(22) Sahle, C. J.; Mirone, A.; Niskanen, J.; Inkinen, J.; Krisch, M.; Huotari, S. *Journal of Synchrotron Radiation* **2015**, *22*, 400–409.

(23) Joly, Y. *Physical Review B* **2001**, *63*, 125120.

(24) Joly, Y.; Cavallari, C.; Guda, S. A.; Sahle, C. J. *Journal of Chemical Theory and Computation* **2017**, *13*, 2172–2177.

(25) Retegan, M. Crispy, 2018.

(26) Oprea, B.; Radu, T.; Simon, S. *Journal of Non-Crystalline Solids* **2013**, *379*, 35–39.

(27) Bajaj, A.; Khanna, A.; Chen, B.; Longstaffe, J. G.; Zwanziger, U.-W.; Zwanziger, J.; Gómez, Y.; González, F. *Journal of Non-Crystalline Solids* **2009**, *355*, 45–53.

(28) Hermans, Y.; Murcia-López, S.; Klein, A.; van de Krol, R.; Andreu, T.; Morante, J. R.; Toupance, T.; Jaegermann, W. *Physical Chemistry Chemical Physics* **2019**, *21*, 5086–5096.

(29) Rini, M.; Cavalleri, A.; Schoenlein, R. W.; López, R.; Feldman, L. C.; Haglund, R. F.; Boatner, L. A.; Haynes, T. E. *Optics Letters* **2005**, *30*, 558.

(30) Schubert, W. K.; Wolf, E. L. *Physical Review B* **1979**, *20*, 1855–1862.

(31) Toudert, J.; Serna, R.; Jiménez de Castro, M. *The Journal of Physical Chemistry C* **2012**, *116*, 20530–20539.

(32) Wang, L.; Tsang, C.-S.; Liu, W.; Zhang, X.; Zhang, K.; Ha, E.; Kwok, W.-M.; Park, J. H.; Suk Lee, L. Y.; Wong, K.-Y. *Journal of Materials Chemistry A* **2019**, *7*, 221–227.

(33) Wang, S.; Chen, P.; Yun, J.-H.; Hu, Y.; Wang, L. *Angewandte Chemie* **2017**, *129*, 8620–8624.

(34) Jovic, V.; Laverock, J.; Rettie, A. J. E.; Zhou, J.-S.; Mullins, C. B.; Singh, V. R.; Lamoureux, B.; Wilson, D.; Su, T.-Y.; Jovic, B.; Bluhm, H.; Söhnel, T.; Smith, K. E. *Journal of Materials Chemistry A* **2015**, *3*, 23743–23753.

(35) Cooper, J. K.; Gul, S.; Toma, F. M.; Chen, L.; Glans, P.-A.; Guo, J.; Ager, J. W.; Yano, J.; Sharp, I. D. *Chemistry of Materials* **2014**, *26*, 5365–5373.

(36) Jovic, V.; Rettie, A. J. E.; Singh, V. R.; Zhou, J.; Lamoureux, B.; Buddie Mullins, C.; Bluhm, H.; Laverock, J.; Smith, K. E. *Physical Chemistry Chemical Physics* **2016**, *18*, 31958–31965.

(37) Zhao, Z.; Li, Z.; Zou, Z. *Physical Chemistry Chemical Physics* **2011**, *13*, 4746.

(38) Nie, K.; Kashtanov, S.; Wei, Y.; Liu, Y.-S.; Zhang, H.; Kapilashrami, M.; Ye, Y.; Glans, P.-A.; Zhong, J.; Vayssieres, L.; Sun, X.; Guo, J. *Nano Energy* **2018**, *53*, 483–491.

(39) Lin, X. W.; Wang, Y. Y.; Dravid, V. P.; Michalakos, P. M.; Kung, M. C. *Physical Review B* **1993**, *47*, 3477–3481.

(40) Rossell, M. D.; Agrawal, P.; Borgschulte, A.; Hébert, C.; Passerone, D.; Erni, R. *Chemistry of Materials* **2015**, *27*, 3593–3600.

(41) Tokunaga, S.; Kato, H.; Kudo, A. *Chemistry of Materials* **2001**, *13*, 4624–4628.

(42)   Joly, Y.; Cabaret, D.; Renevier, H.; Natoli, C. R. *Physical Review Letters* **1999**, *82*, 2398–2401.

(43)   Peter, L. M.; Gurudayal; Wong, L. H.; Abdi, F. F. *Journal of Electroanalytical Chemistry* **2018**, *819*, 447–458.

(44)   Van de Krol, R.; Grätzel, M., et al., *Photoelectrochemical hydrogen production*; New York: Springer: 2012.

(45)   Wood, D. L.; Tauc, J. *Physical Review B* **1972**, *5*, 3144–3151.

(46)   Davis, E. A.; Mott, N. F. *Philosophical Magazine* **1970**, *22*, 0903–0922.

(47)   Cooper, J. K.; Gul, S.; Toma, F. M.; Chen, L.; Liu, Y.-S.; Guo, J.; Ager, J. W.; Yano, J.; Sharp, I. D. *The Journal of Physical Chemistry C* **2015**, *119*, 2969–2974.

4

5

Light induced formation of a surface hetero-junction in photocharged CuWO$_4$ photoanodes

Photocharging has recently shown the ability to significantly improve the performance of several metal oxide photoanodes, similar to the enhancements achieved with co-catalysts and passivation overlayers. Herein, we demonstrate the effect of photocharging on CuWO$_4$ photoanodes for the first time, with prolonged AM 1.5 illumination under open circuit conditions. The photocharging treatment on CuWO$_4$ samples doubled the photocurrent obtained at 1.23 V$_{RHE}$. This enhancement is attributed to the light induced formation of a surface bound copper complex with the solution anion species in the electrolyte. This thin semiconducting copper borate layer forms a hetero-junction with the CuWO$_4$, improving the charge separation near the surface and thus suppressing the recombination of charge carriers in the space charge region. The striking similarities in photocharging of different metal oxide semiconductors highlights that the metal oxide semiconductor - electrolyte interface is more complex than previously understood. The formation of this time-dependent light induced surface layer should therefore be considered in all experimental studies on photo-electrochemistry with metal oxide semiconductor photoanodes.

5.1. Introduction

A shift to a renewable energy based society is necessary to contain or limit the catastrophic effects of global climate change.[2] Producing electricity from renewable energy sources could be a way to tackle this problem, but this transition is currently facing a roadblock in dealing with the intermittency of these resources. Current energy storage techniques are not sufficient to tackle the discrepancy between the energy demand and energy production timelines. The viability of a tera-watt scale renewable energy society will need this intermittency problem to be dealt with. One way to address this challenge is to (photo-)electrochemically produce commercially valuable chemicals or fuels, that have a good market demand, from the excess renewable electricity. This way the economics of the technology can be balanced, making it self-sustainable and attracting further investments and expansions. (Photo-)electrochemical pathways to produce valuable chemicals such as hydrogen from earth abundant raw materials, i.e. water, is one such way to do so.[3]

(Photo-)electrochemical water oxidation is an important (half-)reaction of interest within electrochemistry, as it acts as a proton source for more valuable electrochemical (half-)reactions such as hydrogen evolution, CO_2 reduction and ammonia synthesis. Metal oxides have received significant attention in the past as a prospective photoanode material due to their suitable opto-electronic properties, higher stability compared to low bandgap semiconductors and their raw material abundance. However, these metal oxide photoanodes have been severely underperforming, majorly as a result of the complexity involving the multi-electron ($4e^-/4h^+$) oxygen evolution reaction and the existence of different loss mechanisms such as bulk recombination and surface recombination of photo-generated charge carriers at the semiconductor|electrolyte interface (SEI). The latter issue could be dealt with, to an extent, with the addition of catalytic and passivating overlayers such as Co-Pi.[4, 5] Unfortunately, these overlayers often result in parasitic light absorption that decrease the overall performance of the composite device. [6]

Recently, the "photocharging" process was introduced as a way to suppress the losses at the SEI of several metal oxide photoanodes ($BiVO_4$, Fe_2O_3, WO_3) without the addition of an overlayer, resulting in an improvement in the overall performance.[7–12] This photocharging treatment lead to an increase in the photocurrent and an appreciable cathodic shift in the onset potential in some cases. This was first demonstrated in bismuth vanadate by Trześniewski et al. [11], improving the performance of $BiVO_4$ tremendously and making its performance comparable to that of $BiVO_4$ with catalytic over layers. This photocharging treatment was performed by illuminating the metal oxide semiconductor for a prolonged time under open circuit conditions in a phosphate buffer electrolyte. Li et al. [8] also demonstrated a similar effect on tungsten doped $BiVO_4$, by prolonged illumination of the W:$BiVO_4$ concentration in the electrolyte on the degree of suppression of the losses at the SEI, i.e. at more alkaline conditions the photo-charging treatment worked better. Liu Y. E. et al. [10] made use of intensity modulated photoelectron spectroscopy (IMPS) to quantitatively study the kinetics of the photocharged $BiVO_4$ and show that the enhancement from photocharging is both in the bulk and the surface of

the $BiVO_4$ photoanode. Favaro et al. [7] used in-situ HAXPES to demonstrate that the light induced suppression of surface losses resulting from the photocharging process in $BiVO_4$, in a phosphate buffer solution, could be a result of the formation of a thin $BiPO_4$ overlayer as a result of the illumination. Li et al. [9] further demonstrated the effect of the UV curing process on WO_3 photoanodes, showing that this light induced performance enhancement was not confined to only $BiVO_4$. Xie et al.[12] recently demonstrated a similar enhancement on titanium doped hematite photoanodes, by photocharging the $Ti:Fe_2O_3$ with prolonged illumination under an applied anodic potential.

Copper tungstate ($CuWO_4$) is another n-type metal oxide semiconductor that has been extensively researched for photo-electrochemical water oxidation.[13–18] The band-gap energy of ~ 2.25 eV allows it to achieve a theoretical photocurrent density upwards of 10 mA/cm^2.[13] The ability of $CuWO_4$ photoanodes to selectively oxidize water over chloride ions in the solution is also an added advantage, opening possibilities for direct water oxidation from sea water.[18] Herein, we demonstrate that copper tungstate also shows an improvement in performance with the photocharging treatment. We show that this photocharging process of $CuWO_4$ results in doubling of the photocurrent of the untreated sample at 1.23 V_{RHE}, with only a negligible anodic shift in the onset potential. We also show that this effect is reversible under dark conditions, as also seen with $BiVO_4$. More importantly, these results raise the question if the photocharging treatment is universal to all metal oxide semiconductors, and what the implications of this treatment may hold for general SEI's. Gaining more fundamental understanding of the photocharging process will help to gain more insight into the dynamic behaviour of the metal oxide SEI under illumination. In this article, we would like to briefly discuss the features of the photocharging process of $CuWO_4$ and the similarities with the photocharging process of other metal oxide semiconductors. We highlight that the metal oxide semiconductor – electrolyte interface is much more complex than what is previously understood.

5.2. Materials and methods

Preparation of $CuWO_4$ thin films

$CuWO_4$ thin films of ~ 1.2 μm were deposited onto a conductive FTO coated glass substrate (TEC-15, Hartford glass co.) by the spray pyrolysis technique. The precursor solution was prepared by mixing equimolar aqueous solutions of $CuSO_4.5H_2O$ (99.995% trace metal basis , Sigma Aldrich) and $Na_2WO_4.2H_2O$ (BioUltra, >= 99.0% (T), Sigma Aldrich), resulting in the precipitation of $CuWO_4$. The solution was further diluted with MilliQ water to make the concentrations of Cu^{2+} and W^{6+} at 0.01 M in the final precursor solution. The $CuWO_4$ precipitate was dissolved using 25% aqueous NH_3 solution (Ammonium hydroxide solution, puriss. P.a., reag. ISO, reag. Ph. Eur., >=25% NH_3 basis, Sigma Aldrich) and the final pH of the precursor solution was made up to 11.5. The FTO substrate was cleaned with laboratory grade soap solution followed by MilliQ water, acetone and isopropanol and eventually dried off using nitrogen gas. This was followed by a 45 minute UV/Ozone cleaning step at 60 °C (Novascan UV Ozone cleaner – PSD Pro series). The cleaned substrate was placed on a ceramic heating plate and the plate was

slowly heated to 300 °C. The spray deposition was carried out using an automated spray setup, spraying at 1 minute cycles with 1 second spray and 59 seconds delay time, for 100 cycles driven by an overpressure of 0.8 MPa of nitrogen gas. The nozzle substrate distance was fixed at 40 cm and the precursor solution was placed 33 cm below the nozzle and was fed via the siphoning effect of the nitrogen flow. After the deposition, the samples were annealed in a tube oven at 500 °C for 5 hours at a ramp rate of 5 °C/min with an airflow of 80 cm^3/min.

Photoelectrochemical measurements

The $CuWO_4$ photoanodes were photoelectrochemically tested using a potentiostat (VersaSTAT 3, Princeton Applied Research) in a three electrode arrangement, with a coiled platinum wire as the counter electrode and an Ag/AgCl (XR300, saturated KCl and AgCl solution, Radiometer Analytical) reference electrode. The electrolyte used was an aqueous 0.3 M borate buffer (99.97% trace metal basis Boric acid, Sigma Aldrich) with 0.1 M sodium perchlorate (ACS reagent, >= 98.0%, Sigma Aldrich) and the pH of this solution was corrected to 7.5 using a concentrated NaOH (pellets, >= 98% Assay, Baker analysed ACS, J.T. Baker, Avantor performance materials) solution. The voltammetric scans were performed at a scan rate of 50 mV/s unless specified otherwise. A Newport Sol3A Class AAA (type 94023A-SR3) solar simulator, with a 450 W Xenon short arc lamp, was used to provide the simulated solar illumination for the photocurrent measurements at the standard AM1.5 illumination intensity (100 mW/cm^2). The samples were illuminated in the back illumination mode. The electrolyte inside the photoelectrochemical cell was constantly stirred using a magnetic stirrer and was purged with nitrogen gas to constantly remove any dissolved gasses in the electrolyte. The incident photon to current efficiency (IPCE) measurements were performed using a 200 W quartz-tungsten halogen lamp coupled with a grating monochromator (Acton SpectraPro 150i) and electronic shutter system (Uniblitz LS6). The illumination intensities of the tungsten halogen lamp were measured using a Newport high performance handheld optical power meter (1919-R) coupled with a UV-enhanced silicon photodetector (918-UV-OD3R). The IPCE measurements were performed at an applied potential of 1.23 V_{RHE}. The $CuWO_4$ photoanodes were photocharged by illuminating the sample (with AM1.5 light) in a photoelectrochemical cell under open-circuit conditions, for prolonged hours. The catalytic efficiency of the $CuWO_4$ photoanodes was tested using methanol as a hole scavenger, by mixing it with the electrolyte used for the voltammetry measurements in a 50% v/v ratio. Using this experiment, we probe the photocurrent generated in the presence of a hole scavenging electrolyte, which assumes near unity transfer of holes to oxidize a compound that is more easily oxidized than water, and use the ratio of these photocurrents to estimate the 'ideal' hole transfer rate if it drives a reaction that does not have a major rate limiting step. Mott-Schottky plots were obtained for the $CuWO_4$ samples in the dark, in the fixed frequency mode (10 kHz) with a 15 mV amplitude of perturbation. These measurements were performed without any stirring or nitrogen bubbling.

Material Characterization

UV-Vis absorption measurements of the $CuWO_4$ samples were obtained using a Perkin Elmer Lambda 900 UV/Vis/NIR spectrometer. The measurements were performed inside an integration sphere, in transmittance mode (%T), with a sample tilt of 15 degrees

to minimize reflection of the incident beam from the sample. The transmittance data was converted to absorption data (%A) using the formula %A = 100 - %T. The measurements were performed between 750 nm and 300 nm, at a scan rate of 250 nm/min with an integration time of 0.2 sec. Absorption coefficient and Tauc plot were calculated from the above obtained transmittance data.

X-ray Diffraction (XRD) measurements were performed using a Bruker D8 Advance diffractometer powered with a Co Kα X-ray source (I = 1.78897 Å). The samples were scanned at a scan speed of 0.4 seconds per step, with each step being 0.02 degrees, with no rotation. Scanning electron microscope (SEM) images to study the surface morphology of the $CuWO_4$ samples were obtained using a Joel JSM-6010LA analytical SEM machine. The measurements were performed at a working distance of ~ 10 mm at an accelerating voltage of 5 kV.

X-ray photoelectron spectroscopy (XPS) measurements were performed using a Thermo Scientific Kα XPS system with an Aluminium Kα X-ray source. The measurements were performed with a spot size of 400 μm, pass energy of 50 eV, energy step size of 0.1 eV and a dwell time of 50 ms, along with a flood gun for charge compensation. 10 scans were performed for each of C1s, O1s, W4f, 300 scans for B1s, 50 scans for the valence band and 25 scans were performed for the Cu2p, around their respective binding energies, to obtain the final spectrum. The valence band scans were performed at a pass energy of 100 eV. Measurements were performed for three different spots in each sample and the data was averaged over these three spots, expect for B1s, where the data was averaged over two different spots. All data presented in this work are corrected for the C1s peak shifts, using 284.8 eV as the reference point for the C1s peaks. The data presented in the paper is after background subtraction. A U2 Tougaard background spectra with a C parameter of -3450 was used in each case. Samples were rinsed with MilliQ and dried under N_2 stream, to remove any salt deposits at the surface, before loading to the XPS system.

5.3. Results

Voltammetric scans were performed to evaluate the photoelectrochemical performance of untreated (UT) and photocharged (PC) $CuWO_4$ substrates. The potential sweeps were performed between 0 V vs open-circuit potential (OCP) and 1.4 V_{RHE} to obtain the current–voltage plots. Figure 1 shows the measured photocurrent density of the UT-$CuWO_4$ samples (solid blue line) against the applied potential. A photocurrent density of   30 $\mu A/cm^2$ was measured at 1.23 V_{RHE} for the UT-$CuWO_4$ sample, with an onset potential of   0.7 V_{RHE}. The lower slope at potentials less than 0.9 V_{RHE}, compared to the slope of the curve above this potential, would suggest that there could be other non-faradaic processes occurring apart from water oxidation at these low potentials. In fact, similar observations were made in other reports on $CuWO_4$ [13] and WO_3 [19, 20], where they attribute it to the de-intercalation of protons or alkali cations from the $CuWO_4$ or WO_3 lattice. After analysing the properties of the UT - $CuWO_4$, these samples were then subjected to the photocharging treatment for 15 hours. Figure 5.1 (a) also shows the im-

provement in the photocurrent of the PC-CuWO$_4$ sample (solid green line), compared to the untreated sample (solid blue line). The photocurrent at 1.23 V$_{RHE}$ of the photocharged sample is atmost two times that of the untreated sample, with only a negligible anodic shift in the onset potential. The increase in photocurrent after the photocharging treatment may be a result of light induced - surface passivation, improvement in the kinetics or catalytic properties, improvement in the bulk charge transport or charge separation properties or a combination of some or all of these factors. The latter was true in the case of BiVO$_4$, where a comprehensive set of investigations has been performed since the discovery of this photocharging effect.[7, 8, 10, 11, 21] The evolution of photocurrent with the photocharging time is shown in Figure S5.1.
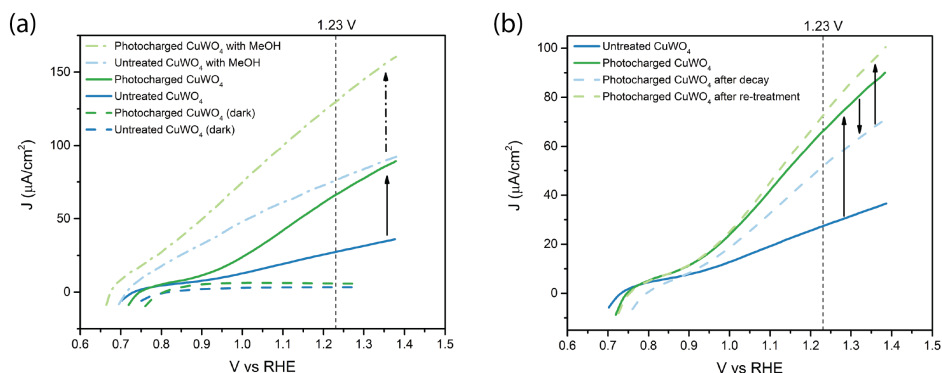
Figure 5.1: (a) Voltammetric scans (in light and dark) of UT and PC – CuWO$_4$ in the back illumination mode. Measurements were performed with and without hole scavenger. (b) Voltammetric scans demonstrating the decay and re-photocharging of the PC – CuWO$_4$ substrates.

To get a better understanding of the reason behind the improvement in performance of the CuWO$_4$ samples from photocharging, a hole scavenger was used before and after photocharging and the results were compared to the case without a hole scavenger. Hole scavengers have a much lower theoretical redox potential and, as a result, can be more easily oxidized than water. The catalytic efficiency in the presence of such hole scavengers is assumed to be near 100%, with a complete suppression of all surface losses. Methanol, which is typically used as a hole scavenger in photoelectrochemical studies [22], was used in a 50% v/v ratio with the aqueous electrolyte to perform the voltammetric scans. Figure 5.1 (a) also shows the improvement in performance of the UT and PC - CuWO$_4$ sample, when a hole scavenger is used (dash dot light blue and light green lines, respectively). The performance of the UT-CuWO$_4$ improved when a hole scavenger is used (dash dot light blue line), as expected. This result suggests that the UT-CuWO$_4$ was suffering from surface recombination losses and/or poor water oxidation kinetics. Comparing the performance of UT-CuWO$_4$ with hole scavenger and that of PC-CuWO$_4$ without the hole scavenger suggests that the improvement in performance of PC-CuWO$_4$ sample could be a result of improvement in catalytic efficiency. Interestingly, the PC-

$CuWO_4$ samples also showed an improvement (dash dot light green line) in photocurrent density across a large potential range when the hole scavenger was used. If the performance enhancement of $CuWO_4$ due to photocharging was purely due to improvement in catalytic efficiency or suppression of surface recombination losses, the performance of UT and PC-$CuWO_4$ with hole scavenger would have been similar. Therefore, the improvement in performance of PC-$CuWO_4$ compared to UT-$CuWO_4$ in presence of hole scavenger suggests that there is a "bulk" component in the performance enhancement due to the photocharging effect, similar to what was found for $BiVO_4$.[10]

The improvement in performance of the PC-$CuWO_4$ was also seen to be reversible under dark conditions. Herein, the sample was first photocharged for 15 hours and then left in the electrolyte under dark OCP conditions for 5 hours. The performance of this "discharged" sample was further evaluated with another voltammetric scan, as seen in Figure 5.1 (b) (dashed blue line). The sample has indeed discharged, as evident from the decrease in the measured photocurrent. However, the performance of this decayed sample was still better than the untreated $CuWO_4$ sample (solid blue line), suggesting a slow decay process or a permanent modification of the $CuWO_4$ sample. This decaying of the photocharging effect was also seen in $BiVO_4$ by Trześniewski et al. [11], albeit at a much faster rate at a similar pH, suggesting that there are some similarities and some differences in the mechanism(s) for the photocharging effect in these two materials. The decayed $CuWO_4$ samples could also be re-photocharged in a similar fashion (dashed green line).

To try and understand if this "bulk" component in performance enhancement after photocharging is related to the improvement in optical characteristics of $CuWO_4$, the absorption spectra of $CuWO_4$ before and after photocharging were measured. As seen in Figure 5.2 (a), the as deposited - $CuWO_4$ samples had an absorption onset of ~ 550nm, with a slow increase in the absorption between 550 nm and 420 nm. This characteristic is attributed to an indirect bandgap within $CuWO_4$, which is also seen with some other metal oxide semiconductors. [23] The other characteristic feature in this figure is the absorption above 700 nm. This is attributed to the d-d transitions in copper due to the Jahn-Teller distortion in the copper octahedra (CuO_6) when copper exists in Cu^{2+} state, as in the case of $CuWO_4$.[24, 25] The absorption spectra of the PC-$CuWO_4$ was also measured in a similar fashion and the absorption within the bandgap was seen to be unchanged. Interestingly, the absorption close to the bandgap onset and above the bandgap decreased after the photocharging treatment. This above bandgap absorption could a result of the combination of multiple factors. One possibility is the change in the absorption onset of the d-d transitions in the Cu 3d orbital. Another is the stray reflection of the incoming light beam during the transmittance measurements, from the complex morphology of the spray deposited $CuWO_4$, while the change in the absorption from any mid-bandgap states originating from the defects within the material may also play a role. To see if this decrease in absorption is related to a change in the optical properties of the material due to the photocharging effect, a Tauc plot was constructed from the absorption data collected before and after photocharging. As seen in Figure 5.2 (b), the bandgap of the as-deposited and photocharged $CuWO_4$ remained the same at 2.25

eV, similar to other reports in literature.[13, 17]
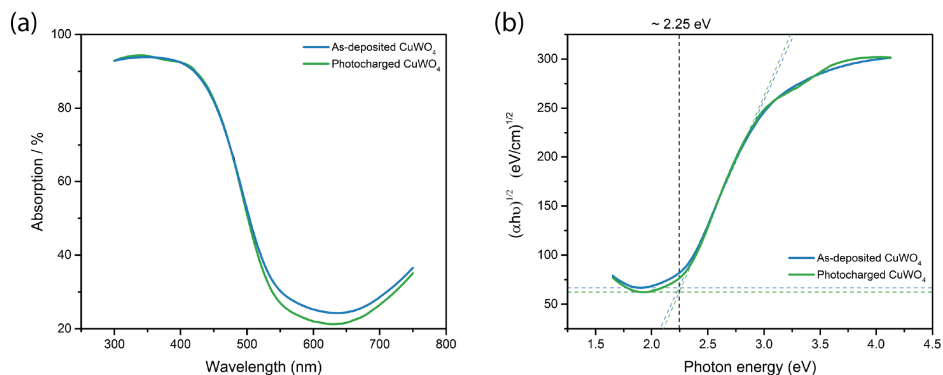
Figure 5.2: (a) Absorption spectra of as-deposited and photocharged CuWO$_4$ (b) Tauc plot constructed from the absorption data for the as-deposited and photocharged CuWO$_4$
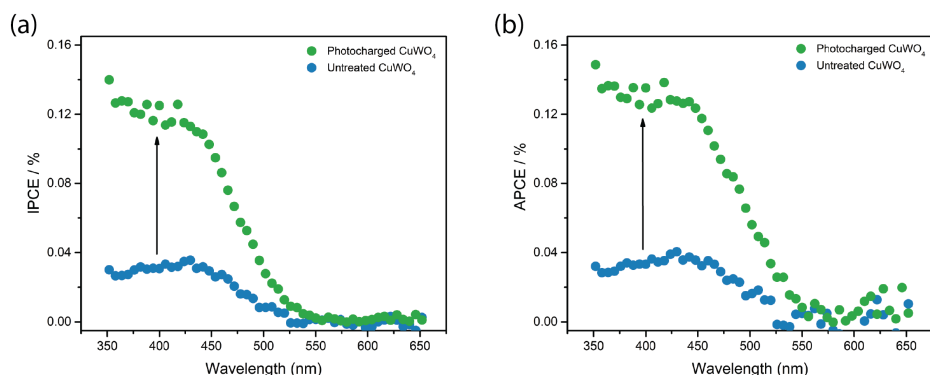
Figure 5.3: (a) Incident photon to current efficiency (IPCE) of the UT and PC – CuWO$_4$ substrates (b) Absorbed photo to current efficiency (APCE) of the UT and PC – CuWO$_4$.

Incident photon to current efficiency (IPCE) measurements were performed on the UT and PC - CuWO$_4$ to determine if this change in absorption at the onset and above the bandgap has altered the wavelength dependent quantum efficiency of CuWO$_4$ due to the photocharging treatment. Figure 5.3 (a) shows the IPCE of UT and PC - CuWO$_4$ plotted against the wavelength of the incoming photons. Both the UT and PC – CuWO$_4$ had a similar onset of the photocurrent, at ~ 550 nm, suggesting that the change in the absorption near the bandgap onset and above bandgap does not contribute to the improved performance due to photocharging. The quantum efficiency within the bandgap improved significantly post photocharging. To understand this improvement, the IPCE

data was corrected for the absorption to obtain the absorbed photon to current efficiency (APCE). The APCE reflects the losses due to recombination of the photo-generated carriers within the semiconductor. The APCE, in Figure 5.3 (b), has also shown a similar enhancement due to photocharging of $CuWO_4$, suggesting that the photocharging treatment has resulted in the suppression of recombination losses within the semiconductor.
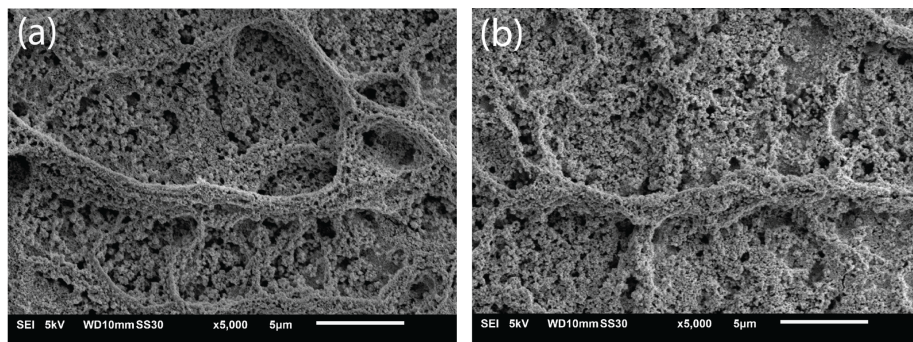
Figure 5.4: (a) SEM image of UT – $CuWO_4$ sample (b) SEM image of PC – $CuWO_4$ sample.

To investigate if the improvement in performance due to photocharging is a result of some photo-induced morphology change, as suggested in some reports[8, 9], the morphology of UT and PC – $CuWO_4$ was analysed using scanning electron microscopy (SEM). Figure 5.4 (a) and (b) shows the surface morphologies of the UT-$CuWO_4$ and PC-$CuWO_4$ respectively. The UT-$CuWO_4$ samples were left in the electrolyte under open circuit conditions for 16 hours without any illumination, whereas the PC-$CuWO_4$ samples were illuminated under the same conditions. A nanoporous surface with an extensive microstructure network is clearly visible in both these images, indicating that the surface has remained mostly intact after the photocharging treatment. This is also shown in figure S5.2 (a-b). To further confirm if the photocharging treatment has led to the formation of any additional active sites at the surface, the electrochemical active surface area (ECSA) of the UT and PC-$CuWO_4$ was determined by performing cyclic voltammetry scans in the dark, at a series of different scan rates for each of these samples. The double layer capacitance (C_{dl}), obtained from the slope of the current density versus scan rate plot, can be directly correlated to the ECSA. In Figure 5.5 (a), the similar C_{dl} values indicate that there is no major change in the number of active sites in the UT and PC – $CuWO_4$ samples. The small change in the obtained C_{dl} values could be a result of the error margin in these fitting techniques.

The bulk crystal structure of the UT and PC - $CuWO_4$ were also analysed with the X-ray diffraction technique. Figure 5.5 (b) shows the XRD spectra for both the untreated and the photocharged samples. Sharp peaks corresponding to $CuWO_4$ (positions marked in red), agreeing with other reports in literature [13, 17], indicate a very crystalline thin film of $CuWO_4$. More importantly, no shift in peak positions or a significant increase in the peak intensities were visible after the photocharging treatment, suggesting that the

(a)

(b)
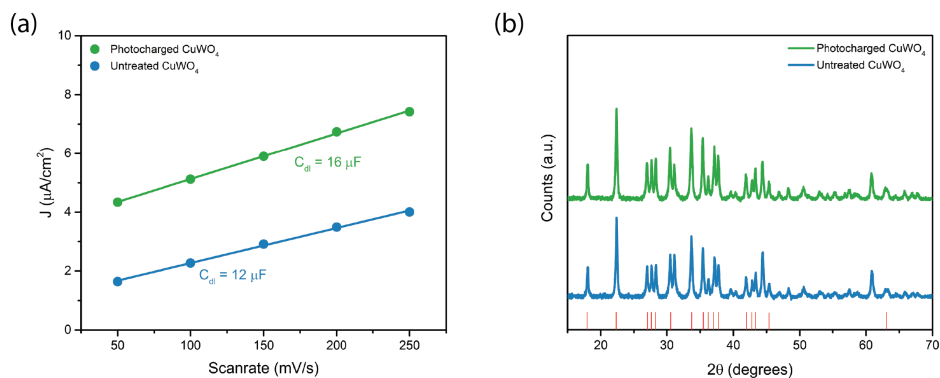
Figure 5.5: (a) Electrochemically active surface area (ECSA) plot for UT and PC – $CuWO_4$, obtained at 1.3 VRHE from performing cyclic voltammetries at different scanrates in the dark (b) X-ray diffractograms of UT and PC –$CuWO_4$.

bulk structure has remained unchanged after the photocharging treatment. This is also consistent with the reports on photocharging of $BiVO_4$.[8, 11]

To investigate if the chemical composition of the surface has been altered due to the photocharging treatment, the surface composition of the UT and PC – $CuWO_4$ were analysed using X-ray photoelectron spectroscopy (XPS). Figure 5.6 (a – c) shows the narrow spectra of the Cu 2p, O 1s and B 1s species. The W 4f narrow spectra is shown in figure S5.3 (a). Cu 2p peaks have a signature of four distinct features, when the Cu exists in the Cu^{2+} state.[26, 27] The Cu^{2+} satellite peaks (as marked in the figure) are a result of the shake-up transitions in the valence band of copper, due to the photoejection of a core electron.[28] The characteristic Cu $2p_{3/2}$ peaks for Cu(I)O, Cu(II)O and Cu(II) hydroxide are at 932.18 ± 0.12 eV, 933.76 ± 0.11 eV and 934.67 ± 0.02 eV, respectively [29] and their associated Cu $2p_{5/2}$ peaks around 955 eV. The Cu2p spectra in Figure 5.6 (a) consists of copper in Cu(I), Cu(II) and Cu(II) hydroxide forms for both the UT and PC –$CuWO_4$, as evidenced by the complex spectra with peaks between 930 and 940 eV, resulting from the convolution of signals from copper in different forms. Interestingly, the peaks at ~ 932 eV and ~ 952 eV diminished after photocharging, which is attributed to Cu^+, possibly suggesting that the concentration of Cu^+ species at the surface has decreased near the semiconductor-electrolyte interface after photocharging. Similarly, the W4f and O1s spectra were also analysed for the UT and PC – $CuWO_4$. The W $4f_{7/2}$ has a characteristic peak at 35.8 ± 0.4 eV, when the tungsten is in the +6 oxidation state [29], with the W $4f_{5/2}$ doublet peak at ~ 37.9 ± 0.4 eV. A W $5p_{3/2}$ peak is also normally visible at ~ 40.8 eV.[29] The associated lattice oxygen (O 1s) would have a peak at 530.5 ± 0.2 eV (28). The O 1s peaks could also have a shoulder at higher binding energies. This shoulder peak at ~ 532 eV is a characteristic of oxygen in the chemisorbed species at the surface.[7, 11] All these characteristic peaks for W 4f and O 1s are visible in Figure S5.3 (a) and Figure 5.6 (b) for both UT and PC – $CuWO_4$. The shoulder peak in the O 1s spectra has become
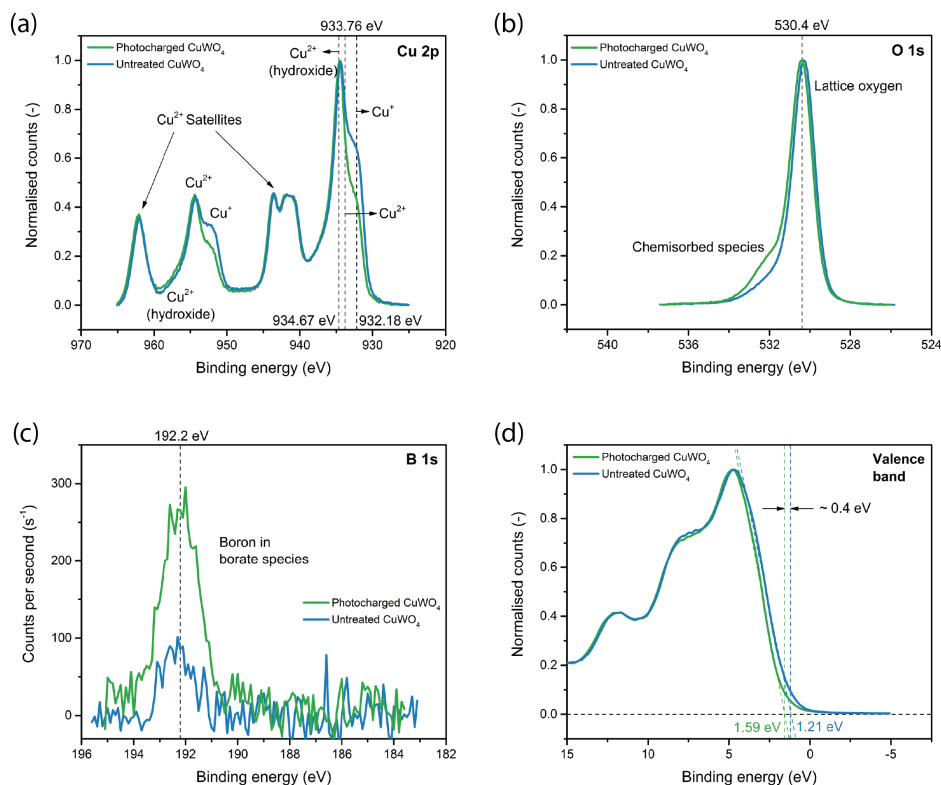
Figure 5.6: XPS spectra of (a) Cu 2p, (b) O1s, (c) B1s and (d) Valence band of UT and PC – CuWO$_4$.

more prominent post photocharging, possibly due to the build-up of oxygen in some chemisorbed species during photocharging. Both the O 1s and W 4f spectra also seem to have a minor shift of ~ 0.1 eV to higher binding energies post photocharging. B 1s spectra was also recorded for both UT and PC – CuWO$_4$. B 1s has a peak at ~ 192.2 eV for boron in a borate species.[30, 31] This peak is clearly visible in Figure 5.6 (c) for the PC – CuWO$_4$ sample and less so for the UT – CuWO$_4$. A noisy spectrum even after performing 300 scans indicate that the concentration of this boron species at the surface is low. This data was presented without normalisation due to this low signal to noise ratio. The valence band spectra of the UT and PC – CuWO$_4$ were measured in a similar fashion, shown in Figure 5.6 (d). The spectra of the UT and PC – CuWO$_4$ seem to be similar, except for a noticeable shift of valence band maximum (VBM) to higher binding energies (by ~ 0.4 eV) for the photocharged sample. The complete valence band spectra is shown in Figure S5.3 (b).

To determine if the band edge positions have been altered due to photocharging, Mott-Schottky plots were gathered for the UT and PC – CuWO$_4$ samples. Additionally,
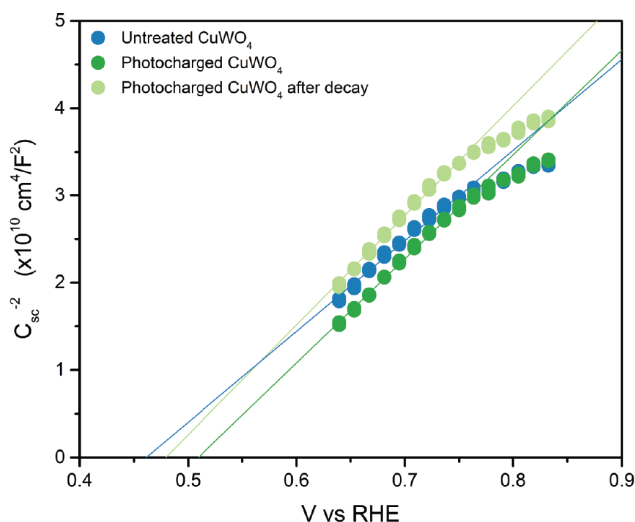
Figure 5.7: Mott-Schottky plots of UT-, PC- and discharged CuWO$_4$ samples obtained in the fixed frequency mode in the dark.

the Mott-Schottky plots were also obtained for the PC – CuWO$_4$ after discharging in the dark OCP conditions, as shown in Figure 5.7. The Mott-Schottky plots can be used to determine the flat band potential and the charge carrier densities of CuWO$_4$. The flatband potential can be estimated from the x-intercept of the linear fit to the C$_{sc}^{-2}$ vs potential plot, while the slope of this linear fit is inversely proportional to the charge carrier density. All three, the UT and PC – CuWO$_4$ and the discharged sample, had a similar x-intercept of ∼ 0.5 V$_{RHE}$ and similar slopes. This flatband potential value agrees with other reports on spray deposited CuWO$_4$.[14] The small difference, < 50 mV, in the x-intercept values could be a factor of the accuracy of the Mott-Schottky method and would fall within the error margin.

5.4. Discussion

The photocharging treatment has clearly improved the performance of CuWO$_4$ post photocharging. This was confirmed by both the cyclic voltammetry scans and the IPCE experiments for the UT and PC – CuWO$_4$. The catalytic efficiency of UT and PC – CuWO$_4$ was calculated according to the method suggested by Dotan et al. [32] A clear bump in the low potential region of the catalytic efficiency plot (Figure S5.4 (a)) confirms the deintercalation of H$^+$ and Na$^+$ from CuWO$_4$ lattice [13, 17], as suggested before. The hole scavenger experiments suggested a "bulk" enhancement factor from the photocharging effect, together with any surface enhancement. This bulk enhancement post photocharging could a be a result of multiple factors; (1) improved light absorption (2) mor-

phological changes or (3) improved charge separation in the space charge region. A series of characterisation techniques were performed to better understand this potential bulk enhancement. Absorption spectra of the UT and PC - $CuWO_4$ showed no major difference within the bandgap. This was confirmed from the Tauc plot which showed a bandgap of ~ 2.25 eV for both the UT and PC - $CuWO_4$. In fact, the IPCE plots also had a similar onset for both the UT and PC - $CuWO_4$. SEM images of the UT and PC - $CuWO_4$ also didn't show any major difference, with both the mirco and nanostructures remaining intact after the photocharging treatment. This was also confirmed by the ECSA plots, which provided similar double layer capacitance for both the UT and PC - $CuWO_4$. The XRD data also revealed that the bulk of the $CuWO_4$ remained unchanged post photocharging. The information obtained from the absorption spectra, IPCE plots, SEM images, ECSA experiments and XRD patterns suggest that the bulk enhancement is not a result of any morphological change or improved light absorption due to the photocharging effect, rather, could due to an improved charge separation in the space charge region post photocharging. To verify this, the charge separation efficiency was also calculated as per the method recommended by Dotan et al. [32], as in Figure S5.4 (b). This plot confirms the increase in charge separation efficiency post photocharging.

The chemical composition of the surface of UT and PC – $CuWO_4$ was analysed using XPS. The data suggested that the surface composition of copper has changed after photocharging. Specifically, there was a decrease in the concentration of Cu^+ at the surface for the PC – $CuWO_4$ samples. Copper predominantly exists in the +2 oxidation state in the bulk lattice of $CuWO_4$. But the surface of such semiconductors could have copper in the +1 oxidation state due to the abrupt termination of the surface. These cations could then act as electron or hole traps at the surface, decreasing the photocurrent obtained from the material. Passivation layers are normally used to suppress such recombination losses at the surface. The decrease in the concentration of Cu^+ at the surface, coupled with the increase in photocurrent after the photocharging treatment, could mean that there is some kind of chemical passivation of these electron traps due to the photocharging effect. In fact, Favaro et al. used in-situ HAXPES on $BiVO_4$ and confirmed the light induced formation of a chemical complex between a metal cation within the semiconductor and a solution anion species, which resulted in the "light induced surface passivation".[7] They reported that the formation of this chemical complex is reversible under dark conditions. Similarly, the photocharging treatment in the case of $CuWO_4$, as in this work, could also form such a complex between the copper atoms at the semiconductor surface and borate or perchlorate ions in the solution. Perchlorate ions in solution are normally considered to be "inert" and is less interactive towards an electrochemical surface compared to a borate anion. Therefore, chances are that the photocharging treatment could induce the formation of a copper borate complex at the surface, similar to the formation of a $BiPO_4$ complex as in the report of Favaro et al. The B 1s XPS spectra with a peak at ~ 192.2 eV for the PC – $CuWO_4$ sample, which corresponds to the spectra of boron in a borate form [30, 31], confirms the presence of a borate species at the surface. The O 1s spectra and W 4f spectra did not show a major difference, except for the increase in the peak at 532 eV for the O 1s spectra. As mentioned earlier, this peak is normally attributed to oxygen from chemisorbed species at the surface of the

semiconductor. Therefore, this O1s peak at 532 eV could be due to the oxygen in the borate species at the surface, formed as a result of the photocharging treatment. Similar observations were also made by Favaro et al. [7] and Trześniewski et al. [11] in the case of $BiVO_4$. The valence band XPS spectra for the UT and PC – $CuWO_4$ also looked similar, expect for a significant shift in the valence band maximum (VBM) by ∼ 0.4 eV. Interestingly though, the Mott-Schottky plots suggests that the CB band position has not changed and is fixed at the 0.5 V_{RHE} post photocharging. The valence band (VB) of $CuWO_4$ is composed of Cu(3d) and O(2p) orbitals.[17, 33] There are conflicting reports in the literature about the composition of the conduction band in $CuWO_4$. Some reports suggest that the conduction band (CB) is composed predominantly of W(5d) [17], whereas other reports suggest that it is composed of W(5d) and Cu(3d).[33] It is important to point out here that the penetration depth of a commercial XPS system is ∼ 5 nm from the surface and thus the data represents the chemical composition information of this first five nanometers. Combining the information obtained from the Tauc plot, XRD, Mott-Schottky plot and the XPS data suggests that a hetero-junction of two semiconductors could have formed close to the surface, due to the photocharging treatment. The anodic shift of the VBM by ∼ 0.4 eV indicates that a semiconductor with a higher bandgap may have formed at the surface due to the photocharging treatment. Therefore, this hetero-junction is composed predominantly of the UT - $CuWO_4$ and a higher bandgap semiconductor at the surface. The unchanged bulk data, as observed in the absorption spectra and XRD data of the UT and PC – $CuWO_4$ suggest that the thickness of the higher bandgap semiconductor is extremely small, possibly smaller than 5 nm. The origin of this higher bandgap semiconductor is still unclear. The presence of a borate species at the surface post photocharging, as seen in the B 1s XPS spectra, would suggest that this high bandgap semiconductor might be borate based.

There are reports in literature about the existence of CuB_2O_4 and $Cu_3B_2O_6$ photocatalysts, both semiconductors with bandgaps of ∼ 3.1 eV and ∼ 2.16 eV respectively. (29) Therefore, a hetero-junction could have formed between the $CuWO_4$ and either of these two semiconductors, close to the surface, due to the photocharging treatment. The improved charge separation in the space charge region, post photocharging, would imply that the band bending at this hetero-junction should be favourable for taking the electrons away from the surface and/or drive holes to the SEI for water oxidation. Unfortunately, there are not many reports in literature on these two copper borate species. Especially, there is no information about the absolute band edge positions and the intrinsic fermi level positions of these two semiconductors in the literature, to our knowledge. Therefore, further research is needed to identify the exact composition of this photo-induced copper borate complex. The data obtained from the Mott-Schottky plots cannot be used anymore to determine the CB position because of the existence of this hetero-junction. Figure 5.8 shows an artistic representation of the authors view of the hetero-junction formed, between $CuWO_4$ and copper borate, due to the photocharging process. The improved band bending resulting from this hetero-junction improves the charge separation and minimises charge carrier recombination. The formation of this copper complex could be initialised by the photo-corrosion of $CuWO_4$, similar to the suggestions of Favaro et al on $BiVO_4$. (6) An attempt was made to perform inductively
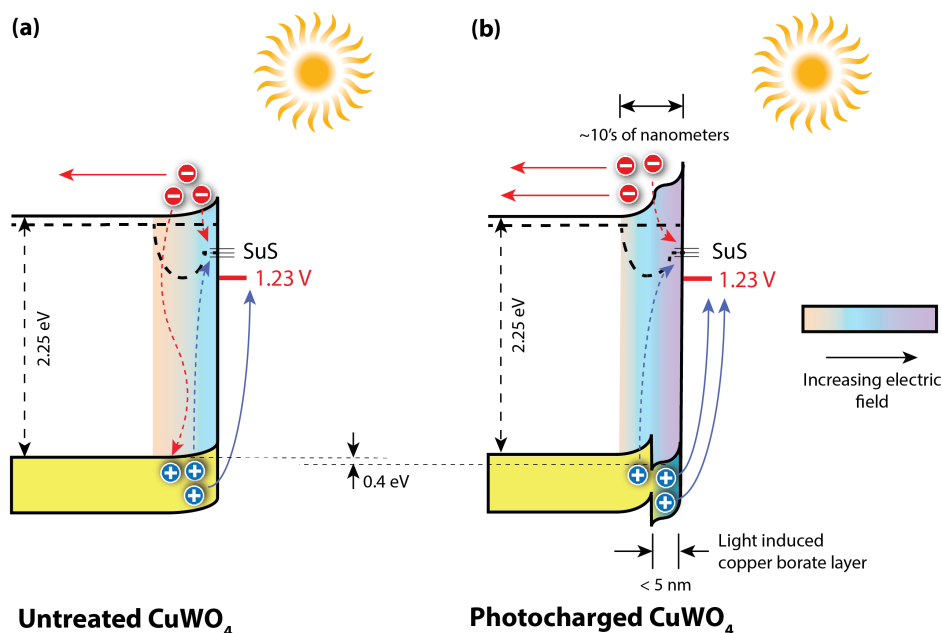
Figure 5.8: (a) Band diagram representing the band bending in the space charge region for UT – CuWO$_4$ (b) A speculative band diagram showing the additional band bending in the space charge region post photocharging, because of the formation of hetero-junction between CuWO$_4$ and the copper borate complex.

coupled plasma – optical emission spectroscopy (ICP-OES) on the electrolyte samples, post photocharging, to see if any copper or tungsten has leached into the solution in the process of photocharging (Table S5.1). However, the data was too erroneous as the concentrations were too low and hence was too close or below the detection limit. High background noise, especially from the sodium ions in the solution also made the measurements erroneous. The open-circuit potential measurements (Figure S5.5) during the photocharging process suggests that the formation of this complex reaches an equilibrium, after a few hours of photocharging, as seen from the plateauing of the OCP after a few hours. Similar observation was also made in the case of BiVO$_4$. [11, 21] Thus, this film probably does not grow beyond a few nanometers in thickness.

5.5. Conclusions

In this work, the effect of photocharging on CuWO$_4$ photoanodes is presented. Prolonged exposure of CuWO$_4$ photoanodes to light under OCP conditions improved the performance of the photoanodes and doubled the photocurrent at 1.23 V$_{RHE}$. This enhancement was seen to be reversible under dark conditions, but at a much slower rate than reports on photocharging of BiVO$_4$. [21] Photoelectrochemical experiments with a hole scavenger suggest that the enhancement in performance is facilitated by a "bulk" factor. Thorough material characterisation suggests that the bulk optical and material

properties have not changed, post photocharging, and neither does the morphology. It is very striking that all these features are very similar to the reports on photocharging of $BiVO_4$. [11, 21]

XPS data suggested a change in the surface chemical composition, post photocharging. There was a decrease in the concentration of Cu^+ at the surface after photocharging. Initial indications suggests that this could be due to chemical passivation of trap sites at the surface. An in-situ HAXPES study on the photocharging of $BiVO_4$ indicated a light induced formation of $BiPO_4$ layer at the surface of $BiVO_4$ during photocharging in a phosphate buffer. [7] In this article, we speculate the build-up of copper borate complex in a similar fashion at the $CuWO_4$ surface, due to photocharging. This results in the formation of a hetero-junction between $CuWO_4$ and the copper borate complex close to the surface. This proposal is supported by the presence of borate peak in the B1s spectra for the PC – $CuWO_4$, additional buildup of a peak at 532 eV in the O1s spectra and a ~ 0.4 eV anodic shift in the valence band maximum. Copper borate exists in two different forms, CuB_2O_4 and $Cu_3B_2O_6$. Both are proven photocatalysts with a bandgap of ~ 3.1 eV and 2.16 eV, respectively. [30] Our data suggests that this copper borate layer is extremely thin and does not grow beyond a few nanometers in thickness. The hetero-junction formed by these two semiconductors leads to an improved charge separation in the space charge region, close to the surface and thus an improvement in the photocurrent post photocharging. More research is needed to determine the exact composition of this copper borate complex.

This article, along with other reports on photocharging of metal oxide semiconductors ($BiVO_4$, WO_3, Fe_2O_3 (6-12)), suggests that the metal oxide semiconductor – electrolyte interface is more complex than normally perceived. The effect of this time - dependent light induced surface layer formation with the electrolyte species at the metal oxide semiconductor surface should be considered in all future works in the field of photo-electrochemistry with metal oxide semiconductors.

5.6. Supplementary information
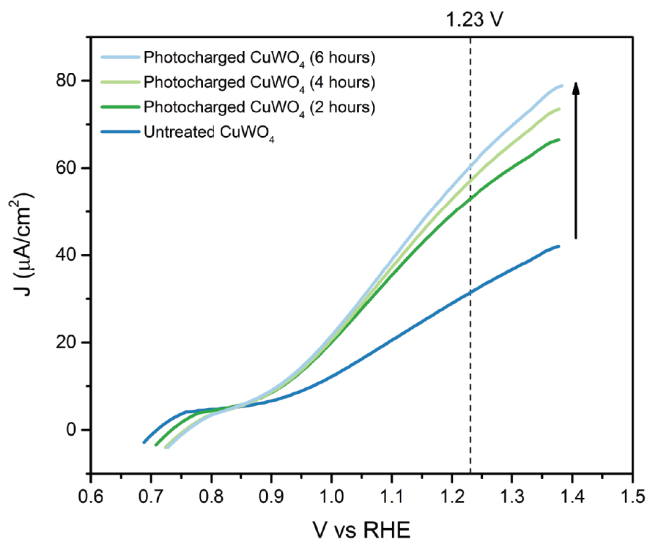
Supplementary Figure S5.1: Photocharging time dependent evolution of performance.
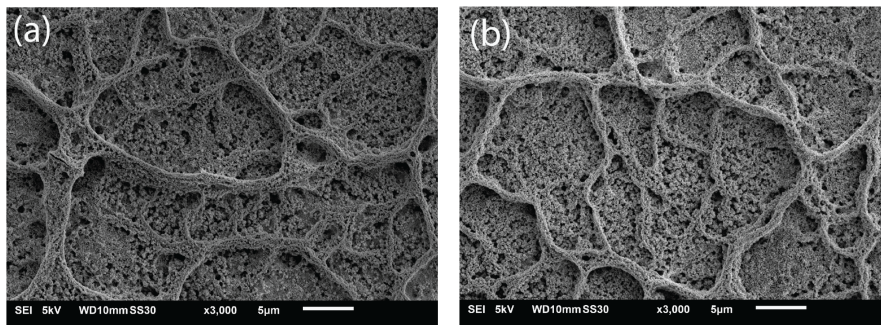
Supplementary Figure S5.2: (a) SEM images of UT – CuWO$_4$ and (b) PC – CuWO$_4$.
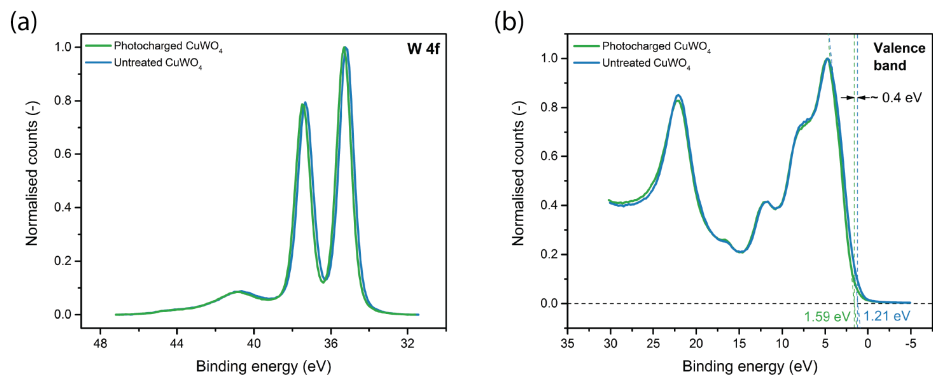
Supplementary Figure S5.3: (a) XPS spectra for W 4f for UT and PC – CuWO$_4$ (b) Valence band spectra for UT and PC – CuWO$_4$ sample.

5
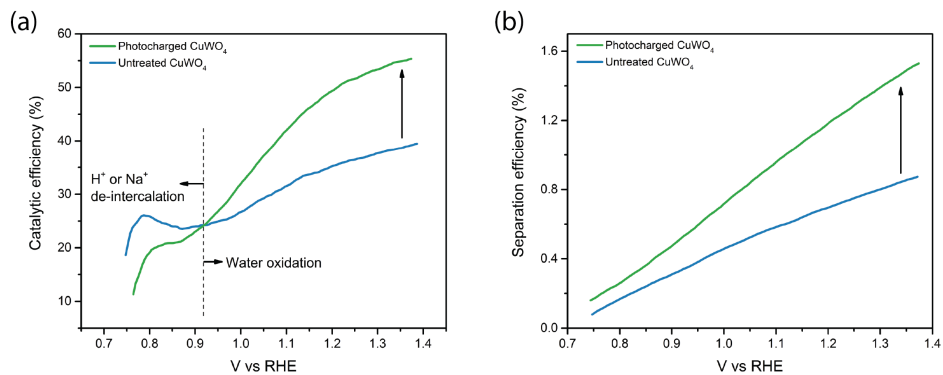
Supplementary Figure S5.4: (a) Catalytic efficiency of UT and PC – CuWO$_4$ (b) Separation efficiency of UT and PC – CuWO$_4$.

The catalytic and separation efficiencies, as in figure S4 (a-b), were calculated as per the method recommended by Dotan et al. [32],

$$\eta_{\text{cat}} = J_{\text{H}_2\text{O}}/J_{\text{hole scavenger}} \times 100\% \qquad\qquad \eta_{\text{sep}} = J_{\text{hole scavenger}}/J_{\text{abs}} \times 100\%$$

Where, $J_{\text{H}_2\text{O}}$ is the photocurrent in the absence of a hole scavenger, $J_{\text{hole scavenger}}$ is the photocurrent in the presence of a hole scavenger and J_{abs} (10.43 mA/cm^2) [13] is the theoretical absorption current density.
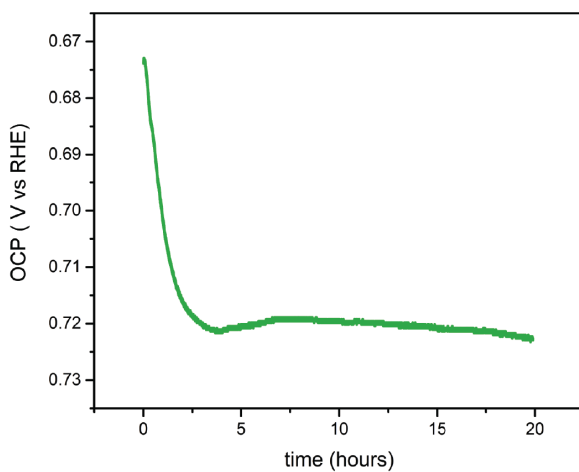
Supplementary Figure S5.5: Open circuit potential (OCP) vs time plot measured during the photocharging process.

5
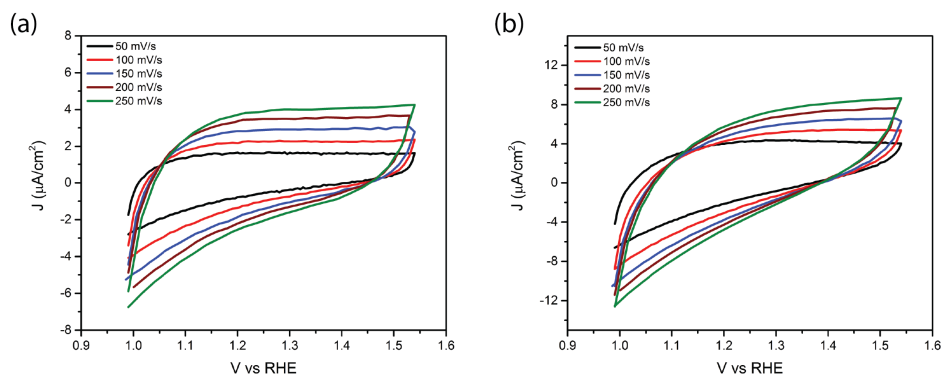
Supplementary Figure S5.6: Cyclic voltammetry scans performed at different scan rates, in the dark, for the ECSA calculation for (a) Untreated $CuWO_4$ (b) Photocharged $CuWO_4$.

Inductively coupled plasma – optical emission spectroscopy (ICP-OES) was used to analyse the electrolyte solution after the photocharging treatment of the $CuWO_4$ samples, to see if the copper or tungsten has leached into the solution during the photocharging treatment. A PerkinElmer Optima 5300 DV ICP-OES system was used for these measurements. Reference solutions were made with known concentrations of copper and tungsten in the electrolyte solution used for this study to make a trend line for calibration.

Table 5.1: ICP-OES measurement data.

Sample	Measured Cu [mg/L]	Measured W [mg/L]
Reference 1 (0 mg/L Cu + 0 mg/L W)	0.005	0.00
Reference 2 (0.26 mg/L Cu + 0.74 mg/L W)	0.055	0.66
Reference 3 (0.51 mg/L Cu + 1.47 mg/L W)	0.085	1.35
Reference 4 (1.02 mg/L Cu + 2.94 mg/L W)	0.159	2.58
10 hour photocharging	<0.05	<0.05
16 hour photocharging	<0.05	<0.05
20 hour photocharging	<0.05	<0.05

5

5.7. References

(1) Venugopal, A.; Smith, W. A. *Faraday Discussions* **2019**, *215*, 175–191.

(2) V. Masson-Delmotte et al. *IPCC, 2018: Global warming of 1.5°C. An IPCC special report on the impacts of global warming of 1.5°C above pre-industrial levels and related global greenhouse gas emission pathways, in the context of strengthening the global response to the threat of cli*; tech. rep.; 2018.

(3) Sixto Giménez, B. J., *Photoelectrochemical solar fuel production*; Springer: Switzerland, 2016.

(4) Zhong, D. K.; Choi, S.; Gamelin, D. R. *Journal of the American Chemical Society* **2011**, *133*, 18370–18377.

(5) Kim, T. W.; Choi, K.-S. *Science* **2014**, *343*, 990–994.

(6) Trotochaud, L.; Mills, T. J.; Boettcher, S. W. *The Journal of Physical Chemistry Letters* **2013**, *4*, 931–935.

(7) Favaro, M.; Abdi, F. F.; Lamers, M.; Crumlin, E. J.; Liu, Z.; Van De Krol, R.; Starr, D. E. *Journal of Physical Chemistry B* **2018**, *122*, 801–809.

(8) Li, T.; He, J.; Pena, B.; Berlinguette, C. P. *Angew Chem Int Ed Engl* **2016**, *55*, 1769–1772.

(9) Li, T.; He, J.; Pena, B.; Berlinguette, C. P. *ACS Appl Mater Interfaces* **2016**, *8*, 25010–25013.

(10) Liu, E. Y.; Thorne, J. E.; He, Y.; Wang, D. *ACS Applied Materials and Interfaces* **2017**, *9*, 22083–22087.

(11) Trześniewski, B. J.; Smith, W. A. *Journal of Materials Chemistry A* **2016**, *4*, 2919–2926.

(12) Xie, J.; Yang, P.; Liang, X.; Xiong, J. *ACS Applied Energy Materials* **2018**, *1*, 2769–2775.

(13) Bohra, D.; Smith, W. A. *Phys Chem Chem Phys* **2015**, *17*, 9857–9866.

(14) Gao, Y.; Hamann, T. W. *J Phys Chem Lett* **2017**, *8*, 2700–2704.

(15) Lhermitte, C. R.; Bartlett, B. M. *Acc Chem Res* **2016**, *49*, 1121–1129.

(16) Valenti, M.; Dolat, D.; Biskos, G.; Schmidt-Ott, A.; Smith, W. A. *The Journal of Physical Chemistry C* **2015**, *119*, 2096–2104.

(17) Yourey, J. E.; Bartlett, B. M. *Journal of Materials Chemistry* **2011**, *21*, 7651.

(18) Yourey, J. E.; Pyper, K. J.; Kurtz, J. B.; Bartlett, B. M. *The Journal of Physical Chemistry C* **2013**, *117*, 8708–8718.

(19) Baeck, S. H.; Choi, K. S.; Jaramillo, T. F.; Stucky, G. D.; McFarland, E. W. *Advanced Materials* **2003**, *15*, 1269–1273.

(20) Smith, W.; Wolcott, A.; Fitzmorris, R. C.; Zhang, J. Z.; Zhao, Y. *Journal of Materials Chemistry* **2011**, *21*, 10792.

(21) Trześniewski, B. J.; Digdaya, I. A.; Nagaki, T.; Ravishankar, S.; Herraiz-Cardona, I.; Vermaas, D. A.; Longo, A.; Gimenez, S.; Smith, W. A. *Energy & Environmental Science* **2017**, *10*, 1517–1529.

(22) Valenti, M.; Venugopal, A.; Tordera, D.; Jonsson, M. P.; Biskos, G.; Schmidt-Ott, A.; Smith, W. A. *ACS Photonics* **2017**, *4*, 1146–1152.

(23) Cooper, J. K.; Gul, S.; Toma, F. M.; Chen, L.; Liu, Y.-S.; Guo, J.; Ager, J. W.; Yano, J.; Sharp, I. D. *The Journal of Physical Chemistry C* **2015**, *119*, 2969–2974.

(24) Ruiz-Fuertes, J.; Sanz-Ortiz, M. N.; González, J.; Rodríguez, F.; Segura, A.; Errandonea, D. *Journal of Physics: Conference Series* **2010**, *215*, 12048.

(25) Yourey, J. E.; Kurtz, J. B.; Bartlett, B. M. *The Journal of Physical Chemistry C* **2012**, *116*, 3200–3205.

(26) Khyzhun, O. Y.; Strunskus, T.; Cramm, S.; Solonin, Y. M. *Journal of Alloys and Compounds* **2005**, *389*, 14–20.

(27) Lin, Z.; Li, W.; Yang, G. *Applied Catalysis B: Environmental* **2018**, *227*, 35–43.

(28) Brisk, M. A.; Baker, A. *Journal of Electron Spectroscopy and Related Phenomena* **1975**, *7*, 197–213.

(29) Rumble, J. R.; Bickham, D. M.; Powell, C. J. *Surface and Interface Analysis* **1992**, *19*, 241–246.

(30) Liu, J.; Wen, S.; Zou, X.; Zuo, F.; Beran, G. J. O.; Feng, P. *J. Mater. Chem. A* **2013**, *1*, 1553–1556.

(31) Ong, C. W.; Huang, H.; Zheng, B.; Kwok, R. W. M.; Hui, Y. Y.; Lau, W. M. *Journal of Applied Physics* **2004**, *95*, 3527–3534.

(32) Dotan, H.; Sivula, K.; Grätzel, M.; Rothschild, A.; Warren, S. C. *Energy Environ. Sci.* **2011**, *4*, 958–964.

(33) Lalić, M.; Popović, Z.; Vukajlović, F. *Computational Materials Science* **2012**, *63*, 163–167.

5

6

Polymer modification of surface electronic properties of electrocatalysts

Finding alternative ways to tailor the electronic properties of a catalyst to actively and selectively drive reactions of interest has been a growing research topic in the field of electrochemistry. In this article, we investigate the tuning of the surface electronic properties of electrocatalysts via polymer modification. We show that when a nickel oxide water oxidation catalyst is coated with polytetrafluoroethylene, stable Ni-CF$_x$ bonds are introduced at the nickel oxide/polymer interface which results in shifting of reaction selectivity away from the oxygen evolution reaction and towards hydrogen peroxide formation. It is shown that the electron-withdrawing character of the surface fluorocarbon molecule leaves a slight positive charge on the water oxidation intermediates at the adjacent active nickel sites, making their bonds weaker. The concept of modifying surface electronic properties of an electrocatalyst via stable polymer modification offers an additional route to tune multi-pathway reactions in polymer/electrocatalyst environments, like with ionomer modified catalysts or with membrane electrode assemblies.

6.1. Introduction

The electrochemical conversion of abundant feedstocks such as water, CO_2, N_2 and O_2 to green value-added chemicals using renewable electricity is very attractive from a sustainability perspective as these chemicals can serve as the basic feedstock to the chemical industry, replacing fossil-based resources. As a result, there has been significant research interest into electrochemical conversion technologies over the past decades.[2–5]

Across the various electrochemical technologies, identifying the right electrocatalyst for different reactions of interest has been one of the main focus areas of researchers. The Sabatier principle is often used as a guideline to find a suitable catalyst for a particular reaction.[6, 7] Based on this principle, computational, and more recently, machine learning approaches have been used to predict potential candidates for selectively catalysing different reactions.[7–9] When a singular material's properties is insufficient for good catalytic activity, the properties of a catalyst or substrate can be tuned by mixing/alloying different elements within the periodic table. [10, 11] However, such strategies may also affect the bulk material properties of the catalyst, such as the conductivity, which is undesirable. Additionally, degradation or phase separation of mixed/alloyed catalysts and operando catalyst restructuring often occur under reaction conditions, making them ineffective for long term operation in practical applications. [12–14] Therefore, there is a need for alternative strategies to tailor the surface electronic property of a catalyst to make it more selective and efficient towards the reaction of interest, while also not affecting their bulk properties.

Polymer modification was previously shown to alter the surface electronic properties of metallic sensing materials in optical hydrogen sensors. [15, 16] This concept could be extended to the field of electrochemistry. Polymers have been previously used in the field of electrochemistry to modify the electrode/electrolyte interfaces [17, 18], however their effect on the surface electronic properties of the electrocatalysts was not extensively studied before. In this letter, we discuss the modification of surface electronic properties of electrocatalysts upon polymer loading, using the recent example of polymer coated water oxidation catalysts.16 Recently, Xia et al. [17] demonstrated that the selectivity of common water oxidation reaction catalysts can be altered from the four electron water oxidation reaction to oxygen, to the two electron water oxidation reaction to hydrogen peroxide by coating these catalysts with a hydrophobic polytetrafluoroethylene (PTFE) polymer. The NiOx/PTFE system is shown in Figure 6.1. It was suggested that this change in selectivity was due to the weakening of the binding energy of the OH* intermediate by two factors. First, by the destabilisation of the OH* intermediate due to the breakage of the hydrogen bonding network within the surrounding electrolyte, because of the presence of the hydrophobic PTFE. Second, due to a less oxidized catalyst surface because of the reduced local H_2O concentration in the presence of hydrophobic PTFE. Theoretical calculations showed that this less oxidized catalyst surface can weaken the OH* binding energy, altering the selectivity of the water oxidation reaction. While these are plausible explanations for the effect of PTFE, more work needs to be done to experimentally verify and support these claims, as well as providing further details that

allow the approach to be extended to other electrochemical applications.
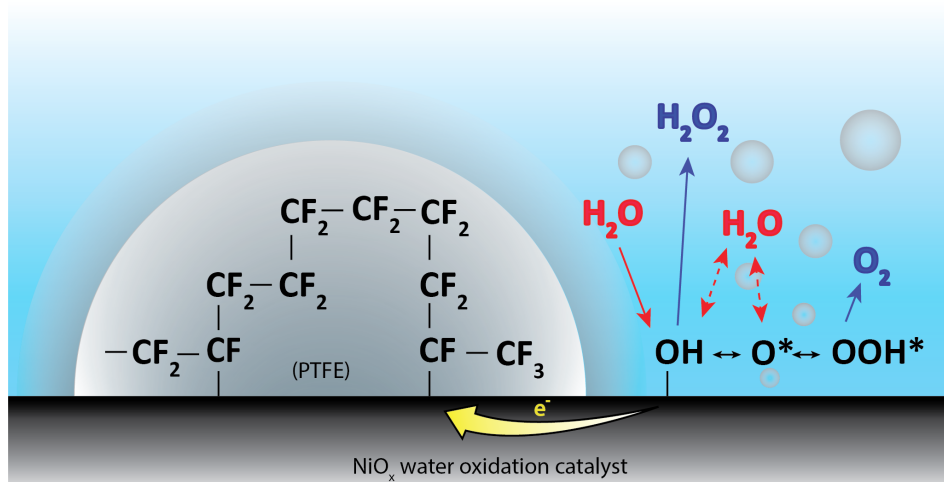
Figure 6.1: Schematic of the PTFE polymer coated NiO_x water oxidation catalyst system. The two electron and the four electron water oxidation pathway to hydrogen peroxide (H_2O_2) and oxygen (O_2) are also shown here. Red colour represents the reactants and blue colour represents the products. The PTFE polymer is chemically bound to the NiO_x water oxidation catalyst. The electron withdrawing nature of the chemically bound fluorocarbon molecules alters the catalytic properties of adjacent active sites.

In this work, we present an alternative explanation to the effect of this PTFE loading for the stable modification of an electrocatalyst's surface properties. We show that polymers having an electron withdrawing or donating character, can alter the electronic properties of the adjacent active sites in the catalyst when bound to the catalyst surface. Using X-ray photoelectron spectroscopy (XPS), we show that the PTFE coated nickel foam results in the formation of Ni-CF_x bonds at the nickel oxide/PTFE interface. Further, using Density Functional Theory (DFT) calculations on a CF_x bound β-NiOOH surface, we demonstrate that the binding of OH* intermediate is destabilized in the presence of these Ni-CF_x bonds, while the step in Gibbs free energy towards the O* intermediate is increased. The reduced binding energy of OH* and the suppressed formation of O* intermediate collectively tunes the selectivity of the water oxidation reaction towards the two electron pathway of hydrogen peroxide formation.

6.2. Materials and methods

6.2.1. Experimental

Preparation of PTFE dip-coated Ni foam
PTFE dip-coated nickel foams were fabricated by first ultrasonically cleaning (Emmi-30 HC sonicator) the 2.5 x 2.5 cm^2 substrate (0.5 mm Ni foam 110PPI, Gelon Energy Co. Ltd) consecutively in acetone and de-ionized water, facilitating or enhancing the

removal of contaminants adhering to the three-dimensional metal scaffold. Substrates were dried with nitrogen gas. Then, the foam was pre-treated by UV/ozone cleaning (60 °C, 45 min). Ni foam was soaked horizontally into 60 wt% PTFE aqueous solution for 10 min and dried vertically at 120 °C under ambient conditions for 1 hour. Samples with lower concentrations of PTFE were prepared by diluting the 60% PTFE solution. The Ni foam-PTFE electrode was annealed in a tube oven at 350 °C under argon atmosphere for 30 min, unless otherwise specified. Pristine Ni samples for blank measurements were also cleaned using the exact same procedure and annealed in a tube oven at 350 °C under argon atmosphere for 30 min, after dipping in ultrapure water for 10 min instead of the 60% PTFE solution.

Preparation of PTFE-dip coated CFP

Carbon-based electrodes were prepared by first ultrasonically cleaning 2.5 x 2.5 cm^2 CFP (Sigracet 29AA, Fuel Cell store) substrates in de-ionized water using an Emmi-30 HC sonicator. The CFP was pre-treated by UV/ozone (60 °C, 45 min). The 190 μm thick as-treated CFP was soaked horizontally into 60 wt% PTFE aqueous solution for 10 min and dried vertically at 120 °C under ambient conditions for 1 hour. Next, the dip coated CFP samples were annealed in a tube oven at 350 °C under argon atmosphere for 30 min.

Electrochemistry

Electrochemical experiments on pristine and PTFE coated nickel foam and carbon fibre paper electrocatalysts were run at room temperature in a customized gas$_2$SO$_4$ and left in lightly boiling ultrapure water for 20 min, after it was rinsed thoroughly with ultrapure water. Cathodic and anodic compartments were separated by a Nafion 115 (FuelCell-Store) cation-exchange membrane to prevent H_2O_2 degradation by cathodic reduction. A Solartron Analytical potentiostat was employed to control and record the electrochemical response. In a three-electrode configuration, the anodic compartment contained the nickel or carbon working electrode and a silver/silver chloride reference electrode (XR300, Radiometer Analytical), while a Pt mesh was used as the counter electrode. An aqueous solution of 1.0 M K_2CO_3 (pH 12.97) was used as an electrolyte, and the anolyte was stirred at a rate of 500 rpm during electrolysis. Formed H_2O_2 was stabilized by addition of 4 mg/ml Na_2SiO_3 (Sigma-Aldrich) to the electrolyte. The working electrode was subjected to a range of different potentials and were converted to the RHE scale using $E_{RHE} = E_{Ag/AgCl} + E°_{Ag/AgCl} + 0.059 \times pH$, where $E°_{Ag/AgCl}$ is the standard potential of Ag/AgCl at 25 °C (0.197 V) and pH values were determined by a calibrated pH meter.

For measuring H_2O_2 concentrations a 0.02 M $KMnO_4$ (standardized against sodium thiosulfate, Titripur, reag. Ph. Eur., Sigma Aldrich) solution is used as the titrant. Concentrated sulphuric acid (95.7 wt%, Fisher Scientific) is diluted by addition to Milli-Q until a volumetric ratio of 1:1 is achieved. The solution was then cooled down to room temperature by immersing the flask in a bath of cold water. A 3 mL aliquot of electrolyte was added to a 50 mL beaker. Next, 15 mL of dilute H_2SO_4 was slowly added to the aliquot. The $KMnO_4$ titrant was added dropwise to the stirred solution using a burette. After a permanent light pink was apparent in the stirred solution the added volume of titrant was calculated and the procedure was repeated thrice for accuracy determination. Given the measured volume of titrant V_{EP} to reach the endpoint, the accumulated

H_2O_2 concentration $C_{H_2O_2}$ (ppm) follows from the reaction stoichiometry between H_2O_2 and MnO_4^-, as shown below :

$$2\,KMnO_4 + 5\,H_2O_2 + 3\,H_2SO_4 \longrightarrow K_2SO_4 + 2\,MnSO_4 + 8\,H_2O + 5\,O_2 \qquad (6.1)$$

$$C_{H_2O_2} = \frac{(5/2).34.015.V_{EP}.C_{KMnO_4}}{V_{Al}} \qquad (6.2)$$

where C_{KMnO_4} is the concentration of titrant (mol/l), V_{Al} is the volume of the electrolyte aliquot (l), and 34.015 is the molar mass of H_2O_2 (g/mol).

X-Ray Photoelectron Spectroscopy
The XPS spectra were generated by Al and Mg Kα X-ray sources. A Thermo Scientific K-alpha apparatus equipped a Flood Gun for charge compensation of the sample was used as an Al Kα X-ray source. Parameters used for the measurements were: spot size of 400 μm, pass energy of 50 eV, energy step size of 0.1 eV and a dwell time of 50 ms. X-ray photoelectron analysis was carried out using a PHI-TFA XPS spectrometer (Physical Electronic Inc.) for Mg-monochromatic measurements. The vacuum during XPS analysis was 10^{-9} mbar. The analyzed area was 0.4 mm in diameter and the analysis depth was ~ 3-5 nm. Narrow multiplex scans of the peaks were recorded using a pass energy of 35 eV with a step size 0.5 eV, at a take-off angle of 45° with respect to the sample surface. Low energy electron gun was used for surface charge neutralization XPS. Spectra were processed using Multipak v8.0 (Physical Electronics Inc.).

6.2.2. Density Functional Theory calculations

β-NiOOH DFT+U Calculations
All spin-polarized density functional theory (DFT) calculations in the present work have been carried out within the periodic plane wave framework as implemented in Vienna Ab initio Simulation Package (VASP) version 5.4.1. The DFT+U correction method of Dudarev et al. [19] was employed to ameliorate the known deficiencies when describing partially occupied 3d shells with the traditional approach. A U-J value of 5.5 eV for Ni(III) was added in combination with the Perdew-Burke-Ernzerhof (PBE) exchange-correlation functional. This value was adapted from the linear response theory calculations of Li and Selloni [20] on β-NiOOH and has been confirmed to lead to accurate replication of electronic and structural properties among other parameter values by Carter et al. [21] Blöchl's all-electron, frozen-core, projector augmented wave (PAW) method was used. The initial β-NiOOH structure (that was subsequently optimized) was taken from the literature. [22] Convergence to within less than 1 meV/atom for the total energies is achieved using a plane-wave kinetic energy cut-off of 500 eV and a Γ-point-centered Monkhorst-Pack k-point mesh of size 3 x 3 x 1 for unit cell calculations. Geometry optimizations were carried out until the forces on all atoms were less than 0.01 eV/Å. The positions of all atoms were allowed to relax but lattice parameters were fixed to their equilibrium bulk values. Gaussian smearing with a width of 0.01 eV was used to aid the convergence of the calculations. Non-converging situations were helped by switching from Pulay mixing with an initial approximation for the charge dielectric function
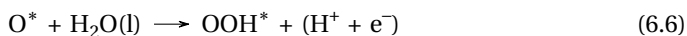
according to Kerker, to a linear mixing algorithm. Brillouin zone integration using the tetrahedron method with Blöchl corrections was used subsequently to evaluate the final energies. Moreover, dipole corrections were applied in the direction perpendicular to the slab. For all of the analyses, assessment of the different models and graphical representation of the structures obtained were carried out with Visualization for Electronic and Structural Analysis (VESTA) software codes.

The β-NiOOH and β-NiOOH-CF$_3$ unit cells

Unit cell calculations were performed on a stoichiometric slab model with half of the surface oxygen atoms hydroxylated (Ni$_{16}$O$_{31}$H$_{16}$). Rossmeisl et al. found that the OER overpotential on RuO$_2$ was lower on an O-terminated slab than on an OH-terminated slab. [23] Because NiOOH is not stable for a fully O-terminated slab, we instead assessed the OER performance on a surface with less than full hydroxylation. The active site on the oxide catalyst that allowed formation of the different adsorbed intermediates was a coordinatively unsaturated site on one side of the slab in the unit cell. To chemically bind the short-polymer CF$_3$ to the metal surface a terminating OH group was removed from a Ni site on the same side as the unsaturated Ni. Slabs of four layers were used for all surface calculations. The resulting relaxed unit cells for β-NiOOH is displayed in Figure 6.5.

The β-NiOOH and β-NiOOH-CF$_3$ unit cells

At variance with the numerous experimental investigations, computational studies on the two-electron H$_2$O-to-H$_2$O$_2$ reaction are still scarce. Most studies in this domain consider the OH* intermediate as the sole intermediate and descriptor for catalyst activity: weak OH* free energy will lead to a high preference towards the two-electron route. [24, 25] The associative mechanism for the four-electron water oxidation involves five elementary steps: one thermochemical step (eq. 6.3) and four electrochemical steps (eq. 6.4-6.7), where the * symbol used refers to a unique free catalytic site. After thermochemical water adsorption at the active site to form H$_2$O*, the intermediate undergoes deprotonation and proton coupled electron transfer (PCET) to form OH* species with production of a H$^+$/e$^-$ pair. Formed OH* is converted to O* by a following PCET, and addition of a water molecule and a PCET event converts the O* species to OOH*. Finally, O$_2$ gas and the fourth H$^+$/e$^-$ is produced from a last PCET step. Protons ejected into the electrolyte will eventually meet a transferring electron at the cathode. The desorption of O$_2$ – which is a thermochemical step – has been omitted because GGA tends to fail miserably at describing gas-phase reaction barriers and describing the energetics of O$_2$* along its reaction coordinate. [26, 27]

$$* + H_2O(l) \longrightarrow H_2O^* \tag{6.3}$$

$$H_2O^* \longrightarrow OH^* + (H^+ + e^-) \tag{6.4}$$

$$OH^* \longrightarrow O^* + (H^+ + e^-) \tag{6.5}$$

$$O^* + H_2O(l) \longrightarrow OOH^* + (H^+ + e^-) \tag{6.6}$$

$$OOH^* \longrightarrow O_2 + (H^+ + e^-) + * \tag{6.7}$$
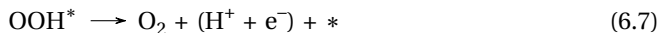
Considering the associative mechanism, the equation for the two-electron H_2O_2 production consistently used involves the addition of a water molecule and a PCET event that converts the OH intermediate (eq. 6.8).1 [28, 29] Next to this so-called Volmer-Heyrovksi mechanism, another possibility was considered. Repetition of the Volmer step and direct coupling of the two adsorbed OH^* intermediates at the surface is referred to as the Volmer-Tafel mechanism (eqn. 6.9). These two mechanisms thus differ in the sequence by which the second water molecule is deprotonated. Due to the size induced limitation of our slabs, only Volmer-Heyrovski mechanism is considered in this work.

$$OH^* + H_2O(l) \longrightarrow H_2O_2(l) + (H^+ + e^-) + * \quad \textit{(Volmer−Heyrovski)} \tag{6.8}$$

$$OH^* + OH^* \longrightarrow H_2O_2(l) \quad \textit{(Volmer−Tafel)} \tag{6.9}$$
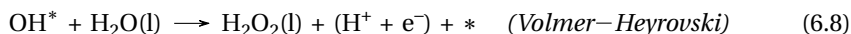
The trends for water oxidation chemistry can, thus, be described by the binding of four key intermediates: H2O*, OH*, O*, and OOH*. Clearly, after adsorption of the OH intermediate the water oxidation could either evolve towards complete four-electron oxygen evolution or two-electron peroxide generation. It should be noted here that all considered electrochemical steps have been written in the "acidic" convention where each equation consists of the production of a proton rather than the consumption of a hydroxide ion. For the present thermodynamic study, the acidity or basicity of the environment has no ramifications for the equilibrium constants of each of the electrochemical steps as they only depend on the potential versus RHE (U_{RHE}).

Thermodynamic intermediate free energy calculations
From a modelling point of view, DFT allows simple calculation of the free energies of surface adsorbed species but determining the chemical potentials of the removed protons and electrons imagined as being put into a reservoir is much less straightforward. As a remedy to this dilemma, Rossmeisl and Nørskov put forward the idea of following the experimental comparison route used for electrochemical performances: aligning potentials with respect to a reference reaction. [23] Catalytic activity for OER on the NiOOH active sites was characterized by calculating the Gibbs free energies of the individual reaction steps using the standard hydrogen electrode (SHE) as a reference electrode. The acidic, associative mechanism has four elementary steps that involve electron and proton transfer processes ($H^+ + e^-$), and their Gibbs free energy is usually calculated implicitly by assuming the equilibrium $H^+ + e^- \longrightarrow 1/2 \ H_2$.12 The effect of the electrode potential U_{SHE} on all electrochemical steps releasing an electron in the electrode is included by shifting the Gibbs free energy by $\Delta G_U = -eU$. At standard conditions (pH = 0, pressure p_{H_2} = 1 bar, and T = 298 K) the reaction free energy is zero at an applied potential of U = 0. Then, the free energy $\Delta G^0 = \Delta G(U = 0, pH = 0, p = 1 \ bar, T)$ of the reaction $^*AH \longrightarrow A + H^+ + e^-$, can be calculated as the free energy of the reaction $AH \longrightarrow A +$

1/2 H_2. The free energy of $H^+ + e^-$ in solution, thus, equals that of 1/2 H_2 in the gas phase.

The reaction Gibbs free energies, ΔG_n corresponding to equations 6.3-6.7 (referred at equation 1 - 5), which provide the binding strength between the NiOOH catalyst and OER intermediates, are shown in equations 6.10-6.14. Calculated values for the reaction free energy ΔE are corrected by including zero-point energies due to reaction (ΔZPE), the change in entropy ($T\Delta S$), and enthalpy correction (ΔH) (i.e., $\Delta G_n = \Delta E + \Delta ZPE - T\Delta S + \Delta H$). The total Gibbs free energy of the four-electron water oxidation reaction $2\,H_2O \longrightarrow O_2 + 2\,H_2$ is fixed at the experimental value (4.92 eV) to avoid the need for performing energy calculations on O_2, since using DFT with a GGA functional is erroneous in accurately describing the electronic structure and energy of the molecule. [23]

$$\Delta G_1 = E_{H_2O*} - E_* - E_{H_2O} + (\Delta ZPE - T\Delta S + \Delta H)_1 \qquad (6.10)$$

$$\Delta G_2 = E_{OH*} + 1/2E_{H_2} - E_{H_2O*} + (\Delta ZPE - T\Delta S + \Delta H)_2 - eU \qquad (6.11)$$

$$\Delta G_3 = E_{O*} + 1/2E_{H_2} - E_{OH*} + (\Delta ZPE - T\Delta S + \Delta H)_3 - eU \qquad (6.12)$$

$$\Delta G_4 = E_{OOH*} + 1/2E_{H_2} - E_{O*} - E_{H_2O} + (\Delta ZPE - T\Delta S + \Delta H)_4 - eU \qquad (6.13)$$

$$\Delta G_5 = 4.92 - \Delta G_1 - \Delta G_2 - \Delta G_3 - \Delta G_4 + (\Delta ZPE - T\Delta S + \Delta H)_5 \qquad (6.14)$$

where $E_*, E_{H_2O*}, E_{OH*}, E_{O*}, E_{OOH*}$ are the total energies of the clean surface (*) and of surfaces with the single adsorbed species OH, O, and OOH, respectively, and E_{H_2O} and E_{H_2} are the total energies of H_2O and H_2 molecules, all obtained from DFT calculations. $(\Delta ZPE - T\Delta S)_n$ (n = 1, 2, 3, 4) can be calculated as:

$$(\Delta ZPE - T\Delta S + \Delta H)_1 = (ZPE_{H_2O*} - TS_{H_2O*} + H_{H_2O*}) - (ZPE_* - TS_* + H_*) \\ + (ZPE_{H_2O} - TS_{H_2O} + H_{H_2O}) \qquad (6.15)$$

$$(\Delta ZPE - T\Delta S + \Delta H)_2 = (ZPE_{OH*} - TS_{OH*} + H_{OH*}) - (ZPE_{H_2O} - TS_{H_2O} \\ + H_{H_2O}) + 1/2(ZPE_{H_2} - TS_{H_2} + H_{H_2}) \qquad (6.16)$$

$$(\Delta ZPE - T\Delta S + \Delta H)_3 = (ZPE_{O*} - TS_{O*} + H_{O*}) - (ZPE_{OH*} - TS_{OH*} + H_{OH*}) \\ + 1/2(ZPE_{H_2} - TS_{H_2} + H_{H_2}) \qquad (6.17)$$

$$(\Delta ZPE - T\Delta S + \Delta H)_4 = (ZPE_{OOH*} - TS_{OOH*} + H_{OOH*}) - (ZPE_{O*} - TS_{O*} \\ + H_{O*}) + 1/2(ZPE_{H_2} - TS_{H_2} + H_{H_2}) \qquad (6.18)$$

Zero-point energies and thermal corrections were calculated using the harmonic oscillator approximation at standard state conditions (298 K) to evaluate vibrational enthalpic and entropic terms for the adsorbates once bound to the surface. ZPEs and thermal contributions for the adsorbates prior to adsorption were taken from the literature and originate from ideal gas, rigid rotor, and harmonic oscillator approximations to evaluate respectively translational, rotational, and vibrational terms. Numerical Hessian matrices were constructed from finite differences of displacement and force components on each atom. The adsorbed intermediate, as well as the Ni/O/H atoms and polymer fragment in first layer nearest to the reaction intermediate, were displaced by ± 0.02 Å in all three directions from their equilibrium positions. The resulting Hessian matrix then was diagonalized to yield the vibrational frequencies ν_j corresponding to each normal mode j. By applying statistical thermodynamics based on the harmonic oscillator model the vibrational contributes are given by equations 6.20-6.21. Enthalpy changes due to temperature increase from 0 to 298 K are expected to be small and are normally neglected in calculations (assuming $\Delta H_{(298 K)} = \Delta H_{(0 K)}$) [30, 31], but are considered here because the energy reported by Carter et al. for the pristine slab has been used in this model.

$$ZPE = \frac{1}{2}\Sigma_j \quad \nu_j \tag{6.19}$$

$$S_{vib} = \Sigma_j \left[\frac{\nu_j}{T(exp(\frac{\nu_j}{kT})-1)} - k * ln(1 - exp(-\frac{\nu_j}{kT}))\right] \tag{6.20}$$

$$(H(T) - H(0))_{vib} = \Sigma_j \quad \frac{\nu_j}{T(exp(\frac{\nu_j}{kT})-1)} \tag{6.21}$$

where k is the Boltzmann constant and T is the temperature. Zero-point vibrational energy correction is required to obtain the true zero-temperature energy of the system.

Following scaling relations were used in this work :

$$\Delta G_{O*} = 2\Delta G_{OH*} + 0.28 (eV) \tag{6.22}$$

$$\Delta G_{OOH*} = \Delta G_{OH*} + 3.2 (eV) \tag{6.23}$$

Lastly, following a similar approach for obtaining free energies and energy corrections, the effective adsorption energies of key OER intermediate species at the surface O vacancy site, ΔE_i (i = OH*, O*, and OOH*), were calculated relative to H_2O and H_2 (at U = 0 and pH = 0) [30, 32] :

$$\Delta E_{OH*} = E_{OH*} - E_* - E_{H_2O} + 1/2 E_{H_2} + (\Delta ZPE - T\Delta S + \Delta H)_A \tag{6.24}$$

$$\Delta E_{O*} = E_{O*} - E_* - E_{H_2O} - E_{H_2} + (\Delta ZPE - T\Delta S + \Delta H)_B \tag{6.25}$$

$$\Delta E_{OOH*} = E_{OOH*} - E_* - 2E_{H_2O} + 3/2 E_{H_2} + (\Delta ZPE - T\Delta S + \Delta H)_C \tag{6.26}$$

Here A, B and C represents the resultant one-step reaction to get from the reactants (H_2O and the free catalytic site (*) to get to the desired intermediates (OH*, O* and OOH*), respectively.

Thermodynamic intermediate free energy calculations

Electron density calculations were performed within the density functional theory framework. The calculated electron charge density from the relaxed atomic structure was used to perform Bader charge analysis to investigate the electron transfer nature and electronic interactions for Ni-CF_3 adsorbate systems, using the code developed by Henkelman and co-workers. [33] This algorithm is based on the Bader partitioning scheme where properties of the condensed phase system are decomposed into contributions from the individual atoms.

6.3. Results

We start by experimentally reproducing the work of Xia et al. [17] on Ni foam, by coating the Ni foam with PTFE using the same procedure as their work and studying the changes in selectivity towards the two electron water oxidation reaction. These results and their explanations are presented in the SI (Figure 6.1 – 6.2). In short, an increased selectivity towards the two electron water oxidation reaction to hydrogen peroxide was reproduced when the Ni foam was coated with PTFE, similar to the observations of Xia et al. [17], confirming that the polymer modification has indeed altered the catalytic property of the electrocatalyst.

To elucidate the cause of the observed selectivity change upon polymer loading, X-ray Photoelectron Spectroscopy (XPS) was performed on pristine and PTFE coated Ni foam electrodes. A Mg Kα X-ray source was used to perform XPS measurements, to prevent the overlap of the Ni2p 3/2 core electron spectra and the fluorine KLL auger electron spectra, as shown in Figure 6.3. Observing the comparative Ni2p 3/2 spectra in Figure 6.2 (a), the pristine and PTFE coated Ni electrodes show large differences in their relative peak positions and shapes, suggesting that the PTFE coating has introduced electronic modifications on the surface nickel atoms. Under normal conditions in air, Ni foam is covered with a native oxide layer, in the form of NiO. [34] This native oxide layer is typically $\sim$ 2-3 nm thick, which is also the probing depth of the XPS. The spectra of pristine Ni foam in Figure 6.2 (a) is thus a typical Ni2p 3/2 spectra for a NiO layer, with the main Ni2p 3/2 peak at 853.9 eV along with its broad satellite peaks at 860.9 eV. Additionally, the Ni2p 3/2 main peak also has a shoulder peak at 855.5 eV. The most common interpretation suggests that this shoulder peak is a result of some surface and non-local screening effect. [35, 36] The spectra for the PTFE coated Ni foam sample in Figure 6.2 (a) is very different compared to that of pristine Ni sample. The Ni2p 3/2 main peak in the PTFE coated sample has shifted to higher binding energies while its satellite peak is relatively unchanged when compared to that of the pristine sample. Additionally, the Ni2p 3/2 main peak now has two shoulder peaks at 853.3 eV and 853.9 eV. The broad shoulder peak present in the pristine sample at 855.5 eV, now overlaps with the main peak of the PTFE coated sample. For both spectra, a small shoulder peak at 852.4 eV is also visible,

which is the contribution from the bulk nickel metal.
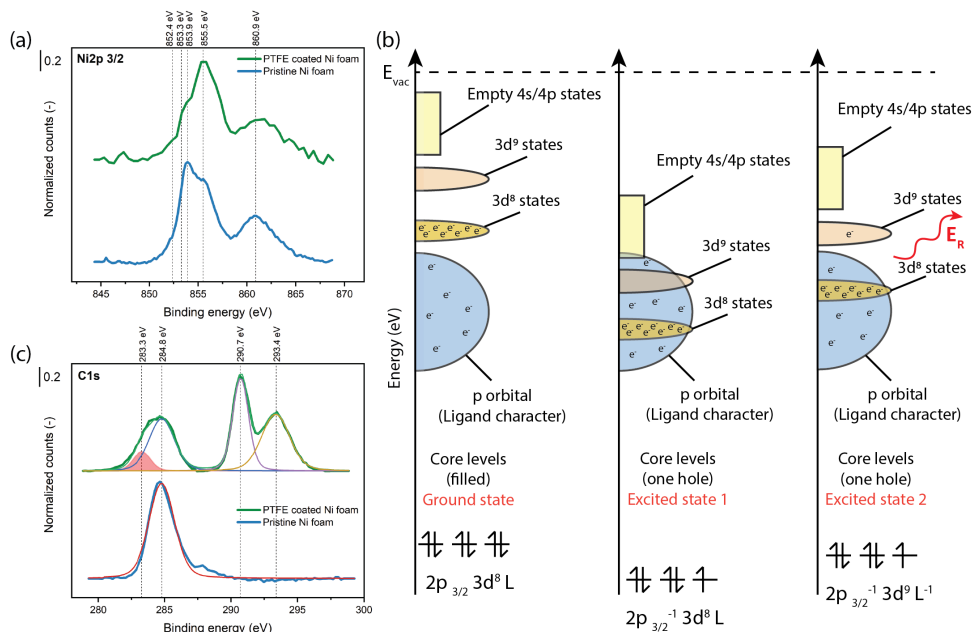
Figure 6.2: (a) Ni2p 3/2 XPS spectra of the pristine and PTFE coated Ni foam water oxidation catalyst. (b) Schematic representation of Kotani – Toyozawa model [37, 38] in nickel insulators. Here the ground state and the two different excited states are shown. In the ground state, the metal d band is above the ligand p band. In the excited state, because of the photoionized ion, the d band is pulled below the Fermi level. Now, there is a possibility of the 3d^9 band getting an electron from the ligand p band, resulting in local screening. When this d band is not filled, it results in the excited state 1, which is represented by the satellite peak in the Ni 2p 3/2 spectra. When the d band is filled by an electron from the ligand p band, it results in the excited state 2, which is represented by the main peak in the Ni 2p 3/2 spectra. (c) C1s spectra of the pristine and PTFE coated Ni foam sample. The fitted peak with the red fill represents the Ni-C bond in the C1s spectra.

To explain the changes in the main peak position in the Ni2p 3/2 spectra with and without the PTFE coating we use the Kotani and Toyozawa model. [37, 38] The ejection of a core electron creates an instantaneous increase in the Coulombic potential around the photogenerated core hole. This localized increase in the potential pulls the metal orbitals towards the nucleus of this photoionized ion, as shown in Figure 6.2 (b). As a result, the empty 3d^9 band in nickel is locally lowered below the top of the valence band, shown as excited state 1 in Figure 6.2 (b). This excited state is a transition state that only exists within the lifetime of the core hole, which is in the order of femto seconds. During this short period, there is a finite probability of this 3d^9 band being filled by the electrons from the top of the valence band. In cases where the 3d^9 band remains empty, the energy of the emitted photoelectron is not altered and results in the higher binding energy satellite peak in the Ni2p 3/2 spectra. In cases where the 3d^9 band is filled (shown as excited state 2 in Figure 6.2 (b)), energy is released due to a relaxation process which is

then transferred to the emitted photoelectron. This process increases the kinetic energy of the photoelectron resulting in the main peak at a lower binding energy in the Ni2p 3/2 spectra. The valence band in these insulating materials primarily has a ligand characteristic. The magnitude of relaxation energy is thus dependent on the nature of the ligand p band. Therefore, the binding energy of the Ni2p 3/2 main peak in insulating Ni materials like NiO is affected by the nature of the ligand coordinated to the Ni, while the binding energy of the Ni2p 3/2 satellite peak is not affected by the nature of the ligand. The difference in the main peak positions in the Ni2p 3/2 spectra in the pristine and the PTFE coated Ni samples is thus an indication that a different Ni-ligand coordination exists in the two samples. The Ni2p 3/2 satellite peak positions of the pristine and PTFE coated samples remain unchanged since these peak positions are not affected by the nature of the ligand, validating this ligand theory. The valence band spectra of the pristine and PTFE coated samples in Figure 6.4 (a) also confirm that the nature of the valence band has been altered with the PTFE coating, showing additional contributions from the PTFE layer.

These results indicate that the PTFE polymer is electronically coordinated to the Ni in the PTFE coated samples. This coordination can either be through the carbon or through the fluorine atoms in the PTFE polymer. If the coordination was through the fluorine atoms, there should also be signatures of Ni-F bond in the Ni2p 3/2 spectra and in the F1s spectra (Figure 6.4 (b)). The main peak for Ni-F bond is expected to be around ~ 858 eV in the Ni2p 3/2 spectra [36, 39], which is not present in Figure 6.2 (a). No Ni-F bond feature was found in the F1s spectra either. On the other hand, if a Ni-C bond is present, a peak is expected in the region of ~ 853.3 eV in the Ni2p 3/2 spectra. [40, 41] This is one of the shoulder peaks present in the Ni2p 3/2 spectra for the PTFE coated sample, suggesting that the polymer is linking with the nickel centre through the carbon, resulting in Ni-CF$_x$ bonds. The shoulder peak at 853.9 eV in the Ni2p 3/2 spectra is originating from the Ni-O coordination from the bulk, which is not affected by the CF$_x$ ligand coordination at the surface of the PTFE coated samples. The Ni-C coordination is further confirmed by the C1s spectra, where an additional shoulder peak at 283.3 eV is observed upon PTFE coating which is typically ascribed to a Ni-C bond in the C1s spectra. [40, 42] Additionally, peaks pertaining to CF$_2$ and CF$_3$ originating from the PTFE polymer are visible at 290.7 eV and 293.4 eV in the C1s spectra of the PTFE coated sample. [16, 43] Adventitious carbon (C-C) and (O-C=O) peaks at 284.8 eV and 287.8 eV are also visible for the pristine and PTFE coated samples, respectively. The F1s XPS spectra of the sample after electrolysis, in Figure 6.4 (b), also confirms that the polymer did not change or degrade during the electrolysis.

Having confirmed the existence of Ni-polymer bond on the PTFE coated sample via XPS, we proceed to further understand its impact on the selectivity towards the water oxidation reaction using computational techniques. The activity and selectivity changes on different catalysts can be predicted by studying the changes in the free energy of the reaction intermediates. The adsorption free energies of the relevant water oxidation intermediates (ΔG_{OH^*}, ΔG_{O^*} and ΔG_{OOH^*}) can be calculated using the Density Functional Theory (DFT) calculations. [22, 28, 44] Although the thermodynamic analysis can only

be taken as qualitative, since kinetic activation barriers between the intermediates are not included, it has proven useful in rationalizing trends in activity for catalytic surfaces. [23, 32] Therefore, performing DFT calculations on the pristine and PTFE coated Ni foam electrodes can help us understand the effect of the Ni-polymer bond on the water oxidation reaction selectivity. The presented thermodynamic analysis is thus a first step towards understanding the activity and selectivity changes on polymer modified electrocatalysts.
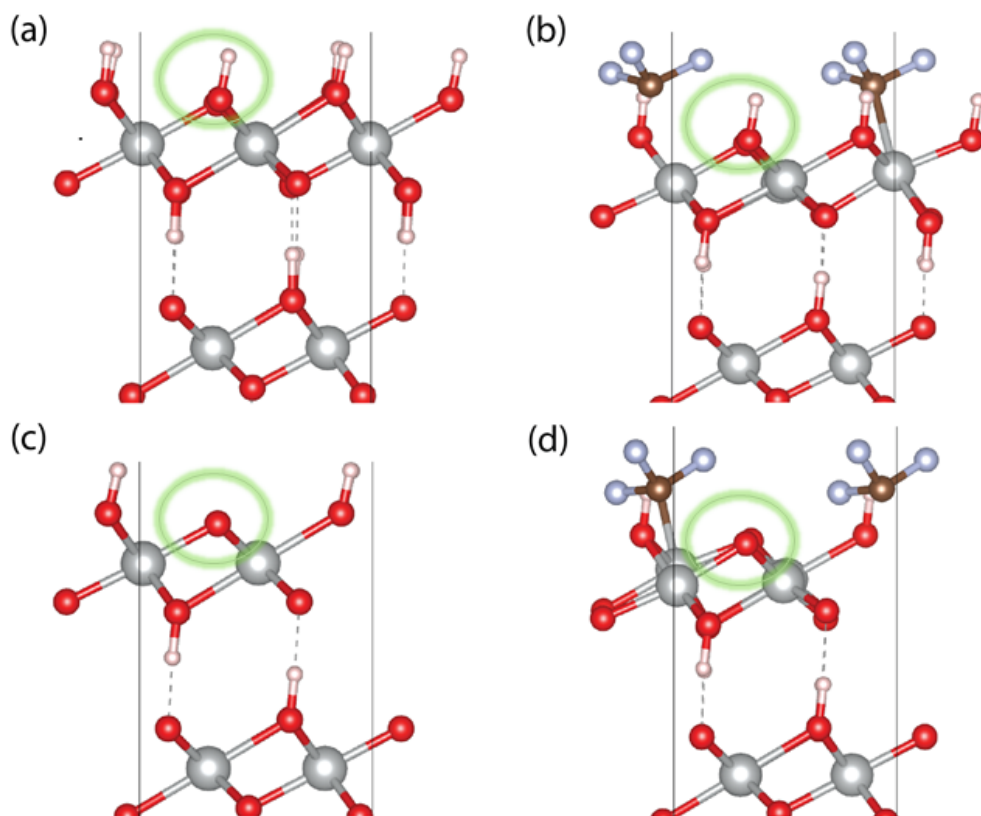
Figure 6.3: β-NiOOH and β-NiOOH-CF3 unit cells with OH* (a-b) and O* (c-d) water oxidation reaction intermediates. The adsorbed intermediates have been highlighted in green circles to guide the readers. Colour code for atoms: O: red; Ni: grey (larger spheres), F: blue; C: brown; H: white. The Ni-C distances for OH* and O* β-NiOOH-CF3 slabs are 2.34 Å and 2.06 Å, respectively.

Based on the recent investigations from Carter et al. [21, 22, 44] we chose the β-NiOOH structure of the catalyst with a staggered arrangement of intercalated protons for the computational investigations. The Perdew-Burke-Ernzerhof (PBE) functional with projector augmented wave (PAW) potentials were used. The DFT+U correction method of Dudarev et al. [19, 45] was employed to improve the known deficiencies of general-

ized gradient approximations (GGA) functionals when describing partially occupied 3d shells. A U-J value of 5.5 eV for Ni(III) was added in combination with the PBE exchange-correlation functional. This value was adapted from the linear response theory calculations of Li and Selloni on β-NiOOH and has been confirmed to lead to accurate replication of electronic and structural properties among other parameter values by Carter et al. [20, 22, 46] To model the PTFE coated catalyst surface, we introduce a Ni-polymer bond in the model via CF_3 fragments which were coordinated to the nickel, by removing a terminating OH group from a Ni site in each unit cell (Figure 6.5 (c)). Some of the possible intermediates of the water oxidation reaction (OH*, O*, and OOH*) [22, 47] were introduced at the coordinatively unsaturated Ni sites for both the β-NiOOH and β-NiOOH-CF_3 unit cells, as shown in Figure 6.3 (a-d). We investigated both atop and bridging binding modes for all intermediates. The bridging mode binding was found to be most stable for all intermediates. The free energy of steps involving the formation of H^+ and e^- were obtained by referencing it to the free energy of H2 using the standard hydrogen electrode (SHE, pH, p = 1 atm, T = 298 K). [48]

We considered step-wise mechanisms releasing ($H^+ + e^-$) pairs for both the $4e^-$ and $2e^-$ pathways. For the $4e^-$ pathway the water oxidation reaction proceeded via OH*, O* and OOH* intermediates forming $O_2(g)$ and $4(H^+ + e^-)$ as the products (eq. 6.27-6.28-6.31-6.32) excluding eq. (6.29,6.30)). [26, 28, 30, 47, 49]

$$* + H_2O(l) \longrightarrow OH^* + H^+ + e^- \tag{6.27}$$

$$OH^* \longrightarrow O^* + (H^+ + e^-) \tag{6.28}$$

$$OH^* + H_2O(l) \longrightarrow H_2O_2 + (H^+ + e^-)^+ * \tag{6.29}$$

$$OH^* + OH^* \longrightarrow H_2O_2 + 2 * \tag{6.30}$$

$$O^* + H_2O(l) \longrightarrow OOH^* + (H^+ + e^-) \tag{6.31}$$

$$OOH^* \longrightarrow O_2 + (H^+ + e^-) + * \tag{6.32}$$
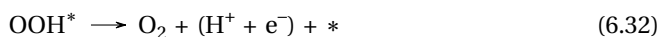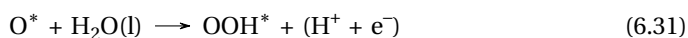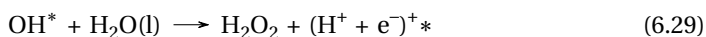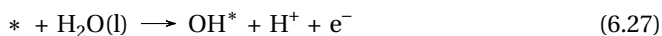
The mechanism for the $2e^-$ pathway consists of eq. 6.27 and eq. 6.29 or 6.30 which results in H_2O_2 as product alongside two pairs of ($H^+ +e^-$). The first step in both mechanisms is the formation of OH* releasing a ($H^+ + e^-$) pair (Figure 6.4 (a)). In the $4e^-$ pathways, a subsequent electrochemical step results in O* species with a second ($H^+ + e^-$) pair (eq. 6.28). Next, the nucleophilic addition of water to O* results in O-O coupling along with the release of a third ($H^+ + e^-$) pair forming the OOH* species (eq. 6.31). The OOH* species forms O_2 (g) product and releases the fourth and final ($H^+ + e^-$) pair (eq. 6.32). In the $2e^-$ pathway the OH* species does not convert to O* but instead undergoes O-O coupling either by a nucleophilic addition to water via eq. 6.29 (Volmer-Heyrovski) or via coupling of two OH* species (eq. 6.30, (Volmer-Tafel) (also see Figure 6.4 (b)).

The results from DFT calculations are presented in the SI. Tables 6.3 and 6.2 in the SI contain the electronic energy, the zero-point energy, thermal corrections, the Gibbs free energies of intermediates, and the ΔG values for elementary steps in the mechanism, The cumulative Gibbs free energy is then plotted and shown in Figure 6.6 in the SI. Compared to the bare surface slab, the binding of OH is destabilized by 0.13 eV for β-NiOOH-CF$_3$ surface. A weakening of OH* Gibbs free energy indicates a shift from the four-electron pathway towards the two-electron route.31,44,45 [24, 28, 50] A Bader charge analysis was also performed on the above systems to investigate the electronic effect of CF$_3$. The results from Bader charge analysis are presented in Table **??** in the SI. The sum of Bader net atomic charges on the OH* complex is zero, as expected for a charge neutral unit cell. For the β-NiOOH-CF$_3$ surface the sum of Bader net atomic charges on all atoms except the CF$_3$ unit is +0.30 indicating the strong electron withdrawing effect of CF$_3$. Further analysis of Bader net atomic charges shows that the OH moiety in OH* is more electropositive by 0.09 units on the β-NiOOH-CF$_3$ surface. This should further facilitate nucleophilic addition of a water molecule forming the H$_2$O$_2$ product via an O-O coupling step (Figure 6.4 (b)), and mitigate immediate further oxidation towards the O* intermediate as in the 4e$^-$ pathway. This is reflected in a $\Delta G_{(OH^* \rightarrow O^*)}$ = 1.38 eV for the β-NiOOH-CF$_3$ surface which is 0.06 eV higher than for the β-NiOOH surface (see Figure 6.6). Therefore, the presence of CF$_3$ units modifies the surface electronic property by a strong electron withdrawing effect and lowers the propensity towards the 4e$^-$ pathway.

6
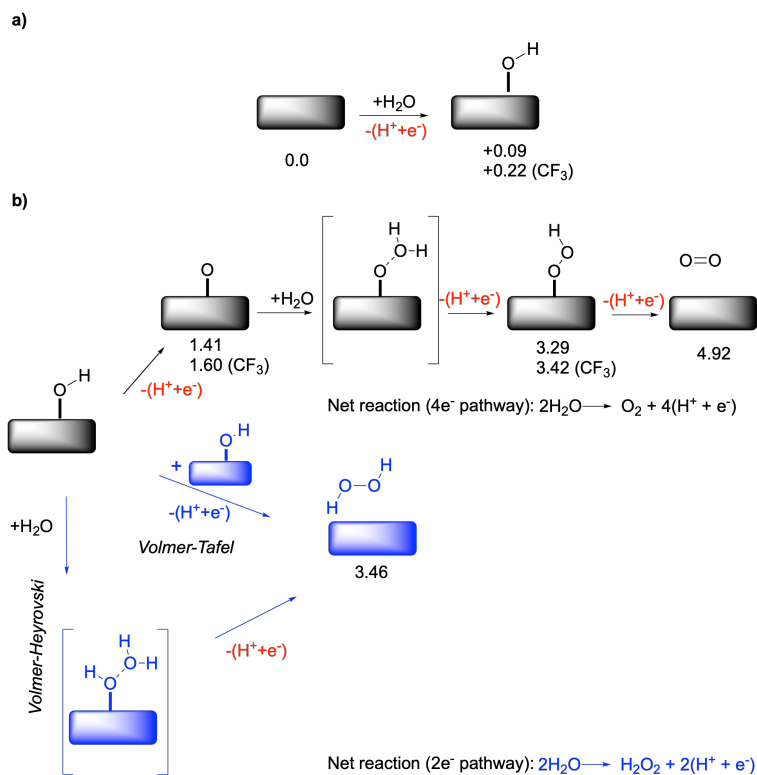
Figure 6.4: (a) Formation of OH* species which is the a descriptor of selectivity for the 4e$^-$ versus the 2e$^-$ pathway for the water oxidation reaction. The DFT computed Gibbs free energy (eV) are shown below for the pristine and the CF$_3$ coated slabs. All the calculations were performed at U = 0 V. b) Further steps in the mechanism leading to O-O coupling and eventual production of O$_2$ or H$_2$O$_2$ via the 4e$^-$ (black) and 2e$^-$ (blue) pathways. For the 2e$^-$ pathway for the Volmer-Tafel and Volmer-Heyrovski mechanisms have been shown. The water adducts shown in the brackets highlight the nucleophilic addition of water to O* (4e$^-$) and OH* (2e$^-$) adducts, and do not necessarily represent the underlying transition states. The computed Gibbs free energy values of the other water oxidation intermediates for the pristine and CF$_3$ coated samples are also shown below the respective slabs.

We note that a OH* binding energy of 0.22 eV, which should ideally be 1.77 eV [28], is still rather low for a highly active and selective material for the 2e⁻ pathway. We have used a rather simple model to mimic the PTFE coating by a chemically bound Ni-CF$_3$ per unit cell. This simplified model already provides qualitative insights into the promoting role of PTFE units towards the selectivity for 2e⁻ pathway. The presence of PTFE coating can also influence the interaction of surface adsorbed intermediates such as OH* with water which can in turn influence the kinetics of H$_2$O$_2$ formation via the Volmer-Heyrovski mechanism. Ni sites that are next to PTFE layer, and sites that are farther away can have different binding affinities to OH*, and can influence the H$_2$O$_2$ production via Volmer-Tafel mechanism. Incorporation of such effects would require a more rigorous computational treatment possibly via (ab initio) molecular dynamics simulations which is beyond the scope of present work. The present model nonetheless captures the molecular effect of the PTFE coating towards promoting the 2e⁻ pathway via an electron withdrawing effect which destabilizes the OH* intermediate. This weakening of the binding energy of the OH* intermediate directly explains the experimentally observed change in selectivity towards the two electron hydrogen peroxide reaction on PTFE coated samples.

In principle, the strategy of modification of the surface electronic character of the electrocatalyst and subsequent tuning of the reaction selectivity, upon polymer loading, can be extended to other electrocatalytic reactions and systems. Even though polymers have previously been used to modify electrocatalysts, by influencing the reaction environment [50, 51], their effect on the electronic properties of the catalyst has not been extensively investigated before. There are several articles in literature that demonstrate different instances where a polymer is bound to an electrocatalyst surface. [52, 53] However, any change in the electrocatalyst performance because of this polymer coating was normally attributed to the catalyst site poisoning due to this polymer binding. Through this work, we show that this polymer binding can induce additional surface electronic changes on the electrocatalyst. A thorough understanding of this concept becomes important with the increased usage of polymer/electrocatalyst interfaces, in the form of ionomer coated catalysts and solid state electrolytes. [18] This is especially important with multi-pathway reactions, like CO$_2$ reduction, where a small change in the surface electronic property can alter the selectivity of different reaction pathways. In the current context, with a careful selection of the polymer, the Ni foam can be made more favourable or less favourable for the four electron water oxidation reaction compared to the two electron formation of hydrogen peroxide.

In this work, we study the modification of the surface electronic property of nickel based water oxidation catalysts upon polymer loading and use it to explain the change in the water oxidation reaction selectivity on PTFE coated Ni foam catalysts. Using XPS, we show that upon coating these catalysts with the PTFE polymer, stable Ni-CF$_x$ bonds are formed at the nickel oxide/PTFE interface. Further using DFT calculations on β-NiOOH and β-NiOOH-CF$_3$ structures we show that, due to the electronegativity of the fluorine atoms, the CF$_3$ group withdraws the electrons from the oxygen atom of the adsorbed OH* intermediate. This electron withdrawing effect of the CF$_3$ group weakens the bind-

ing energy of the OH* intermediate and makes it more difficult to form the adsorbed O* intermediate. The weakening of the OH* intermediate makes it easier to take the two-electron pathway to H_2O_2, while the increased energy requirement to form the O* intermediate suppresses the four electron pathway to oxygen. Therefore, this dual effect of favourable H_2O_2 formation and suppressed OER pathway on PTFE modified water oxidation catalysts explains the experimentally observed selectivity difference. In principle, this approach of tuning the electronic property of electrocatalysts with polymers with electron withdrawing/donating character can be extended to other heterogeneous electrochemical systems.

6

6.4. Supplementary information

Electrochemical measurements

The pristine and PTFE coated Ni foam were tested in an H-cell with 1 M K_2CO_3 as the electrolyte. The polarisation curves for each are shown in Figure 6.1 (a). Two key differences can be observed here. First, the performance of the PTFE coated Ni foam electrode is inferior to the pristine Ni foam electrode. This is a result of the passivation of the active sites in the Ni foam by the insulating PTFE. As a result, the electrochemically active surface area is less on the PTFE coated Ni foam in comparison to the pristine Ni foam electrodes. This was also observed by Xia et al. [17] with their PTFE coated Carbon Fiber Paper (CFP) electrodes. The second key difference is in the delay of the onset potential for the PTFE coated Ni foam electrode. This is clear when looking at the magnified image of the polarisation curves, as shown in Figure 6.1 (b). The delayed onset potential of the PTFE coated electrode is an indication of a higher overpotential for the thermodynamically favourable water oxidation reaction, i.e., the four electron water oxidation to oxygen. This higher overpotential suggests that the PTFE modification has made the Ni foam less active towards the oxygen evolution reaction. The redox wave pertaining to the potential induced transition of Ni^{2+} to Ni^{3+} is also visible in the voltammogram in Figure 6.1 (a).

Next the electrodes were tested for its selectivity towards the two electron water oxidation reaction to hydrogen peroxide. A chronoamperometry was performed until a fixed amount of charge was passed through the setu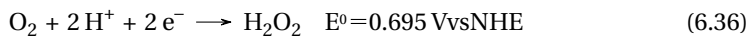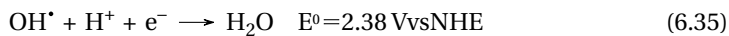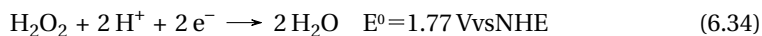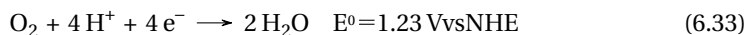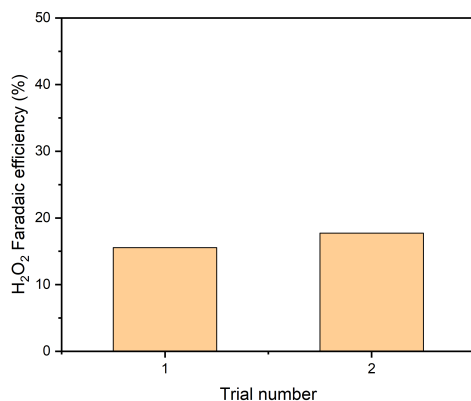p and the hydrogen peroxide produced at the anode was quantified using permanganate titration. The hydrogen peroxide faradaic efficiency of the pristine and the PTFE coated Ni foam electrode are shown in Figure 6.1 (c). As expected, the faradaic efficiency towards hydrogen peroxide by the PTFE coated Ni foam electrode was higher compared to the pristine Ni foam electrode, agreeing with the work of Xia et al.1 [17], suggesting that the PTFE modification has indeed altered the selectivity of the water oxidation reaction. We noticed a faster decrease of this faradaic efficiency over time compared to the work of Xia et al., as shown in Figure 6.1 (d). This is due to the higher surface area of the electrodes (3.14 cm^2) used in our work, compared to the work of Xia et al. (0.42 cm^2) as well as the lower amount of anolyte in our H cell compared to that of Xia et al. Higher surface area and higher concentrations of hydrogen peroxide will lead to the accelerated degradation of the hydrogen peroxide via its oxidation at the anode, as shown in equation 6.36. This oxidative decay of the hydrogen peroxide to oxygen with time, the oxygen bubble trapping nature of the porous structure of the Ni foam and the aerophilic character of the PTFE makes the oxygen gas quantification unreliable and hence is not presented here. To confirm that the decay observed here is from the hydrogen peroxide degradation and not the sample itself, we performed repeat experiments on the same sample by replacing the electrolyte. As shown in Figure 6.2, similar hydrogen peroxide faradaic efficiency was recovered by performing the electrolysis with a fresh electrolyte, confirming that it is indeed the hydrogen peroxide degradation that is resulting in drop in faradaic efficiency with time. For best results, it would be ideal to minimize the residence time of the hydrogen peroxide in the anodic chamber either by using a flow cell or through other approaches.
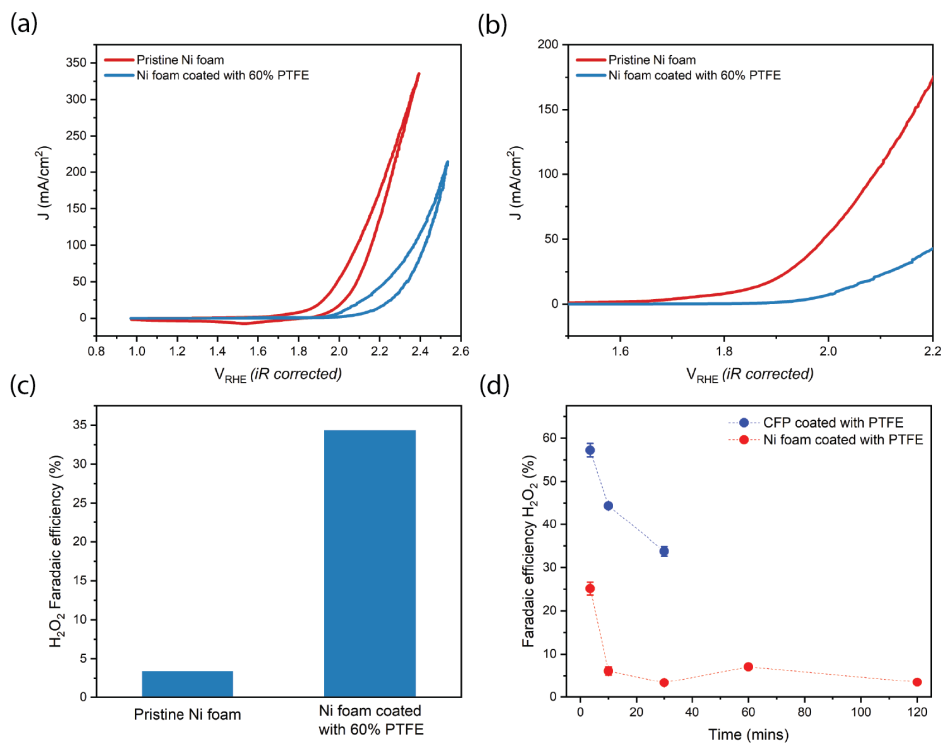
Supplementary Figure S6.1: (a) Cyclic voltammetries of the pristine and PTFE coated nickel foam in 1M K_2CO_3. (b) Zoomed in image of this cyclic voltammetry showing the delayed onset potential of water oxidation in PTFE coated nickel foam electrode. (c) Plot showing the improved faradaic efficiency towards H_2O_2 on the PTFE coated nickel foam electrode. (d) Degradation of the H_2O_2 faradaic efficiency over time on PTFE coated nickel and CFP electrodes.

$$O_2 + 4\,H^+ + 4\,e^- \longrightarrow 2\,H_2O \quad E^0 = 1.23\,V\,vs\,NHE \tag{6.33}$$

$$H_2O_2 + 2\,H^+ + 2\,e^- \longrightarrow 2\,H_2O \quad E^0 = 1.77\,V\,vs\,NHE \tag{6.34}$$

$$OH^\bullet + H^+ + e^- \longrightarrow H_2O \quad E^0 = 2.38\,V\,vs\,NHE \tag{6.35}$$

$$O_2 + 2\,H^+ + 2\,e^- \longrightarrow H_2O_2 \quad E^0 = 0.695\,V\,vs\,NHE \tag{6.36}$$

Supplementary Figure S6.2: Repeat chronoampherometric tests on the same sample, with fresh electrolyte, shows that similar faradic efficiencies can be regained. This again suggests that the drop in faradic efficiency seen earlier is through H_2O_2 degradation at the anode and not because of sample degradation.

6
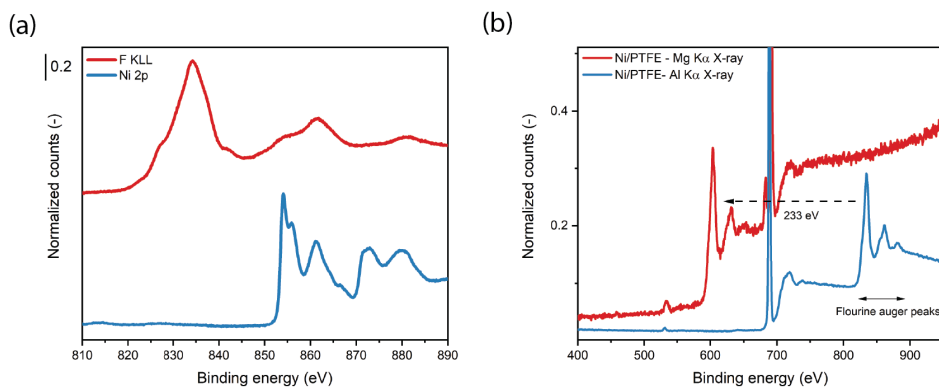
Supplementary Figure S6.3: (a) Ni2p core electron and F KLL auger emission spectra acquired using an XPS system with Al Kα X-ray source, showing their obvious overlap. (b) Survey spectra of the PTFE coated Ni foam samples using XPS systems with Al Kα (1486.6 eV) and Mg Kα (1253.6 eV) X-ray sources. As shown in the figure, the F KLL auger emission spectra is shifted to lower binding energies when using a Mg Kα X-ray source, by a factor equalling the difference between the X-ray energies.
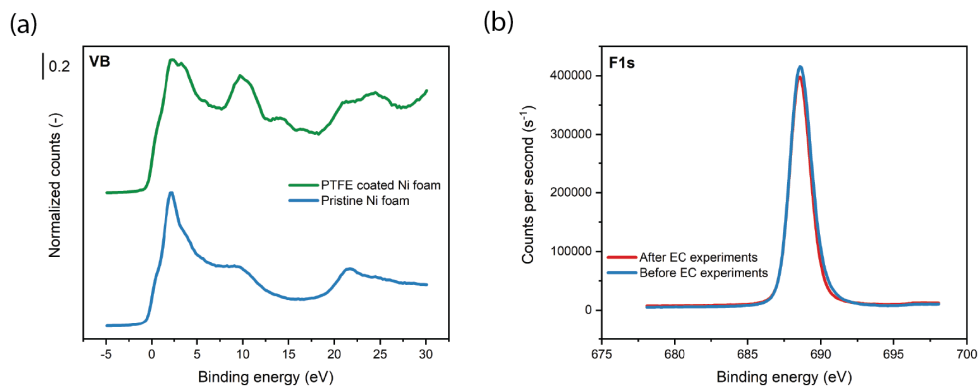
Supplementary Figure S6.4: (a) Valence band XPS spectra of the pristine and PTFE coated Ni foam electrodes. (b) F1s core electron spectra of the PTFE coated Ni foam electrode before and after electrochemical experiments, again showing the PTFE coating was stable during the electrochemical experiments.

6
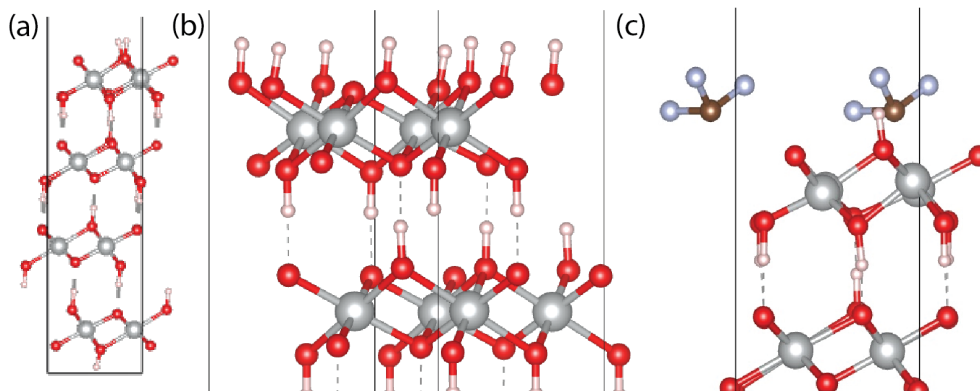
Supplementary Figure S6.5: (a-b) Relaxed β-NiOOH unit cells used in this work (c) Relaxed β-NiOOH-CF$_3$ unit cells used in this work

Table 6.1: Values of the zero-point energies, enthalpic, and entropic contributions for the OER

		Ref ZPE (eV)	H (eV)	TS (eV)	Total correction (eV)
β-NiOOH	H2O*	2.18	0.04	0.05	2.17
	OH*	1.85	0.09	0.13	1.82
	O*	1.64	0.08	0.11	1.61
β-NiOOH-CF3	H2O*	2.21	0.07	0.09	2.19
	OH*	1.84	0.08	0.11	1.82
	O*	1.59	0.09	0.12	1.56
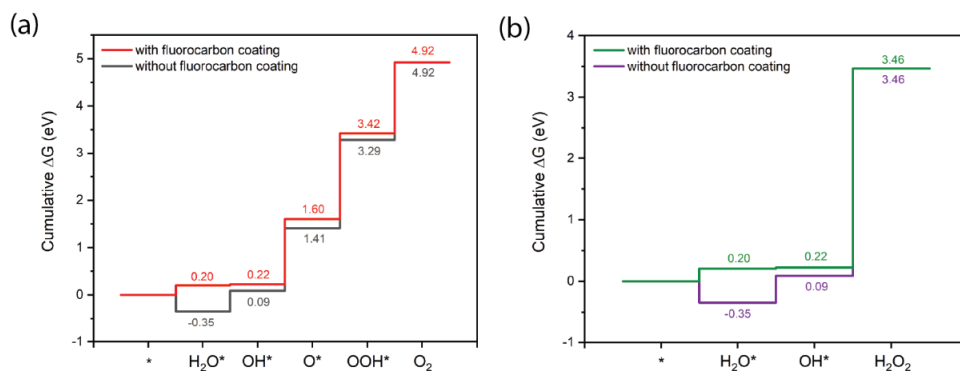
Supplementary Figure S6.6: (a) Cumulative free energy profile for the four electron water oxidation reaction to oxygen for β-NiOOH and β-NiOOH-CF$_3$ unit cells (associate pathway) (b) Cumulative free energy profile for the two electron water oxidation reaction to hydrogen peroxide for β-NiOOH and β-NiOOH-CF$_3$ unit cells (Volmer Heyrovski pathway)

6

Table 6.2: Mechanism reaction energetics on the NiOOH surface. (Reaction free energies include the ZPE and thermal energy corrections.)

		Reaction energies (eV)	Reaction free energies (eV)
H_2O/H_2O^* without CF_3	$H_2O + * \longrightarrow H_2O^*$	-0.86	-0.35
H_2O/H_2O^* with CF_3		-0.64	0.20
H_2O^*/OH^* without CF_3	$H_2O^* \longrightarrow OH^* + (H^+ + e^-)$	0.85	0.43
H_2O^*/OH^* with CF_3		0.47	0.02
OH^*/O^* without CF_3	$OH^* \longrightarrow O^* + (H^+ + e^-)$	1.60	1.32
OH^*/O^* with CF_3		1.70	1.37
O^*/OOH^* without CF_3	$O^* + H_2O \longrightarrow OOH^* + (H^+ + e^-)$	1.60	1.88
$O^*/O0H^*$ with CF_3		1.50	1.82
OOH^*/O_2 without CF_3	$OOH^* \longrightarrow O_2 + * + (H^+ + e^-)$	1.72	1.63
OOH^*/O_2 with CF_3		1.88	1.50

Table 6.3: Values of the zero-point energies, enthalpic, and entropic contributions for the OER

NiOOH-OH		NiOOH-OH-CF3	
	Bader net atomic charge		Bader net atomic charge
Ni	1.241	Ni	0.85
Ni	1.199	Ni	1.338
Ni	1.084	Ni	1.349
Ni	1.206	Ni	1.015
Ni	1.231	Ni	0.838
Ni	1.183	Ni	1.331
Ni	1.079	Ni	1.362
Ni	1.142	Ni	1.132
Ni	1.149	Ni	1.279
Ni	1.882	Ni	1.401
Ni	1.121	Ni	1.101
Ni	1.254	Ni	1.231
Ni	1.135	Ni	1.294
Ni	1.403	Ni	1.428
Ni	0.851	Ni	1.137
Ni	1.252	Ni	1.235
O	-0.659	O	-0.784
O	-0.644	O	-0.631
O	-0.743	O	-0.633
O	-0.72	O	-0.732
O	-0.639	O	-0.811
O	-0.641	O	-0.676
O	-0.747	O	-0.627
O	-0.716	O	-0.748
O	-0.569	O	-0.755
O	-0.823	O	-0.615
O	-0.751	O	-0.685
O	-0.749	O	-0.584
O	-0.739	O	-0.684
O	-0.742	O	-0.574
O	-0.779	O	-0.746
O	-0.622	O	-0.616
O	-0.711	O	-0.503
O	-1.006	O	-0.697

6

NiOOH-OH Bader net atomic charge		NiOOH-OH-CF3 Bader net atomic charge	
cont..		cont..	
O	-0.625	O	-0.698
O	-0.741	O	-0.63
O	-0.651	O	-0.508
O	-0.986	O	-0.712
O	-0.648	O	-0.68
O	-0.494	O	-0.678
O	-0.746	O	-0.685
O	-0.667	O	-0.753
O	-0.696	O	-0.777
O	-0.659	O	-0.674
O	-0.755	O	-0.693
O	-0.659	O	-0.74
O	-0.758	O	-0.769
O	-5.708	H	0.06
H	0.164	H	0.23
H	0.501	H	0.155
H	0.097	H	0.103
H	0.038	H	0.126
H	0.079	H	0.229
H	0.502	H	0.165
H	0.09	H	0.074
H	0.098	H	0.189
H	0.183	H	0.178
H	0.328	H	0.15
H	0.264	H	-0.042
H	0.191	H	0.157
H	0.254	H	-0.076
H	0.168	H	0.166
H	0.174	H	0.208
H	0.118	C	1.235
H	0.131	F	-0.511
		F	-0.402
		F	-0.618

6.5. References

(1) Venugopal, A.; Egberts, L. H. T.; Meeprasert, J.; Pidko, E. A.; Dam, B.; Burdyny, T.; Sinha, V.; Smith, W. A. *ACS Energy Letters* **2022**, *7*, 1586–1593.

(2) Perry, S. C.; Pangotra, D.; Vieira, L.; Csepei, L. I.; Sieber, V.; Wang, L.; Ponce de León, C.; Walsh, F. C. *Nature Reviews Chemistry* **2019**, *3*, 442–458.

(3) Salmon, N.; Bañares-Alcántara, R. *Sustainable Energy and Fuels* **2021**, *5*, 2814–2839.

(4) Tremel, A.; Wasserscheid, P.; Baldauf, M.; Hammer, T. *International Journal of Hydrogen Energy* **2015**, *40*, 11457–11464.

(5) Kondratenko, E. V.; Mul, G.; Baltrusaitis, J.; Larrazábal, G. O.; Pérez-Ramírez, J. *Energy and Environmental Science* **2013**, *6*, 3112–3135.

(6) Ooka, H.; Huang, J.; Exner, K. S. *Frontiers in Energy Research* **2021**, *9*, 1–20.

(7) Medford, A. J.; Vojvodic, A.; Hummelshøj, J. S.; Voss, J.; Abild-Pedersen, F.; Studt, F.; Bligaard, T.; Nilsson, A.; Nørskov, J. K. *Journal of Catalysis* **2015**, *328*, 36–42.

(8) Zhong, M. et al. *Nature* **2020**, *581*, 178–183.

(9) Li, Z.; Achenie, L. E.; Xin, H. *ACS Catalysis* **2020**, *10*, 4377–4384.

(10) Mistry, H.; Varela, A. S.; Kühl, S.; Strasser, P.; Cuenya, B. R. *Nature Reviews Materials* **2016**, *1*, 1–14.

(11) Guntern, Y. T.; Okatenko, V.; Pankhurst, J.; Varandili, S. B.; Iyengar, P.; Koolen, C.; Stoian, D.; Vavra, J.; Buonsanti, R. *ACS Catalysis* **2021**, *11*, 1248–1295.

(12) Wanjala, B. N.; Luo, J.; Loukrakpam, R.; Fang, B.; Mott, D.; Njoki, P. N.; Engelhard, M.; Naslund, H. R.; Wu, J. K.; Wang, L.; Malis, O.; Zhong, C. J. *Chemistry of Materials* **2010**, *22*, 4282–4294.

(13) Liao, H.; Fisher, A.; Xu, Z. J. *Small* **2015**, *11*, 3221–3246.

(14) Kuai, C.; Xu, Z.; Xi, C.; Hu, A.; Yang, Z.; Zhang, Y.; Sun, C. J.; Li, L.; Sokaras, D.; Dong, C.; Qiao, S. Z.; Du, X. W.; Lin, F. *Nature Catalysis* **2020**, *3*, 743–753.

(15) Nugroho, F. A.; Darmadi, I.; Cusinato, L.; Susarrey-Arce, A.; Schreuders, H.; Bannenberg, L. J.; da Silva Fanta, A. B.; Kadkhodazadeh, S.; Wagner, J. B.; Antosiewicz, T. J.; Hellman, A.; Zhdanov, V. P.; Dam, B.; Langhammer, C. *Nature Materials* **2019**, *18*, 489–495.

(16) Ngene, P.; Westerwaal, R. J.; Sachdeva, S.; Haije, W.; de Smet, L. C. P. M.; Dam, B. *Angewandte Chemie* **2014**, *126*, 12277–12281.

(17) Xia, C.; Back, S.; Ringe, S.; Jiang, K.; Chen, F.; Sun, X.; Siahrostami, S.; Chan, K.; Wang, H. *Nature Catalysis* **2020**, *3*, 125–134.

(18) García de Arquer, F. P. et al. *Science* **2020**, *367*, 661–666.

(19) Dudarev, S.; Botton, G. *Physical Review B - Condensed Matter and Materials Physics* **1998**, *57*, 1505–1509.

(20) Li, Y. F.; Selloni, A. *ACS Catalysis* **2014**, *4*, 1148–1153.

6

(21) Tkalych, A. J.; Yu, K.; Carter, E. A. *Journal of Physical Chemistry C* **2015**, *119*, 24315–24322.

(22) Tkalych, A. J.; Zhuang, H. L.; Carter, E. A. *ACS Catalysis* **2017**, *7*, 5329–5339.

(23) Rossmeisl, J.; Logadottir, A.; Nørskov, J. K. *Chemical Physics* **2005**, *319*, 178–184.

(24) Siahrostami, S.; Li, G. L.; Viswanathan, V.; Nørskov, J. K. *Journal of Physical Chemistry Letters* **2017**, *8*, 1157–1160.

(25) Shi, X.; Siahrostami, S.; Li, G. L.; Zhang, Y.; Chakthranont, P.; Studt, F.; Jaramillo, T. F.; Zheng, X.; Nørskov, J. K. *Nature Communications* **2017**, *8*, 6–11.

(26) Dickens, C. F.; Kirk, C.; Nørskov, J. K. *Journal of Physical Chemistry C* **2019**, *123*, 18960–18977.

(27) Gerrits, N.; Smeets, E. W. F.; Vuckovic, S.; Powell, A. D.; Doblhoff-Dier, K.; Kroes, G.-J. *The Journal of Physical Chemistry Letters* **2020**, *11*, 10552–10560.

(28) Viswanathan, V.; Hansen, H. A.; Nørskov, J. K. *Journal of Physical Chemistry Letters* **2015**, *6*, 4224–4228.

(29) Nadar, A.; Gupta, S. S.; Kar, Y.; Shetty, S.; Van Bavel, A. P.; Khushalani, D. *Journal of Physical Chemistry C* **2020**, *124*, 4152–4161.

(30) Liao, P.; Keith, J. A.; Carter, E. A. *Journal of the American Chemical Society* **2012**, *134*, 13296–13309.

(31) Valdes, A.; Qu, Z. W.; Kroes, G. J.; Rossmeisl, J.; Nørskov, J. K. *J. Phys. Chem. C.* **2008**, *112*, 9872–9879.

(32) Man, I. C.; Su, H. Y.; Calle-Vallejo, F.; Hansen, H. A.; Martínez, J. I.; Inoglu, N. G.; Kitchin, J.; Jaramillo, T. F.; Nørskov, J. K.; Rossmeisl, J. *ChemCatChem* **2011**, *3*, 1159–1165.

(33) Tang, W.; Sanville, E.; Henkelman, G. *Journal of Physics: Condensed Matter* **2009**, *21*, 084204.

(34) Flege, J. I.; Meyer, A.; Falta, J.; Krasovskii, E. E. *Physical Review B - Condensed Matter and Materials Physics* **2011**, *84*, 1–10.

(35) Preda, I.; Gutiérrez, A.; Abbate, M.; Yubero, F.; Méndez, J.; Alvarez, L.; Soriano, L. *Physical Review B - Condensed Matter and Materials Physics* **2008**, *77*, 1–7.

(36) Grosvenor, A. P.; Biesinger, M. C.; Smart, R. S. C.; McIntyre, N. S. *Surface Science* **2006**, *600*, 1771–1779.

(37) Hüfner, S., *Photoelectron Spectroscopy : Principles and Applications*; Springer: 2003, pp 109–124.

(38) Nesbitt, H. W.; Legrand, D.; Bancroft, G. M. *Physics and Chemistry of Minerals* **2000**, *27*, 357–366.

(39) Grim, S. O.; Swartz, W. E.; Matienzo, L. J.; Yin, I. *Inorganic Chemistry* **1973**, *12*, 2762–2769.

(40) Benayad, A.; Li, X. S. *Journal of Physical Chemistry C* **2013**, *117*, 4727–4733.

(41) Sarawutanukul, S.; Phattharasupakun, N.; Wutthiprom, J.; Sawangphruk, M. *Sustainable Energy and Fuels* **2018**, *2*, 1305–1311.

(42) Lewin, E.; André, B.; Urbonaite, S.; Wiklund, U.; Jansson, U. *Journal of Materials Chemistry* **2010**, *20*, 5950–5960.

(43) Li, L.; Jones, P. M.; Hsia, Y. T. *Applied Surface Science* **2011**, *257*, 4478–4485.

(44) Martirez, J. M. P.; Carter, E. A. *Chemistry of Materials* **2018**, *30*, 5205–5219.

(45) Tolba, S. A.; Gameel, K. M.; Ali, B. A.; Almossalami, H. A.; Allam, N. K. In *Density Functional Calculations - Recent Progresses of Theory and Application*; InTech: 2018, pp 4–30.

(46) Cococcioni, M.; De Gironcoli, S. *Physical Review B - Condensed Matter and Materials Physics* **2005**, *71*, 1–16.

(47) Sinha, V.; Sun, D.; Meijer, E. J.; Vlugt, T. J.; Bieberle-Hutter, A. *Faraday Discussions* **2021**, *229*, 89–107.

(48) Nørskov, J. K.; Rossmeisl, J.; Logadottir, A.; Lindqvist, L.; Kitchin, J. R.; Bligaard, T.; Jónsson, H. *Journal of Physical Chemistry B* **2004**, *108*, 17886–17892.

(49) Wang, R. B.; Hellman, A. *Journal of Physical Chemistry C* **2019**, *123*, 2820–2827.

(50) Lee, J. H.; Doo, G.; Kwon, S. H.; Kang, H.; Choi, S.; Yim, S. D.; Kim, H. T.; Lee, S. G. *ACS Applied Polymer Materials* **2020**, *2*, 1807–1818.

(51) Ott, S.; Orfanidi, A.; Schmies, H.; Anke, B.; Nong, H. N.; Hübner, J.; Gernert, U.; Gliech, M.; Lerch, M.; Strasser, P. *Nature Materials* **2020**, *19*, 77–85.

(52) Safo, I. A.; Dosche, C.; Özaslan, M. *ChemPhysChem* **2019**, *20*, 3010–3023.

(53) Tymoczko, J.; Calle-Vallejo, F.; Colic, V.; Koper, M. T.; Schuhmann, W.; Bandarenka, A. S. *ACS Catalysis* **2014**, *4*, 3772–3778.

6

Summary

Climate change, due to the continued emissions of carbon dioxide into our atmosphere and subsequent warming of the planet, is an existential crisis facing humanity. The rising temperature is are resulting in the melting of our ice caps and glaciers, influencing the weather patterns, are making many parts of the world unliveable and are driving many species into extinction. If the current trend is continued, catastrophic and irreversible effects to our planet is almost guaranteed. To tackle this issue, we need to immediately find a viable replacement for the carbon emitting fossil fuels currently used in our energy, transportation and chemical infrastructures. Moving to renewable energy sources like wind and solar energy is already proving to be the answer to this problem. However, in-order to scale the use of these non-emitting sustainable energy sources rapidly, some of the issues associated with these sources like the intermittency and the heavy reliance of fossil fuels in the hard to electrify sectors need to be dealt with.

Electrochemistry can offer various solutions here. Using electrochemistry, we can convert electrical energy to chemical energy and vice versa. This way, we can synthesize chemicals that can be easily stored in large quantities and can be converted back to electricity when required. We can also use electrochemistry to make chemical building blocks that can be used to replace the existing fossil based chemical building blocks or make chemicals that can decarbonize the hard to electrify sectors. In order for these electrochemical technologies to be economically competitive with fossil fuel technologies, the cost of electrochemical synthesis needs to drastically decrease. Therefore, further innovations are required to drastically decrease the capital and operational costs of electrolysis. One such innovative approach to potentially decrease the capital and operating cost is the concept of a photoelectrochemical system, which is an integrated system where one of the electrodes in the water electrolyzer is a photo-absorbing semiconductor to integrate capture and utilization of the solar energy. Such devices have already been demonstrated at a small scale. However, to practically scale-up this technology, such systems should offer long term stabilities. To develop stable systems, it is important to understand different degradation mechanisms at the semiconductor/electrolyte interface. In this thesis, we study this interface extensively and offer new insights into the degradation mechanisms.

The thesis builds on the photocharging of $BiVO_4$ photoanodes that was introduced by our research group back in 2016. It was first introduced as a performance improvement strategy, where the performance of $BiVO_4$ photoanodes improved multi-fold when subjected to prolonged illumination under open-circuit conditions. It was shown that most of the changes observed where at the photoanode surface while the bulk photoanode remained intact. At the start of this thesis, we investigated other photoanode materials to if this effect was unique to $BiVO_4$ photoanodes or if it was common to other materials. $CuWO_4$ photoanodes were tested and studied, to observe its response to the

photocharging treatment. It was demonstrated that the response of the $CuWO_4$ photoanodes was fairly similar to that of $BiVO_4$ photoanodes, suggesting the possibility of a common mechanism. In parallel, other research groups demonstrated the same effect on other metal oxides photoelectrodes, reiterating the suggestion of a common mechanism.

In subsequent works, more characterisation techniques were developed and used to study this phenomenon. $BiVO_4$ photoanodes were chosen for these studies as the model system. Grazing incidence X-ray Raman Scattering technique was used to study the effect of the photocharging treatment on the space charge region of $BiVO_4$. It was shown that the photocharged $BiVO_4$ photoanodes had an improved band bending in this region. It was speculated that the photocharging treatment resulted in the formation of a bismuth borate surface layer, which resulted in a $BiVO_4$ / bismuth borate hetero-junction near the photoelectrode surface post photocharging. This hetero-junction resulted in the improved band bending, which improved the charge separation within the space charge region. This improved charge separation was the reason for the improved photoelectrochemical performance.

To understand this phenomenon better, in a subsequent work, a novel operando photoelectrochemical infrared spectroscopy setup was constructed to study the photocharging process. The infrared spectra was followed during the process of photocharging, which revealed the slow dissolution of the vanadium species from the photoelectrode surface during the photocharging process. This slow dissolution of vanadium altered the Bi:V composition at the surface of the $BiVO_4$ photoanode, making it bismuth rich. An increase in the concentration of anions like hydroxyl ions and borate ions were also observed in the infrared spectra, during the photocharging treatment. The formation of the bismuth rich surface, would reiterate the story of the formation of heterojunction during photocharging. It was previously shown that a bismuth rich $BiVO_4$ has higher band positions compared to $BiVO_4$ with equimolar ratio of Bi:V. This would suggest that the resultant heterojunction between bulk $BiVO_4$ and the bismuth rich $BiVO_4$ will have an improved band bending, confirming the observation from the X-ray Raman Scattering studies. The infrared spectroscopy results gives sufficient proof that the photocharging is a temporary performance enhancement phenomenon resulting from the degradation of the photoelectrode under illuminated conditions.

The operando infrared spectroscopy and other characterisation studies suggest that the simultaneous exposure of the cation and the anion species of the photoelectrode to the oxidative and reductive environment within the photoelectrode is the cause of this degradation phenomenon. This simultaneous existence of a oxidative and reductive environment within an electrode is unique to photoelectrodes and so is this degradation mechanism. The redox cycling of the surface cation-anion species within the photoelectrodes have been discussed before in the context of "surface recombination" of charge carriers. Here, this concept was only discussed from the perspective of its impact on the device efficiency. With the work done within this thesis, we provide enough proof to suggest that the surface recombination phenomenon is also a degradation mechanism for

photoelectrodes. The authors also discuss the implication of this, within this thesis. It is suggested that this degradation mechanism will be difficult to prevent from a material perspective. The only work around might be to "minimize" its impact by choosing the right photoelectrode-system configurations.

With regard to the general theme of decreasing the capital and operating costs of electrochemical systems, the thesis also explores the use of alternative ways to tailor the electronic properties of electrocatalysts. Having the ability to selectively tune the electronic property of a catalyst surface has many advantages, which includes potentially decreasing the capital and operating costs. Within this context, the authors provide new insights into the effect of polymer loading on electrocatalysts. With a combined experimental and computational approach, it is shown that when common water oxidation catalysts like nickel is coated with polymers like polytetrafluoroethylene, a Ni-CF$_x$ bond is produced at the electrocatalyst/polymer interface. The electron withdrawing property of this CF$_x$ group will then alter the electron density of the neighbouring nickel species, altering the activity and selectivity of these catalytic sites. The authors suggest that, this concept of polymer loading of electrocatalysts could be a new way to tune the electronic properties of electrocatalysts. This concept also becomes increasingly relevant with the increased usage of ionomers and catalyst coated membrane electrode assemblies, where the catalyst is in direct contact with polymers like in the system studied above.

6

Samenvatting

Klimaatverandering, als gevolg van de aanhoudende uitstoot van koolstofdioxide in onze atmosfeer en de daaropvolgende opwarming van de planeet, is een existentiële crisis waarmee de mensheid wordt geconfronteerd. De stijgende temperaturen leiden tot het smelten van onze ijskappen en gletsjers, beïnvloeden de weerpatronen, maken veel delen van de wereld onleefbaar en bedreigen veel soorten met uitsterven. Als de huidige trend zich doorzet, zijn catastrofale en onomkeerbare gevolgen voor onze planeet bijna gegarandeerd. Om dit probleem aan te pakken, moeten we onmiddellijk een levensvatbare vervanging vinden voor de CO2-uitstotende fossiele brandstoffen die momenteel worden gebruikt in onze energie-, transport- en chemische infrastructuur. Overstappen op hernieuwbare energiebronnen zoals wind- en zonne-energie blijkt nu al het antwoord op dit probleem te zijn. Om het gebruik van deze niet-emitterende duurzame energiebronnen echter snel op te schalen, moeten enkele van de problemen die met deze bronnen samenhangen, zoals de intermitterende en de grote afhankelijkheid van fossiele brandstoffen in de moeilijk te elektrificeren sectoren worden aangepakt.

Elektrochemie kan hier verschillende oplossingen bieden. Met behulp van elektrochemie kunnen we elektrische energie omzetten in chemische energie en omgekeerd. Op deze manier kunnen we chemicaliën synthetiseren die gemakkelijk in grote hoeveelheden kunnen worden opgeslagen en indien nodig weer kunnen worden omgezet in elektriciteit. We kunnen ook elektrochemie gebruiken om chemische bouwstenen te maken die kunnen worden gebruikt om de bestaande op fossielen gebaseerde chemische bouwstenen te vervangen of om chemicaliën te maken die de moeilijk te elektrificeren sectoren koolstofvrij kunnen maken. Om ervoor te zorgen dat deze elektrochemische technologieën economisch concurrerend zijn met fossiele brandstoftechnologieën, moeten de kosten van elektrochemische synthese drastisch dalen. Daarom zijn verdere innovaties nodig om de kapitaal- en operationele kosten van elektrolyse drastisch te verlagen.

Een van die innovatieve benaderingen om de kapitaal en bedrijfskosten mogelijk te verlagen, is het concept van een foto-elektrochemisch systeem. Dit is een geïntegreerd systeem waarbij een van de elektroden in de waterelektrolyser een foto-absorberende halfgeleider is om de opname en het gebruik van de zonne-energie te integreren. energie. Dergelijke apparaten zijn al op kleine schaal gedemonstreerd. Om deze technologie praktisch op te schalen, moeten dergelijke systemen echter stabiliteit op lange termijn bieden. Om stabiele systemen te ontwikkelen, is het belangrijk om verschillende degradatiemechanismen op de halfgeleider/elektrolyt-interface te begrijpen. In dit proefschrift bestuderen we deze interface uitgebreid en bieden we nieuwe inzichten in de degradatiemechanismen. Het proefschrift bouwt voort op de foto-oplading van $BiVO_4$-fotoanodes die in 2016 door de groep werd geïntroduceerd. Het werd voor het eerst geïntroduceerd als een prestatieverbeteringsstrategie, waarbij de prestaties van $BiVO_4$

fotoanodes meervoudig verbeterden bij blootstelling aan langdurige verlichting onder open circuit-omstandigheden. Er werd aangetoond dat de meeste waargenomen veranderingen zich aan het oppervlak van de fotoanode bevonden, terwijl de bulkfotoanode intact bleef. Aan het begin van dit proefschrift hebben we andere fotoanodematerialen onderzocht om te kijken of dit effect uniek was voor $BiVO_4$ fotoanodes of dat het gebruikelijk was voor andere materialen. $CuWO_4$ fotoanodes werden getest en bestudeerd om de reactie op de foto-oplaadbehandeling te observeren. Er werd aangetoond dat de respons van de $CuWO_4$ fotoanodes redelijk vergelijkbaar was met die van $BiVO_4$ fotoanodes, wat de mogelijkheid van een gemeenschappelijk mechanisme suggereert. Tegelijkertijd toonden andere onderzoeksgroepen hetzelfde effect aan op andere foto-elektroden van metaaloxiden, waarbij de suggestie van een gemeenschappelijk mechanisme werd herhaald.

In latere werken werden meer karakteriseringstechnieken ontwikkeld en gebruikt om dit fenomeen te bestuderen. $BiVO_4$ fotoanodes werden voor deze studies gekozen als modelsysteem. Grazing incidence X-ray Raman Scattering-techniek werd gebruikt om het effect van de fotoladingsbehandeling op het ruimteladingsgebied van $BiVO_4$ te bestuderen. Er werd aangetoond dat de foto-geladen $BiVO_4$ fotoanodes in dit gebied een verbeterde bandbuiging hadden. Er werd gespeculeerd dat de foto-opladingsbehandeling resulteerde in de vorming van een bismutboraat-oppervlaktelaag, wat resulteerde in een $BiVO_4$/bismut boraat hetero-overgang nabij het foto-elektrode-oppervlak na foto-oplading. Deze hetero-junctie resulteerde in de verbeterde bandbuiging, die de ladingsscheiding binnen het ruimteladingsgebied verbeterde. Deze verbeterde ladingsscheiding was de reden voor de verbeterde foto-elektrochemische prestatie.

Om dit fenomeen beter te begrijpen, werd in een volgend werk een nieuwe operando foto-elektrochemische infraroodspectroscopie-opstelling geconstrueerd om het fotolaadproces te bestuderen. De infraroodspectra werden gevolgd tijdens het fotoladen, wat de langzame oplossing van de vanadiumsoorten van het foto-elektrodeoppervlak tijdens het fotolaadproces onthulde. Deze langzame oplossing van vanadium veranderde de Bi:V-samenstelling aan het oppervlak van de $BiVO_4$ fotoanode, waardoor deze rijk werd aan bismut. Een toename van de concentratie van anionen zoals hydroxylionen en boraationen werd ook waargenomen in de infraroodspectra tijdens de foto-oplaadbehandeling. De vorming van het bismutrijke oppervlak zou het verhaal van de vorming van heterojunctie tijdens fotoladen herhalen. Eerder werd aangetoond dat een bismutrijke $BiVO_4$ hogere bandposities heeft in vergelijking met $BiVO_4$ met een equimolaire verhouding van Bi:V. Dit zou suggereren dat de resulterende heterojunctie tussen bulk $BiVO_4$ en het bismutrijke $BiVO_4$ een verbeterde bandbuiging zal hebben, wat de waarneming van de röntgenonderzoeken van Raman Scattering bevestigt. De resultaten van de infraroodspectroscopie geven voldoende bewijs dat de foto-oplading een tijdelijk prestatieverbeteringsfenomeen is dat het gevolg is van de degradatie van de foto-elektrode onder verlichte omstandigheden.

De operando-infraroodspectroscopie en andere karakteriseringsstudies suggereren dat de gelijktijdige blootstelling van het kation- en de anionspecies van de foto-elektrode

aan de oxidatieve en reductieve omgeving binnen de foto-elektrode de oorzaak is van dit afbraakfenomeen. Dit gelijktijdige bestaan van een oxidatieve en reductieve omgeving binnen een elektrode is uniek voor foto-elektroden en dat geldt ook voor dit afbraakmechanisme. De redox-cycli van de oppervlakte-kation-anionsoorten in de foto-elektroden zijn eerder besproken in de context van öppervlakte-recombinatie"van ladingsdragers. Hier werd dit concept alleen besproken vanuit het perspectief van de impact op de efficiëntie van het apparaat. Met het werk dat in dit proefschrift is gedaan, hebben we voldoende bewijs geleverd om te suggereren dat het fenomeen van oppervlakterecombinatie ook een degradatiemechanisme is voor foto-elektroden. De auteurs bespreken ook de implicaties hiervan in dit proefschrift. Er wordt gesuggereerd dat dit degradatiemechanisme moeilijk te voorkomen zal zijn vanuit een materieel perspectief. De enige oplossing zou kunnen zijn om de impact ervan te "minimaliseren"door de juiste configuraties van het foto-elektrodesysteem te kiezen.

Met betrekking tot het algemene thema van het verlagen van de kapitaal- en bedrijfskosten van elektrochemische systemen, onderzoekt het proefschrift ook het gebruik van alternatieve manieren om de elektronische eigenschappen van elektrokatalysatoren aan te passen. De mogelijkheid hebben om de elektronische eigenschap van een katalysatoroppervlak selectief af te stemmen, heeft vele voordelen, waaronder een mogelijke verlaging van de kapitaal- en bedrijfskosten. Binnen deze context bieden de auteurs nieuwe inzichten in het effect van polymeerbelading op elektrokatalysatoren. Met een gecombineerde experimentele en computationele benadering wordt aangetoond dat wanneer gewone wateroxidatiekatalysatoren zoals nikkel worden gecoat met polymeren zoals polytetrafluorethyleen, een $Ni\text{-}CF_x$ binding wordt geproduceerd op het elektrokatalysator / polymeer-interface. De elektronenzuigende eigenschap van deze CF_x groep zal dan de elektronendichtheid van de naburige nikkelsoorten veranderen, waardoor de activiteit en selectiviteit van deze katalytische plaatsen veranderen. De auteurs suggereren dat dit concept van polymeerbelading van elektrokatalysatoren een nieuwe manier zou kunnen zijn om de elektronische eigenschappen van elektrokatalysatoren af te stemmen. Dit concept wordt ook steeds relevanter met het toegenomen gebruik van ionomeren en met katalysator beklede membraanelektroden, waarbij de katalysator in direct contact staat met polymeren zoals in het hierboven bestudeerde systeem.

6

Acknowledgements

Looking back, I am indebted to a lot of people that showed me the way and helped with through my journey to where I am today. In a way, you have shaped the person I am today and I will forever be thankful for that. I hope that we will cross paths again and that I can return the favours to all of you one day. Each of you have contributed to this thesis in one way or the other and I am going to use this section to try and thank you personally.

First, Prof. Andreas Schimdt-Ott for influencing me through his lectures and introducing me to the MECS group. The enthusiasm he shares when he talks about nanoparticles was truly inspiring. He introduced me to Prof. Wilson Smith and Marco Valenti, with whom I got the opportunity to work on my master thesis within the MECS group. If you ask me to pick one moment which changed the direction of my life, this might perhaps be it. It was here, that I found something that I enjoyed doing and defined the rest of my young career. Marco, your child like curiosity for fundamental science and the excitement and energy you bring always passed on positive energy to me. I'm sure these attributes will take you high and far in your career. I thank you for all the training and knowledge you've imparted to me and wish you luck in everything you wish to try.

Wilson, I do not know where to start. A mere mention here will not do justice to everything you have done and the opportunities you have given me. First you welcomed me to your research group as a master student and offered me all support I needed to execute that to the best of my ability. Next, you acted as my internship coordinator, when I needed one. As I mentioned earlier, it was during my time in your research group that I figured out what I enjoy doing the most and what I want to do in the future. I was over the moon when you offered me that PhD position in your group. I immediately knew what my answer to that offer was and I do not regret one bit for taking that up. It was from you that I learned how to put our research into a broader context and how to start from the big picture. Right from the get go, you always made sure your students got the exposure and access to the network that will help them build the next stage of their career. I see myself as one of the beneficiaries of it. You also made sure that we all became independent researchers and gave us the freedom to steer our topic to how we saw fit. There are many more things to list and thank you for, but I will stop here. I wish you and your family good health and success with everything coming your way.

I would also like to thank Prof. Arjan Houtepen, who was of great help and support during my PhD. You very willingly became my promotor, half way through my thesis when Wilson had to move abroad. I had many great discussions with you and it was really interesting to see that there was a lot of overlap between the work your group and I were doing, even though the end applications were completely different. You always had probing questions for me, which made me think further on the topic I was working on and helped me to refine it further. I wish you success in everything you venture into,

Arjan! I hope our paths will cross again.

Next up, is my MECS family. And of course, I cannot address the MECS group without addressing Prof. Bernard Dam. Bernard, you have been the corner stone of the MECS group for many years and have been a natural leader. You always found time to check on every member of the MECS group and made sure we grew as a scientist and as a person. You also always asked the right questions that picked our brains and helped us get deeper into the scientific problems we were working on. I feel lucky to have the opportunity to continue working with you with my current job. I wish you all the success in the coming years! I would also like to thank Prof. Fokko Mulder, Prof. Hans Geerlings and Dr. Wim Haije, for the many great discussions we have had during my time with the MECS group. The MECS group is in safe hands with you, Fokko, and I wish you great success with the Battolyzer venture. And of course, the ever present duo of Joost and Herman! I cannot thank you guys enough for all the help and support you have given us over the last few years. You both are the invisible glue that binds everything together within the MECS group and have always been a great company! I wish you both success for the years ahead! I will try to pop-in with some cakes every now and then ;) Same goes with Helen, Noortje, Rajashree, Roos and other management assistants who have been of great help and made our life a lot easier as PhD students. I would like to thank all of them here.

6

I would also like to thank Digda, Bartek, Ming and Steffen who were the experienced heads within MECS, when I joined them. I learned a lot from you guys and I thank you for all the help you have given me and the knowledge you shared. I wish you all the very best with your respective careers. And of course - Divya, Fahimeh and Nienke – you guys were the other experienced heads around us. It was really great to have you around and I learned a lot from you guys too. Divya, thank you for all the fresh perspectives you brought into the group with your computational work. It was always a pleasure to discuss different topics with you and you perspectives helped us understand those topics better. You have all the right tools to go high and far in life and I wish you and Mandar all the success in life! Fahimeh, thank you for all the good times. You are one of the very kind hearted person I know and you make the best cheesecakes! I wish you all the very best in life. And Nienke, it was a pleasure knowing you and working with you. And thanks for giving me the opportunity to come with you to ESRF. It was a very unique experience and we met some very nice people too! And thank you giving me some quick lessons in skiing and bouldering! It is also very nice to get the opportunity to work with you again and have you in the east of Netherlands as well. I wish you and Peter the very best in life! Next up, the rest of the bunnies gang – Kailun, Marijn and Sanjana (did I get the order right Marijn?) – it was great to start my PhD together with you guys and share the struggles and successes. It was great to see how you all developed into great scientists and professionals over time. Kailun, my office bestie, I cannot put in words how happy and proud I am to see you where you are today, after seeing all the effort and hard work you put to make yourself grow as a scientist and as a person. Your desire to get better at everything you do will take you to great places. I am super glad to have shared time and space with you for the past 4 years and talk about science, work and life and learn

from you while doing so. I am also glad that you also started working in the same city as I am! I wish you and Kayiu all the best with everything in life! Marijn, thanks for all the fun trips, dinners, games and scientific discussions we have had. It's been a pleasure to share those moments with you. I wish you and Anna all the very best with everything you guys venture into! Sanjana, the same goes with you. Thanks a lot for all the fun times and Diwali sweets! I wish you and Tushar success with everything in life.

Tom, Dowon and Recep – you guys were the very talented post docs in the group, who we could look up to and ask all the silly questions. Tom (a.k.a "captain"), it was refreshing to see you join the group and bring in new ideas and change the perspectives of everyone around you. This kind of set the bar for most of us, as to where we need to be at the end of our PhD. It was also incredibly pleasing to see you kick-on from there and build your own group in a span of few years. It was always nice to discuss science and life with you. I am really looking forward to work closely with you and your group in the coming years. I wish you, Sarah and Oliver all the success in life! Dowon, being the only other person in the group who did photoelectrochemistry, it was really helpful to have you around and learn from you. I wish you all the very best in Scotland. Recep, you are one of the most beautiful and knowledgeable minds I know! Anyone can easily have an in-depth conversation about anything with you and that is one of your strengths. Thank you for all the knowledge you have shared and the works we did together. I wish you all the very best in the states! Kai and Nate – the other former members of SmithLabNL – it was great to have you guys around. I learned a lot from both of you too. Thank you for everything and good luck!

Giorgio, Davide, Audrey, Erdem – it was really great to have you guys in the MECS group. Cheers to all the beach volleyball and squash and other good times we have shared. Gio, you are always so kind and it was great to also share the office with you. I always admired your drive to try out new things (and excel in each one of them!) and I feel like there is nothing left in which you haven't tried your hand in. I hope you keep up that spirit! I wish you and Diana all the best wishes! Davide, another kind and down to earth Italian (I see a trend here!)! It's been great to know you in person and thanks for all the good times we have spent! I wish you the very best with the last phase of your PhD and the next steps in your career. Audrey, you have always been very sweet to everyone around you and it was great to have you within the MECS group. Goodluck with all your adventures back in Toulouse. Erdem, thanks for all the Turkish sweets and your amazing kebab's. It was great to have you in the MECS group! I wish you the very best at VSP! My other MECS friends – Robin, Martin, Bernhard, Mark (Sassy pants), Diana, Hugo, Sid, Maryam, Aaron, Mark (W), Dylan and Peter – thanks for all the great memories. I wish you all the very best in life!

I have been incredibly fortunate to supervise some very bright master and bachelor students - Joost, Bas, Kayeu, Marieke and Lars – on their end thesis. I have learned a lot from each of you and I really hope I was able to pass on some valuable knowledge to all of you. Thank you for all the hard work and the good times we have spend together. You have played a major part in putting together this thesis and I would like to thank each

6

one of you for that. I am sure that each of you will scale great heights and I will be cheering for you from the side lines all the way through! Please don't hesitate to reach out if there is anything I can do for you at any time.

I would also like to thank all my friends and collaborators in Prof. Evgeny, Vivek, Jittima, Jan, Prof. Marc Koper, Ale, Chiarra, Christoph and Ursa with whom I have been fortunate enough to learn from and to do some great science! I am incredibly thankful for the opportunities I have had to work with each of you. I wish you all the very best. I would also like to thank some other incredible support staff of TU Delft – Ruben, Bart, Marcel and others – who have all helped us in various stages of our PhD and made our life a lot easier. I would also like to thank Tomaz and Angie for all the fun filled beach volleyball and kayaking sessions we have had. I wish you both success with everything you venture into.

Next, I would like to thank my support system of friends and family. Aswin and Jishnu, whom I have known since my bachelors! We took the journey to the Netherlands together and having you guys here right from the start made my life here so much easier. We know we have each other to fall back on, if needed, and I would like to thank you both for that. Aswin, thank you for listening to all my PhD frustrations and being my support structure in Delft. I hope I have been there for you too, when needed. I can see you reaching really great heights, perhaps even getting a Nobel one day ;) Jishnu, cheers to all the great trips and good times we have had! I hope there is more to come. I will be rooting for both of you all the way. Varsha, Deepak, Amit, Manju, Sneha and others, who I met and became friends with during my masters at TU Delft. You have all been incredibly kind to me and I cannot thank you all enough for that. I wish you all the very best in life. I am also incredibly happy to see two of my best friends and travel buddies, Jishnu and Varsha, get married during my PhD time and I wish them both all the happiness and luck in this world. I hope you get to see many more places and reach to all corners of the globe. I would also like to thank my ChemBuddies and other friends back home for always being there for me. Thanks also to my former housemates in Delft – Andrea, Diogo, Nadine and others – for always creating a good atmosphere back home and being awesome housemates! Cheers to all the good times!

Last but not the least, my family back home. Jai and Amma, I cannot thank you both enough for all the sacrifices you have made for me to get here. I don't think I can every repay you for all of that, but I will try. Thank you for always being there for me and cheering me through. Acha, this thesis is dedicated to you. I really wish you were there with us at this moment. I hope I am making you proud. I would also like to thank all my extended family for all the encouragement and support they have provided me and my family, all the way through.

Anirudh Venugopal
10-08-2022

Curriculum Vitæ

Anirudh VENUGOPAL

Anirudh was born in Mangalore, India, on 16th June 1992. He received his Bachelor's degree in Chemical Engineering (with distinction) from National Institute of Technology Calicut, India, in 2014. After a short stint as a trainee engineer at Bharat Petroleum Corporation Limited, Kochi Refinery, he moved to the Netherlands to pursue his masters. He received his Master's degree in Chemical Engineering (with honours and cum laude) from Delft University of Technology in 2017. Soon after, he started his PhD work under the supervision of Prof. Wilson A. Smith in the Materials for Energy Conversion and Storage group of the Applied Sciences faculty of TU Delft. His research focused on understanding the electrode/electrolyte interfaces in (photo-)electrochemical systems. He is currently working as the Chief Technology Officer at HyET E-Trol, an energy technology start-up developing next generation water electrolyzers.

List of Publications

11. **Venugopal, A.** & Smith, W. A. *Advancing the understanding of the semiconductor/electrolyte interface in metal oxide photoelectrodes*, (submitted).

10. **Venugopal, A.**, Egberts, L. H., Meeprasert, J., Pidko, E. A., Dam, B., Burdyny, T., ... & Smith, W. A. *Polymer Modification of Surface Electronic Properties of Electrocatalysts.*, ACS Energy Letters **7**, 5 (2022).

9. **Venugopal, A.**, Kas, R., Hau, K., & Smith, W. A. *Operando Infrared Spectroscopy Reveals the Dynamic Nature of Semiconductor–Electrolyte Interface in Multinary Metal Oxide Photoelectrodes.*, Journal of the American Chemical Society **143**, 44 (2021).

8. Bae, D., Kanellos, G., Faasse, G. M., Dražević, E., **Venugopal, A.**, & Smith, W. A. *Design principles for efficient photoelectrodes in solar rechargeable redox flow cell applications.*, Communications Materials **1**, 1 (2020).

7. Vos, J. G., **Venugopal, A.**, Smith, W. A., & Koper, M. T. *Competition and Interhalogen Formation During Parallel Electrocatalytic Oxidation of Bromide and Chloride on Pt.*, Journal of The Electrochemical Society **167** (2020).

6. Vos, J. G., **Venugopal, A.**, Smith, W. A., & Koper, M. T. *Competition and selectivity during parallel evolution of bromine, chlorine and oxygen on IrOx electrodes.*, Journal of catalysis **389** (2020).

5. Firet, N. J.*, **Venugopal, A.***, Blommaert, M. A., Cavallari, C., Sahle, C. J., Longo, A., & Smith, W. A. *Chemisorption of anionic species from the electrolyte alters the surface electronic structure and composition of photocharged BiVO4.*, Chemistry of Materials **31**, 8 (2019).

4. Abe, R., Aitchison, C. M., Andrei, V., Beller, M., Cheung, D., Creissen, C. E., **Venugopal, A.** ... & Zwijnenburg, M. A. *Demonstrator devices for artificial photosynthesis: general discussion.*, Faraday Discussions **215** (2019).

3. Firet, N. J., Blommaert, M. A., Burdyny, T., **Venugopal, A.**, Bohra, D., Longo, A., & Smith, W. A. *Operando EXAFS study reveals presence of oxygen in oxide-derived silver catalysts for electrochemical CO 2 reduction.*, Journal of Materials Chemistry A **7**, 6 (2019).

2. **Venugopal, A.**, & Smith, W. A. *Light induced formation of a surface heterojunction in photocharged CuWO$_4$ photoanodes*, Faraday Discussions **215** (2019).

1. Valenti, M., **Venugopal, A.**, Tordera, D., Jonsson, M. P, Biskos, G., Schmidt-Ott, A., & Smith, W. A. *Hot carrier generation and extraction of plasmonic alloy nanoparticles.*, ACS photonics **4**, 5 (2017).